UNIVERSITY OF CALIFORNIA
RIVERSIDE

Pore-Space Partition of Crystalline Porous Materials via Monomer Trimerization for Gas Captures

A Dissertation submitted in partial satisfaction
of the requirements for the degree of

Doctor of Philosophy

in

Chemistry

by

Yanxiang Wang

December 2021

Dissertation Committee:
Dr. Pingyun Feng, Chairperson
Dr. Boniface P.T. Fokwa
Dr. Yadong Yin

The Dissertation of Yanxiang Wang is approved:

Committee Chairperson

University of California, Riverside

Acknowledgement

By taking this chance, I want to express my gratitude to everyone supported me in the last five years. I am grateful for their aspiring assistance and priceless constructive advice no matter on my research or in my life. I am sincerely thankful to all of them for their patience and support in obstacles I have encountered through my study.

Foremost, I would like to express my sincere appreciation to my advisor Prof. Pingyun Feng for the instruction on my Ph.D. study. I feel very lucky to join her group. Her patience, modesty, foresight and wisdom motivate to constantly move forward. Her supports and advices helped me to conduct research and finish writing of this thesis. I am truly grateful to her unswerving support.

I also want to thank Prof. Xianhui Bu from CSULB for the fruitful discussions. He is a knowledgeable and smart structural chemist. It is enlightening and encouraging to discuss with him. His helpful suggestions and persistent collaborations enabled me to finish my study.

I am also grateful to all of the past and current group members from Prof. Pingyun Feng's research team. Firstly, I want to thank three postdoctoral researchers: Dr. Xiang Zhao, Dr. Wei Jiao and Dr. Huajun Yang. The collaboration and discussions with them helped me learn and grow a lot. I also want to thank the visiting scholars: Dr. Mingming Zheng, Dr. Guoping Yang, Dr. Xiaowu Lei, Dr. Yanli Gai, Dr. Gang Xiong, Dr. Yong Wang, Dr. Xiaoxia Jia, Dr. Kun Lan, Dr. Dandan Hu, and Dr. Songsong Li. Moreover, I

want to thank brothers and sisters in the lab: Dr. Xitong Chen, Dr. Chengyu Mao, Dr. Yuan Wang, Anh Hong, Yuchen Xiao, Yichong Chen and Pooja Ajayan. It's great experience to work with them.

I am also thankful to my committee members Prof. Boniface P.T. Fokwa and Prof. Yadong Yin for their valuable comments on my dissertation. Especially, I want to express my sincere appreciation to Prof. Ming Lee Tang, who is a committee member in my oral qualifying exam. Wish her a great success in the University of Utah.

I also would like to thank the staff in Department of Chemistry for their kindly help.

At last, I would like express my gratefulness to my step-father, Chengli Yin, my mother, Li Zhang, my father, Li An Wang, and my fiancé, Tingting Huang for everything they did for me. I could not possibly finish my study without their love and support. Their spiritual and emotional supports are the most valuable motivation for me to overcome obstacles thorough my Ph.D. research and study.

Dedication

To my respectful parents and my beloved wife

ABSTRACT OF THE DISSERTATION

Pore-Space Partition of Crystalline Porous Materials via Monomer Trimerization for Gas Captures

by

Yanxiang Wang

Doctor of Philosophy, Graduate Program in Chemistry
University of California, Riverside, December 2021
Dr. Pingyun Feng, Chairperson

The introduction of C_3-symmetric pore-partitioning agents, in the form of either molecular ligand such as 2,4,6-tri(4-pyridinyl)-1,3,5-triazine (tpt) or metal-complex clusters, into hexagonal channels of MIL-88/MOF-235 type (the **acs** net) to create **pacs**-type (partitioned **acs**) crystalline porous materials is an effective strategy to develop high-performance gas adsorbents.

In the first part, inspired by the synthetic chemistry of COF-1, we developed integrated COF-MOF chemistry through co-assembly of $[B_3O_3(py)_3]$ COF-type trimers and $[(M_3(OH)(COO)_6]$ MOF-type trimers as a new method for pore-space partition. With this strategy, the coordination-driven assembly of the **acs** framework occurs concurrently with the COF-1-type condensation of pyridine-4-boronic acid into a C_3-symmetric trimeric boroxine molecule leading to a new family of **pacs** materials. The new boroxine-based **pacs** materials exhibit dramatically enhanced NH_3 sorption properties.

In the second part, we further explored and utilized the method in the first part to let the self-assembly of the **acs** framework react simultaneously with the trimerization of three different monomers. Three monomers including 4-cyanopyridine, 4-vinylpyridine, and pyridine-4-boronic acid trimerized into 2,4,6-tri(pyridin-4-yl)-1,3,5-triazine (TPT), 1,3,5-tri(pyridin-4-yl)-cyclohexane (TPC), and 2,4,6-tri(4-pyridinyl)-1,3,5-boroxine (TPB) during the **pacs** materials formation. New materials exhibit excellent C_2H_2/CO_2 gas separation performance.

In the third part, we lengthened the monomer from pyridine-4-boronic acid to 4-(pyridin-4-yl) phenyl boronic acid and prepared two new **pacs** compounds with similar surface areas. C_3H_8 and C_3H_6 isothermal adsorption studies on these two compounds revealed the host-guest interaction sites in structures.

In summary, the pore-space partition of crystalline porous materials by monomer trimerization in this dissertation is a novel and efficient method for gas captures and host-guest interaction studies.

Table of Contents

List of Figures

List of Tables

Chapter 1 Introduction

1.1 Seven Critical Separation

Separating large quantities of chemical mixtures into individual pure phase is a daily routine but also a challenging issue for industrial chemists. [1] The separation processes, taking distillation for instance, hold ~15% energy cost around the world. [2] There are seven critical separations would be a game changer to industrial production including a solid phase separation: rare-earth metals from ores; four liquid phase separations: hydrocarbons from crude oil, benzene derivatives from each other, trace contaminants from water, and uranium from seawater; and two gas phase separations: greenhouse gases from dilute emissions, and alkenes from alkanes. [3]

There are 15 lanthanide metals, also known as rare-earth metals, widely used in energy generation and petrochemical refining. Despite their names, most of the elements are more fruitful in earth than noble metals such as gold and silver. However, rare earth metals are only trace amounts in ores and mixed with each other due to the similar chemical properties. Rare earth metal separation requires a combination of mechanical methods and chemical processing.[4] Unfortunately, these approaches are energy and chemical consuming.[5] The recycling of these metals from waste products is increasing. Various metallurgical and gas-phase extractions have been developed, but recycled rare earths are not yet involved in most purification process.[6]

Hydrocarbons are vital petrochemical raw materials for the production of polymers and plastics. Approximately 90 million barrels of crude oil is processed in the world's refineries every day. The atmosphere distillation cost around 230 gigawatts (GW), accounts for the amount of energy spends of UK in 2014, around the world.[7] Around 200,000 barrels of crude oil are heated and separated to various of components according to their boiling points in a refinery every day. Light components gather at the low temperature top and gradually heavier liquids leave at high temperature bottom. It is challenging to find an plan-B to distillation due to the complex components in crude oil, in which it contains high viscosities and large amount of contaminants such as sulfur materials, nickel, and mercury metals. Separating light hydrocarbons based on the difference in their physical parameters, such as molecular size and chemical affinity, is a viable method in tandem. Membrane separations or non-heating methods can be more energy friendly than the thermal driven classic distillation.

Benzene is a key solvent on the production chains of various chemical materials such as polymers, plastics, fibers, solvents and fossil fuel derivatives. Benzene and its derivatives including toluene, ethylbenzene, and xylene isomers are separated through column distillation, which costs around 50 GW of energy per year around the world.[7] Para-xylene (*p*-xylene) is the raw material for the production of PET (polyethylene terephthalate). However, similarity in size and boiling points in the isomers of xylenes, such as *m*- xylene, *o*- xylene, and *p*- xylene, makes it a challenge to separate them via method like distillation. The improvement in membranes and sorbents could lower the energy cost in these separations.

Distillation or membrane filtration are energy and money consuming methods for desalination. Reverse-osmosis filtration is a process applying pressure across a membrane to salty water to purified water. Though this method has been commercialized in the Middle East. But the expensive pretreatment of other pollutants in water is necessary. Advances in membranes enables a more efficient and money-saving approach for polluted water purification and desalination.

Nuclear power can be a main energy generation approach in the future due to the low carbon production and high energy efficiency.[7] Scientists have been working on uranium separation from water for years due to the existence of more than 4 billion tons of uranium in seawater at ppb levels. The amidoxime functionalized porous polymers are feasible candidates for uranium captures. However, the selectivity between uranium and other metals including nickel, vanadium, and cobalt, are low. Chemists need to conduct processes to remove other metals to purify and concentrate Uranium after the as-mentioned capture. Hundreds of tons of uranium are required for a nuclear power station; however, the current capture level is still far lower than kilogram-scale. The capture-scale needs to be increased and the cost of these materials needs to be lowered.

PE (polyethene) and PP (polypropene) are common plastics produced from alkenes such as ethylene and propylene.[8] The production of the two olefins are more than 200 million tons per year in the world. High-pressure Cryogenic distillation at low temperatures around -160 ° C is the most popular method in the industry separation of ethylene from ethane. Purification of olefins from paraffins is an energy consuming process. Porous carbon membranes are being applied to separate olefins from paraffins at room temperature

and mild pressures less than 10 atm. [9] But this method cannot meet the 99.9% purity of olefins for chemicals manufacturing. A combination of two methods might help – membranes can be utilized for first-round of separation and cryogenic distillation for further purify the product. This approach would reduce the energy cost before membranes become powerful enough to replace cryogenic method entirely.[10]

Emissions of CO_2 and other hydrocarbons such as CH_4 from human activities are the main cause of the global warming. Captures of these two gases from dilute sources such as vehicle exhausts, industry exhausts, and power plants are expensive and challenging. Monoethanolamine solution can react with CO_2, while the process is not economically feasible because of the heating process is required to regenerate the chemical to remove CO_2.[11] The conversions of CO_2 into crude-oil production and chemical raw products are feasible methods to consume the purified greenhouse gas.

1.2 Introduction to Metal-organic Frameworks

Introducing bulk porous materials into polymer membranes has been approved as an effective method to enhance the selectivity and separation efficiency in gas captures and separations.[12] Indeed, developing porous materials possessing abilities like high thermal and chemical stability, large accessible surface areas, strong interactions with gas molecules, high uptake capacity, and low energy cost to regenerate is an attractive and challenging research direction for gas captures and separations.[13]

Metal-organic frameworks (MOFs), also known as porous coordination polymers (PCPs), is a crystalline porous material.[14] This material is constructed by inorganic metal ions or metal clusters and organic ligands containing carboxylate, hydroxyl, pyridyl, or azolate groups via coordination bonds. Thanks to the highly accessible porosity, ultrahigh surface areas, various designable and tunable structures, and multiple functional sites, MOFs have been utilized in application of gas captures,[15] gas separations,[16] liquid phase catalysis,[17] gas phase catalysis,[18] water purification,[19] enzyme immobilization,[20] drug delivery,[21] etc.

1.3 Metal-organic Frameworks for Gas Captures and Separations

1.3.1 Open Metal Sites

Open metal sites (OMSs), also named unsaturated metal sites, are exposed after removing terminal coordinated chemicals like solvent molecules, H_2O, -OH, Cl^-, and F^-via solvent exchange, heating, and vacuumize. OMSs are strong interaction sites for guest molecules. Utilizing OMSs is an efficient method for gas captures [22] and separations.[23]

In 2005, Yaghi et al. reported a compound Zn_2(dobdc) (where dobdc is 2,5-dihydroxyterephthalate).[24] In dobdc, both hydroxyl and carboxylate groups functionalize as ligands coordinated to metal ions. In 2008, Matzger et al. reported an analogous structure, Mg-CPO-74 [Mg_2(dobdc)], and they utilized this compound for CO_2 capture after removing terminal solvents coordinated to Mg^{2+} via evacuation and heating.[23] The sorbent material possesses a honeycomb structure and 1D channels. The BET surface area

of Mg-CPO-74 is 1495 m^2/g, which is higher than its analogs composed by other metal ions. Besides, Mg-CPO-74 was found to provide 23.6 et % at 0.1 atm and 35.2 et % at 1 atm for CO_2 sorption isotherms measured at 296 K. Heat of adsorption illustrated a 47 kJ/mol for CO_2 in Mg-CPO-74. This CO_2 uptake value surpassed all other physisorptive materials at that time. In 2012, Long et al. reported *in situ* ^{13}C NMR measurements of CO_2 adsorbed in Mg-CPO-27 from 12 K to 400K to reveal a detailed picture of the dynamics of CO_2 rotational motion in Mg-CPO-27. Combining with spin-lattice relaxation, they observed the interaction was between open Mg sites and O sites on CO_2 molecules.[25]

In 2016, Dinca et al. reported a series of MOFs, $M_2Cl_2(BTDD)(H_2O)_2$ {where M = Mn^{2+}, Co^{2+}, Ni^{2+}, and BTDD = bis(1H-1,2,3-triazolo[4,5-b],[4′,5′-i])dibenzo[1,4]dioxin} in application of NH_3 capture.[26] Isostructural Mn, Co, and Ni analogs adsorbed 15.47, 12.00, and 12.02 mmol of NH_3/g. The isotherms of ammonia uptakes were among the highest at that time. This work described the first examples of MOFs with excellent uptake capacities and also were stable after repeated cycling of ammonia. The stability of azolate frameworks with OMSs facilitates the strong host-guest interactions between ammonia and MOFs in that work.

In 2017, Long et al. utilized M_2(*m*-dobdc) (M = Mn, Fe, Co, Ni; *m*-$dobdc^{4-}$ = 4,6-dioxido-1,3-benzenedicarboxylate) as adsorptions for olefin/paraffin separations (C_2H_4/C_2H_6, C_3H_6/C_3H_8).[27] Fe_2(*m*-dobdc) possesses the highest selectivity for C_2H_4/C_2H_6 (>25) and C_3H_6/C_3H_8 (>55). C_2H_4 binding site in Co_2(*m*-dobdc) was characterized via *in situ* single-crystal X-ray diffraction. The metal-carbon distances were 2.63 and 2.685 Å revealed from SCXRD results indicating a strong host-guest interaction. They performed

transient adsorption tests as well. Over 90 % of C_2H_4 was adsorbed less than 30 s after dosing. This further confirmed the interaction between as-prepared materials and C_2H_4 was strong. They further conducted transient breakthrough measurements on both gas pairs among those materials. The high uptake capacities, excellent selectivity, and fast adsorption kinetics enable M_2(*m*-dobdc) a competitive candidate for olefin/paraffin separations.

1.3.2 Molecular Sieving

Most of pore size manipulation is achieved via tuning on ligand length and metal nodes or incorporating bulky functional groups onto the organic ligands. These methods enable controlling on the size of pore opening to a certain degree.[28] Achieving ideal molecular sieving, where the large gas molecules are totally blocked and the uptakes of small molecules remain unchanged, is an energy efficient gas separation and purification method. This method can replace energy consuming cryogenic distillation to the energy friendly porous material based absorbent separations in the future.

In 2017, Chen et al. reported a porous material $Cu(apzy)_2(SiF_6)$ (SIFSIX-14-Cu-i/UTSA-200a, where apzy is 4,4'-azopyridine) achieve molecular sieving C_2H_2 from C_2H_4.[28] The pore size of UTSA-200 is only 3.4 Å, which can completely block out C_2H_4 molecule. Besides, the small pore size enhances the affinity of interaction between SiF_6^{2-} and C_2H_2 because the lowered distance enhances H···F interaction. At 0.01 bar, which is a sign for the C_2H_2 capture ability of adsorbents from a 1% C_2H_2/99% C_2H_4 mixture, USTA-

200a possessed 58 cm^3/cm^3 uptakes capacity of C_2H_2. This was the benchmark C_2H_2 uptake at 0.01 bar among all materials. The IAST selectivity is over 6000 at 1 bar and 298 K for C_2H_2/C_2H_4 mixture. USTA-200a was utilized to conduct transient breakthrough separation for C_2H_2/C_2H_4 (1/99) and the captured amount of C_2H_2 was as high as 1.18 mmol/g. The cycling test was performed over 12 times without any change. The C_2H_4 productivity was as high as 87.6 mmol/g per cycle. The excellent gas uptake capacity, ultrahigh selectivity, and high stability enable UTSA-200a become an efficient and ideal adsorbent for C_2H_2/ C_2H_4 separation.

The difference between C_3H_6 and C_3H_8 molecules is smaller than that of in C_2H_4 and C_2H_6 because the existence of methyl groups in both C3 gases. In 2020, Chen et al. reported a novel compound C-gallate·$2H_2O$ ($[Co(C_7O_5H_4)]\cdot 2H_2O$) in application of C_3H_8/C_3H_6 separation.[29] The small aperture size in this compound is only 16.8 $Å^2$, which is larger than the size of propylene (16.4 $Å^2$) and smaller than the size of propane (21.2 $Å^2$). The C_3H_6 isotherm in Co-gallate was 66.6 cm^3/cm^3 at 1 bar and 298 K, and the C_3H_8 isotherm in Co-gallate was only 5.2 cm^3/cm^3 at 1 bar and 298 K. Isosteric heat of adsorption for C_3H_6 was 41 kJ/mol. The IAST selectivity for C_3H_8/C_3H_6 was 330 at 1 bar and 298 K. Gas separation for C_3H_8/C_3H_6 was conducted. Co-gallate is a promising candidate for C_3H_8/C_3H_6 separation.

1.3.3 Cooperation Insertion of CO_2

In 2012, Long reported a new MOF, M_2(dobpdc) (M = Mg, dobpdc^{4-} = 4,4'-dioxido-3,3'-biphenyldicarboxylate).[30] This compound can be regarded as a longer version of MOF-74, Mg_2(dobdc). Mg_2(dobpdc) was functionalized with N, N'-dimethylethylenediamine (mmen) to get Mg_2(dobpdc)$(mmen)_{1.6}(H_2O)_{0.4}$ (mmen-Mg_2(dobpdc)). This compound possessed extremely high uptake of CO_2 at low pressures, which are 2.0 mmol/g a 0.39 mbar and room temperature. This condition is very similar to the removal of CO_2 from air. Gas adsorption/desorption cycling experiments illustrate that mmen- Mg_2(dobpdc) can be regenerated after repeated exposures to the simulated air. The purity of the CO_2 recovered from dry air was ~96%. In 2015, Long et al. utilized a series of characterization approaches to confirm the CO_2 insertion process was carbamate insertion into the metal–nitrogen bond.[31] The reactions occurred during the adsorption process. This method is a chemisorption process, which is different from the previous two physisorption in 1.3.1 and 1.3.2.

1.4 Pore-Space Partition Strategy

1.4.1 Introduction to Pore-Space Partition

In 2015, our group members Zhao et al. reported a novel strategy named pore-space partition, which is introducing a size- and symmetry-matching molecule 2,4,6-tri(4-pyridyl)-1,3,5-triazine (tpt) into MIL-88B framework (**acs** net) to divide 1D channel into

consecutive pockets.[32] The materials were named as **pacs** (partitioned-**acs**) prepared via this method.

A series of MIL-88 materials was first reported by Ferey et al. in 2004.[33] The formular of MIL-88B is $M_3O(BDC)_3(H_2O)X_2$ (where M = Fe^{3+}, Cr^{3+}, X = F^-, Cl^-). This category of materials possesses hexagonal 1D channels. However, these structures are highly flexible and able to shrink and expand under different conditions.[34] The guest accessibility to the channels are very limited as shown in Figure 1.1.

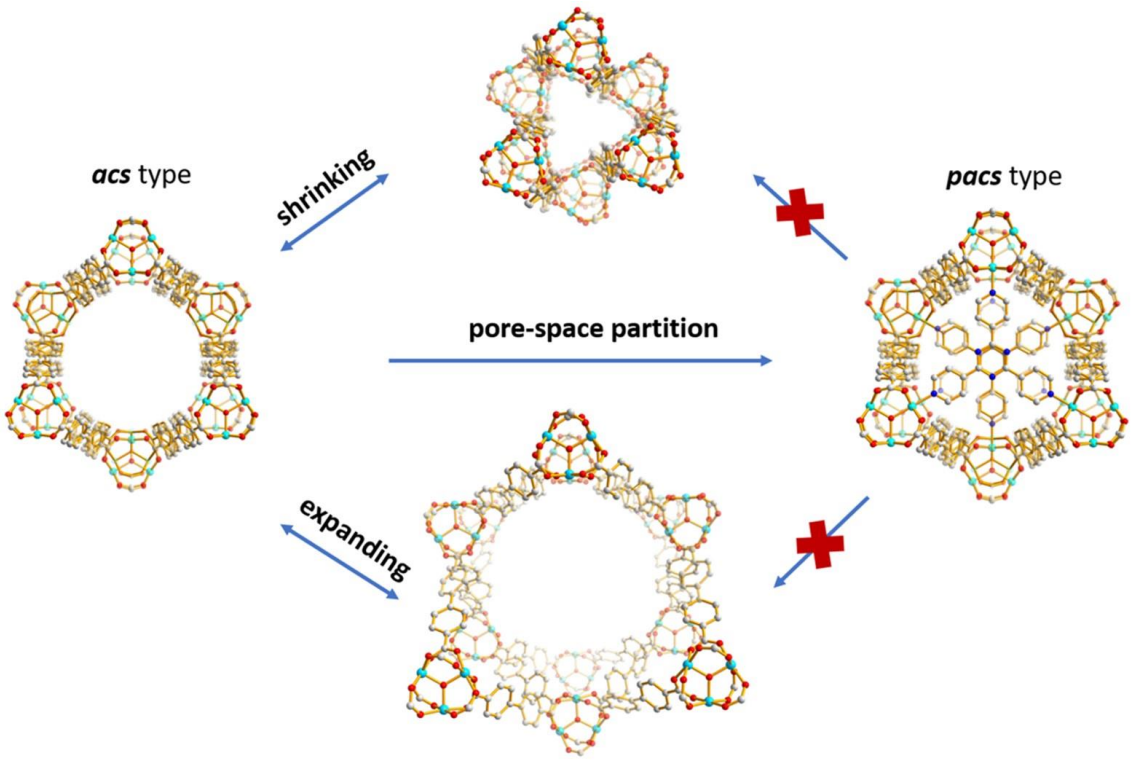

Figure 1.1 Illustration of the structure flexibility in MIL-88 and robustness in **pacs** materials

The introduction of tpt molecule into MIL-88B channels enable the replacement of terminal group such as H_2O, F^-, and Cl^- by pyridines on the C_3 partitioning ligand. This

strategy can fix the distance between three metal trimers on the same layer and make the pore-space partitioned structures become rigid. (Figure 1.1).

The isotherms gas adsorption results in **pacs** materials are amazing as well. Among all materials, $Ni_3(OH)(DHBDC)_3TPT$ (CPM-33b, $DHBDC^{2-}$ = (2,5-dihydroxylterephthalate) exhibits 173.9 cm^3/g CO_2 uptake at 273 K and 126.4 cm^3/g CO_2 uptake at 298 K. This result is comparable to Ni-MOF-74 (Ni_2(DOBDC)) under the same condition.

The pore-space partition strategy attracts a lot of attention not only because the novel design and synthesis method, but also due to the excellent gas adsorption ability.[35] A series of work in this system had been reported since 2015. The strategies to construct pacs materials are categorized into three and introduced below.

1.4.2 Molecular Ligands Insertion Strategy

This strategy is to introduce tpt-type molecules into **acs** net to construct **pacs** materials (Figure 1.2). In 2016, our group members Zhai et al. utilized heterometallic method to replace the Ni_3 metal trimers in previous work and prepare a large number of novel MOFs.[36] Among all the materials, $Mg_2V(OH)DHBDC_3TPT$ possesses CO_2 uptake as high as 232.3 cm^3/g at 1 atm and 273 K. This is one of the best CO_2 adsorbents among all materials reported to date. The Q_{st} in CO_2 for CPM-233 [$Mg_2V(OH)(DHBDC)_3TPT$] is 20.38 kJ/mol at zero coverage, which is much lower than 42 kJ/mol for Mg-MOF-74 [Mg_2(dobdc)] and 42.2 kJ/mol for Cu-TDPAT [$Cu_3(TDPAT)(H_2O)_3$].

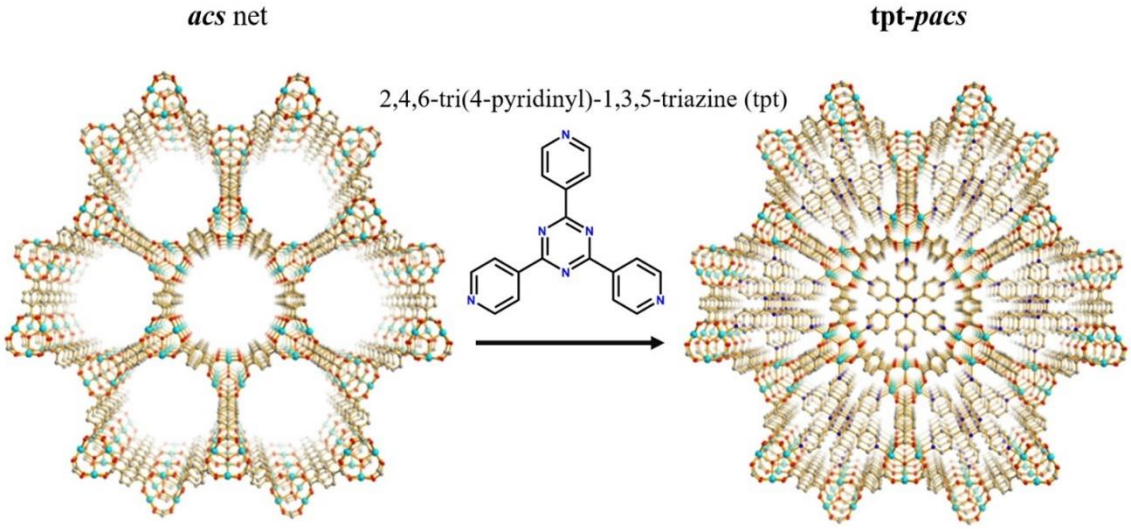

Figure 1.2 Illustration of tpt-type molecule insertion strategy.

In 2020, our group member Yang et al. utilized the same material construction strategy reported a series of MOFs for C_2H_6 uptake.[37] Among all materials, C_2H_6 uptake in $Mg_2V(OH)BDC_3TPT$ (CPM-233) is as high as 166.8 cm^3/g at around 1 bar and 298 K. This is the highest C_2H_6 uptake among all materials. Besides, the isosteric heat of adsorption (Q_{st}) in C_2H_2 belongs to CPM-733 [$Co_2V(OH)BDC_3TPT$] is only 21.9 kJ/mol at zero coverage, which is much lower than 66.8 kJ/mol for $Fe_2(O_2)$(dobdc) and 25 kJ/mol for Fe_2(dobdc). The same strategy was followed by other groups as well.[38]

1.4.3 Metal-cluster Insertion Strategy

In 2016, our group members Zhao et al. reported a new construction method for **pacs** materials.[39] We introduced a series of metal-clusters including $M_2(trz)_3$ and $Cu_3O(trz)_3$ (where M = Co^{2+}, Ni^{2+}, Mn^{2+}, Zn^{2+}, Mg^{2+}, trz^- = 1,2,4-triazolate) into MIL-88B

channel to construct **pacs** materials (Figure 1.3). The highest CO_2 uptake in this work can reach up to 146.7 cm^3/cm^3.

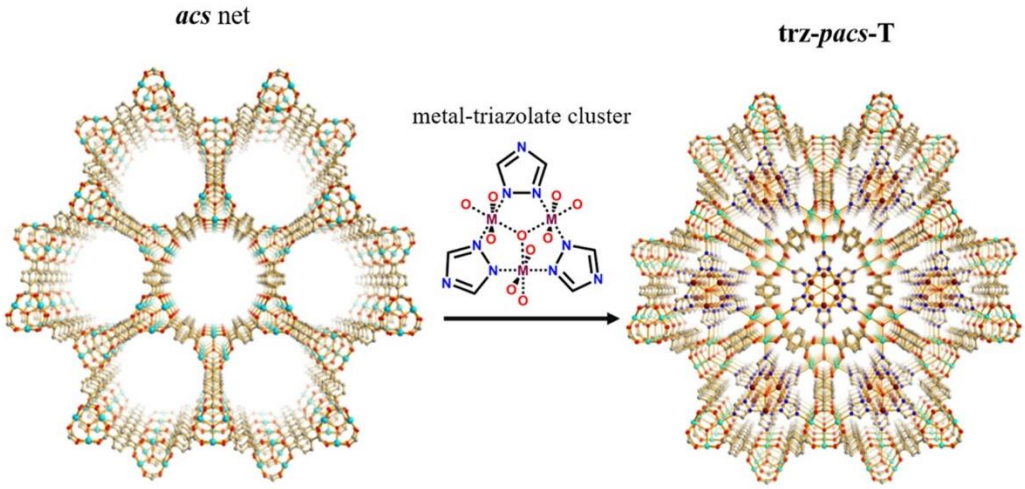

Figure 1.3 Illustration of metal-azolate cluster insertion strategy.

In 2013, our group members Zheng et al. introduced monomer metal-cluster $Zn(H_2O)INT_3$ and dimer metal-cluster $Co_2(OH)(H_2O)INT_3$ (where INT = isonicotinate) into hexagonal channel of **acs** network to construct a series of **pacs** materials (Figure 1.4).[40] This work didn't focus on gas adsorption and no CO_2 uptake results were reported.

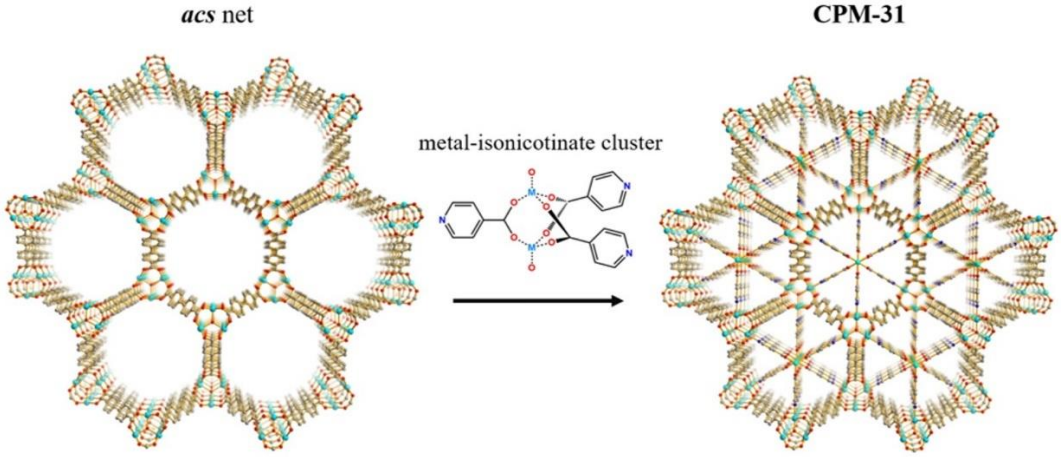

Figure 1.4 Illustration of metal-isonicotinate cluster insertion strategy.

1.4.4 Post-synthetic Modification and [2+2+2] Cyclotrimerization

In 2015, Chen et al. reported a post-synthetic strategy to construct **pacs** materials. They prepared MIL-88B first and introduced three monomers including 4-cyanopyridine, 4-vinylpyridine, and 4-ethynylpyridine into as the as-prepared material to replace terminal groups via Soxhlet extraction method.[41] After the terminal groups were fully replaced, the intermediate materials were heated at 140 °C for 12h enabling the [2+2+2] cyclotrimerization reaction happened between loaded monomers. As a result, three pore-partitioning ligands including ,4,6-tri(pyridin-4-yl)-1,3,5-triazine (TPT), 1,3,5-tri(pyridin-4-yl)-cyclohexane (TPC), and 2,4,6-tri(4-pyridinyl)-1,3,5-benzene (TPBz) were formed in the networks.

1.5 Contribution from This Work

In my study, I developed a pathbreaking strategy to combine coordination-driven MOF materials with covalent bond-driven trimerized monomers concurrently and synergistically to construct a large family of **pacs** materials via introducing toluene or TMB (1,3,5-trimethylbenzene) into DMF (N, N-Dimethylformamide) or DMA (N, N-Dimethylacetamide) as reaction co-solvent.

Monomers including pyridine-4-boronic acid, 4-(pyridine-4-yl) phenylboronic acid, 4-cyanopyridine, and 4-vinylpyridine were reported to construct pore-space partitioning ligands including 2,4,6-tri(4-pyridinyl)-1,3,5-boroxine (TPB), 2,4,6-tris(4-

(pyridin-4-yl) phenyl)-1,3,5-boroxine (TPPB), 2,4,6-tri(pyridin-4-yl)-1,3,5-triazine (TPT), and 1,3,5-tri(pyridin-4-yl)-cyclohexane (TPC) in my work.

Gas uptake studies including NH_3, CO_2, C_2H_2, C_3H_6, C_3H_8 were conducted on these materials. The results illustrated that the boroxine ring in TPB molecule can interact with NH_3 through Lewis acid-base interaction on B sites in Chapter 2 and with C_2H_2 via H···O interaction on O sites in Chapter 3. Besides, the host-guest interaction site study was also confirmed through experimental result and structure analysis in Chapter 4.

My dissertation not only develops a novel material preparation methodology and conducts host-guest interaction studies, but also enlightens the future integrated materials study.

1.6 Reference

[1] D. S. Sholl, R. P. Lively, *Nature* **2016**, *532*, 435-437.

[2] Oak Ridge National Laboratory. *Materials forSeparation Technologies: Energy and Emission Reduction Opportunities*, **2005.**

[3] Humphrey, J. & Keller, G. E. *Separation Process Technology*, **1997**.

[4] A. Jordens, Y. P. Cheng, K. E. Waters, *Miner. Eng.* **2013**, *41*, 97-114.

[5] S. Massari, M. Ruberti, *Resources Policy* **2013**, *38*, 36-43.

[6] N. Muthukaman, S. Deshmukh, S. Tondlekar, M. Tambe, D. Pisal, N. Sarode, S. Mhatre, S. Chakraborti, D. Shah, V. M. Bhosale, A. Kulkarni, M. Y. A. Mahat, S. B. Jadhav, G. S. Gudi, N. Khairatkar-Joshi, L. A. Gharat, *Bioorg. Med. Chem. Lett.* **2018**, *28*, 3766-3773.

[7] US Dept. Energy Advanced Manufacturing Office. *Bandwidth Study on Energy Use and PotentialEnergy Saving Opportunities in U.S. PetroleumRefining*, **2015**.

[8] W. J. Koros, R. P. Lively, **2012**, *R. P. AIChE J.58*, 2624-2633.

[9] B. Su, T. Wang, Z. Wang, X. Gao, C. Gao, *J. Membr. Sci.* **2012**, *423-424*, 324-331.

[10] H. Lee, S. Kang, J. Y. Lee, J. H. Jung, *Soft Matter* **2012**, *8*, 2950-2955.

[11] Interagency Working Group on Social Cost of Carbon (US Govt.). *Social Cost of Carbon for Regulatory Impact Analysis*, **2013**.

[12] a) R. Zhang, S. Ji, N. Wang, L. Wang, G. Zhang, J. R. Li, *Angew. Chem. Int. Ed. Engl.* **2014**, *53*, 9775-9779; b) M. S. Denny, Jr., S. M. Cohen, *Angew. Chem. Int. Ed. Engl.* **2015**, *54*, 9029-9032; c) J. E. Bachman, Z. P. Smith, T. Li, T. Xu, J. R. Long, *Nat. Mater.* **2016**, *15*, 845-849.

[13] X. Zhao, Y. Wang, D.-S. Li, X. Bu, P. Feng, *Adv. Mater.* **2018**, *30*, 1705189.

[14] H.-C. Zhou, J. R. Long, O. M. Yaghi, *Chem. Rev.* **2012**, *112*, 673-674.

[15] D. E. Jaramillo, D. A. Reed, H. Z. H. Jiang, J. Oktawiec, M. W. Mara, A. C. Forse, D. J. Lussier, R. A. Murphy, M. Cunningham, V. Colombo, D. K. Shuh, J. A. Reimer, J. R. Long, *Nat. Mater.* **2020**.

[16] X. Cui, K. Chen, H. Xing, Q. Yang, R. Krishna, Z. Bao, H. Wu, W. Zhou, X. Dong, Y. Han, B. Li, Q. Ren, M. J. Zaworotko, B. Chen, *Science* **2016**, *353*, 141.

[17] X. Yu, S. M. Cohen, *J. Am. Chem. Soc.* **2016**, *138*, 12320-12323.

[18] J.-S. Qin, S. Yuan, L. Zhang, B. Li, D.-Y. Du, N. Huang, W. Guan, H. F. Drake, J. Pang, Y.-Q. Lan, A. Alsalme, H.-C. Zhou, *J. Am. Chem. Soc.* **2019**, *141*, 2054-2060.

[19] N. Hanikel, X. Pei, S. Chheda, H. Lyu, W. Jeong, J. Sauer, L. Gagliardi, O. M. Yaghi, *Science* **2021**, *374*, 454-459.

[20] X. Zhao, C. Mao, K. T. Luong, Q. Lin, Q.-G. Zhai, P. Feng, X. Bu, *Angew. Chem. Int. Ed.* **2016**, *55*, 2768-2772.

[21] H. Zheng, Y. Zhang, L. Liu, W. Wan, P. Guo, A. M. Nyström, X. Zou, *J. Am. Chem. Soc.* **2016**, *138*, 962-968.

[22] D.-A. Yang, H.-Y. Cho, J. Kim, S.-T. Yang, W.-S. Ahn, *Energy & Environmental Science* **2012**, *5*, 6465-6473.

[23] S. R. Caskey, A. G. Wong-Foy, A. J. Matzger, *J. Am. Chem. Soc.* **2008**, *130*, 10870-10871.

[24] N. L. Rosi, J. Kim, M. Eddaoudi, B. Chen, M. O'Keeffe, O. M. Yaghi, *J. Am. Chem. Soc.* **2005**, *127*, 1504-1518.

[25] X. Kong, E. Scott, W. Ding, J. A. Mason, J. R. Long, J. A. Reimer, *J. Am. Chem. Soc.* **2012**, *134*, 14341-14344.

[26] A. J. Rieth, Y. Tulchinsky, M. Dincă, *J. Am. Chem. Soc.* **2016**, *138*, 9401-9404.

[27] J. E. Bachman, M. T. Kapelewski, D. A. Reed, M. I. Gonzalez, J. R. Long, *J. Am. Chem. Soc.* **2017**, *139*, 15363-15370.

[28] B. Li, X. Cui, D. O'Nolan, H.-M. Wen, M. Jiang, R. Krishna, H. Wu, R.-B. Lin, Y.-S. Chen, D. Yuan, H. Xing, W. Zhou, Q. Ren, G. Qian, M. J. Zaworotko, B. Chen, *Adv. Mater.* **2017**, *29*, 1704210.

[29] B. Liang, X. Zhang, Y. Xie, R.-B. Lin, R. Krishna, H. Cui, Z. Li, Y. Shi, H. Wu, W. Zhou, B. Chen, *J. Am. Chem. Soc.* **2020**, *142*, 17795-17801.

[30] T. M. McDonald, W. R. Lee, J. A. Mason, B. M. Wiers, C. S. Hong, J. R. Long, *J. Am. Chem. Soc.* **2012**, *134*, 7056-7065.

[31] T. M. McDonald, J. A. Mason, X. Kong, E. D. Bloch, D. Gygi, A. Dani, V. Crocellà, F. Giordanino, S. O. Odoh, W. S. Drisdell, B. Vlaisavljevich, A. L. Dzubak, R. Poloni, S. K. Schnell, N. Planas, K. Lee, T. Pascal, L. F. Wan, D. Prendergast, J. B. Neaton, B. Smit, J. B. Kortright, L. Gagliardi, S. Bordiga, J. A. Reimer, J. R. Long, *Nature* **2015**, *519*, 303-308.

[32] X. Zhao, X. Bu, Q. G. Zhai, H. Tran, P. Feng, *J. Am. Chem. Soc.* **2015**, *137*, 1396-1399.

[33] C. Serre, F. Millange, S. Surblé, G. Férey, *Angew. Chem. Int. Ed.* **2004**, *43*, 6285-6289.

[34] C. Mellot-Draznieks, C. Serre, S. Surblé, N. Audebrand, G. Férey, *J. Am. Chem. Soc.* **2005**, *127*, 16273-16278.

[35] Q.-G. Zhai, X. Bu, X. Zhao, D.-S. Li, P. Feng, *Acc. Chem. Res.* **2017**, *50*, 407-417.

[36] Q. G. Zhai, X. Bu, C. Mao, X. Zhao, L. Daemen, Y. Cheng, A. J. Ramirez-Cuesta, P. Feng, *Nat. Commun.* **2016**, *7*, 13645.

[37] H. Yang, Y. Wang, R. Krishna, X. Jia, Y. Wang, A. N. Hong, C. Dang, H. E. Castillo, X. Bu, P. Feng, *J. Am. Chem. Soc.* **2020**, *142*, 2222-2227.

[38] a) Y. Ye, Z. Ma, R.-B. Lin, R. Krishna, W. Zhou, Q. Lin, Z. Zhang, S. Xiang, B. Chen, *J. Am. Chem. Soc.* **2019**, *141*, 4130-4136; b) Q.-G. Zhai, Y.-Y. Xue, X.-Y. Bai, J. Zhang, Y. Wang, S.-N. Li, Y.-C. Jiang, M.-C. Hu, *Angew. Chem. Int. Ed.* **2021**, *60*,10122 –10128.

[39] X. Zhao, X. Bu, E. T. Nguyen, Q. G. Zhai, C. Mao, P. Feng, *J. Am. Chem. Soc.* **2016**, *138*, 15102-15105.

[40] S.-T. Zheng, X. Zhao, S. Lau, A. Fuhr, P. Feng, X. Bu, *J. Am. Chem. Soc.* **2013**, *135*, 10270-10273.

[41] Y. S. Wei, M. Zhang, P. Q. Liao, R. B. Lin, T. Y. Li, G. Shao, J. P. Zhang, X. M. Chen, *Nat. Commun.* **2015**, *6*, 8348.

Chapter 2 A COF-1-Inspired Synthetic Strategy for Pore-Space Partition of MOFs

2.1 Introduction

Metal-organic frameworks (MOFs) are crystalline porous materials possessing intriguing structural characteristics,[1] have attracted intensive attention in the last two decades for various applications like gas sorption,[2] separation,[3] catalysis and so on.[4] Pore space partition has been proven as a versatile design strategy for constructing crystalline porous materials (CPM) with much enhanced chemical stability and gas sorption properties.[5] A prominent platform involves the introduction of C_3-symmetric pore-partitioning agents into hexagonal channels of MIL-88/MOF-235 type structures,[6] also known as **acs** net, to form 9-connected **pacs** framework.[7] The flexibility of **acs** parent framework enables a large number of pore-partitioning agents to be used within the channel. To expand the **pacs** system, novel strategies for designing symmetry-matching C_3-partitioning agents are needed, and some of which have been demonstrated, including: (i) individual tpt-type ligand insertion method to prepare tpt-**pacs** (tpt = 2,4,6-tri(4-pyridinyl)-1,3,5-triazine) materials, (ii) co-assembly of the **acs** frameworks with in situ formed metal-ligand clusters based on isonicotinate and 1,2,4-triazolate with monomeric, dimeric, and trimeric metal cores,[7] and (iii) post-synthetic modification and

cyclotrimerization approach to introduce tpt, tpbz (2,4,6-tri(4-pyridinyl)-1,3,5-benzene), and tpc (2,4,6-tri(4-pyridinyl)- 1,3,5-cyclohexane).[8]

Covalent-organic frameworks (COFs) are a new class of crystalline porous materials built up by covalent bonds between light elements (B, C, N, O, Si).[9] Organic building units are linked covalently into extended 2D or 3D nets. Various chemical strategies have been reported to construct COFs including: (1) boron-oxygen based linkages such as B_3O_3 boroxine 6-ring or BO_2C_2 boronate ester 5-ring,[10] (2) C=N imine-based linkage,[11] (3) $(CN)_3$ triazine-based linkage,[12] and (4) other methods such as imidization reaction.[13] These chemical reaction strategies have led to rapid growth of COF materials. However, the integration of such COF chemistry with coordination-driven MOF chemistry, especially as it relates to pore space partition method, has not been explored.

In this work, we have integrated COF-1 chemistry (Figure 2.1a),[10] also known as self-condensation of boronic acids, with the MOF chemistry to develop a novel pore partition method, leading to the synthesis of a new family of pore-partitioned materials. Our method makes use of pyridine-4-boronic acid, which is introduced as monomer, or organic building block, into the MIL-88-type reaction system. During the reaction, a new pore-partitioning ligand, trimer of pyridine-4-boronic acid, is formed as tpb (2,4,6-tri(4-pyridinyl)-1,3,5-boroxine). (Figure 2.1b) The use of toluene as co-solvent into DMF and DMA promotes boronic acid condensation to build up our tpb-**pacs** materials, as a result of MOF-COF synergistic reaction. The simultaneous construction of two totally different reactions requires all components to work cooperatively. The metal ions coordinate with pyridine-4-boronic acid (or its trimer) at the N-side during metal trimer ($M_3(OH)(COO^-)_6$)

formation process (Figure 2.1c), and the condensation of three boronic acids occur at the B-side forming a C_3-symmetric pore-partitioning ligand. Crystal structures of In-Co-based materials were determined by single-crystal X-ray diffraction (Table 2.1).

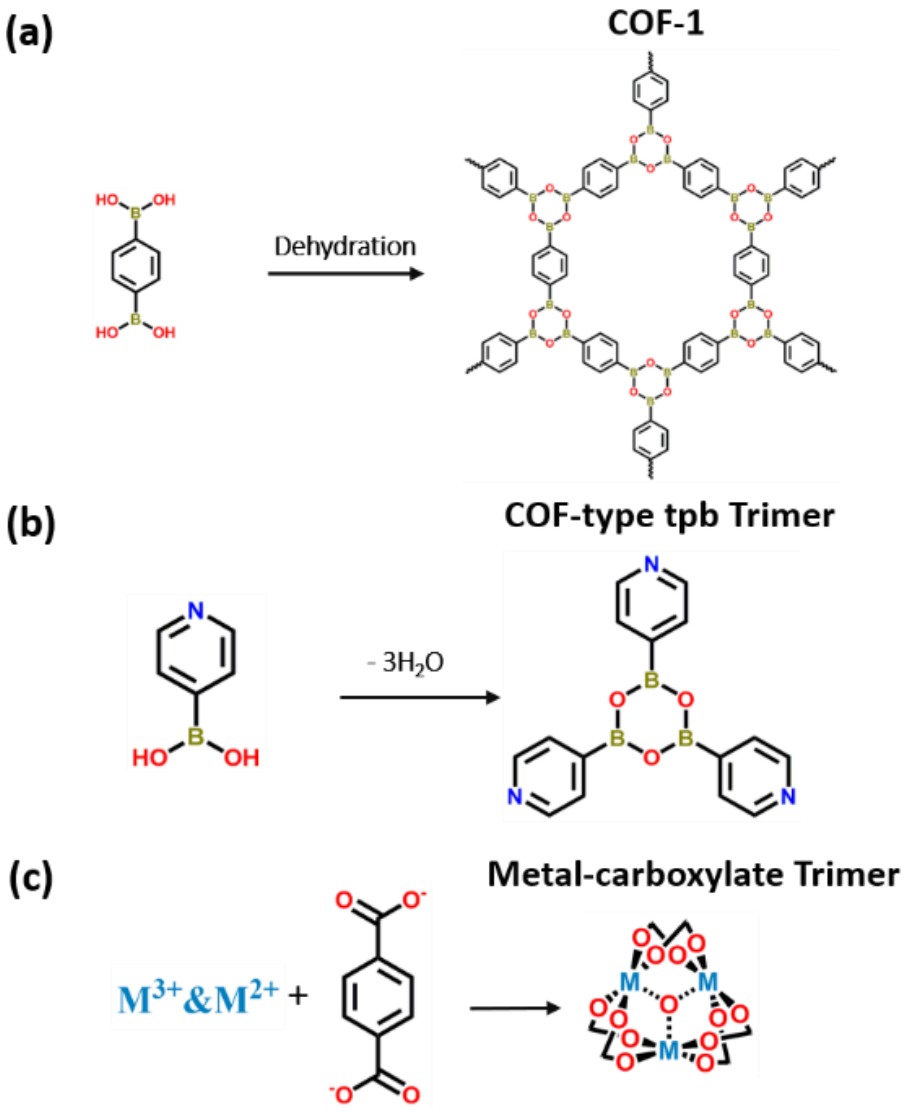

Figure 2.1(a) Condensation reaction of benzene-1,4-diboronic acid to prepare COF-1. (b) pyridine-4-boronic acids self-assemble into tpb through covalent bonds. (c) Metal-carboxylate trimer formation through coordination bonds.

It is noteworthy the trimer of pyridine-4-boronic acid (tpb) does not form under common chemistry environment. The realization of its formation highlights a significant difference between standard COF chemistry and COF-type chemistry reported here. In COF-1, two sides of boronic acids are identical, whereas in our chemistry, two sides are different. Under normal chemical condition, the B-site in the targeted trimer would bond to N-site from pyridyl group in a competitive reaction. Thanks to metal-pyridine coordination, the side reaction of B-N coordination is avoided (Figure 2.2).

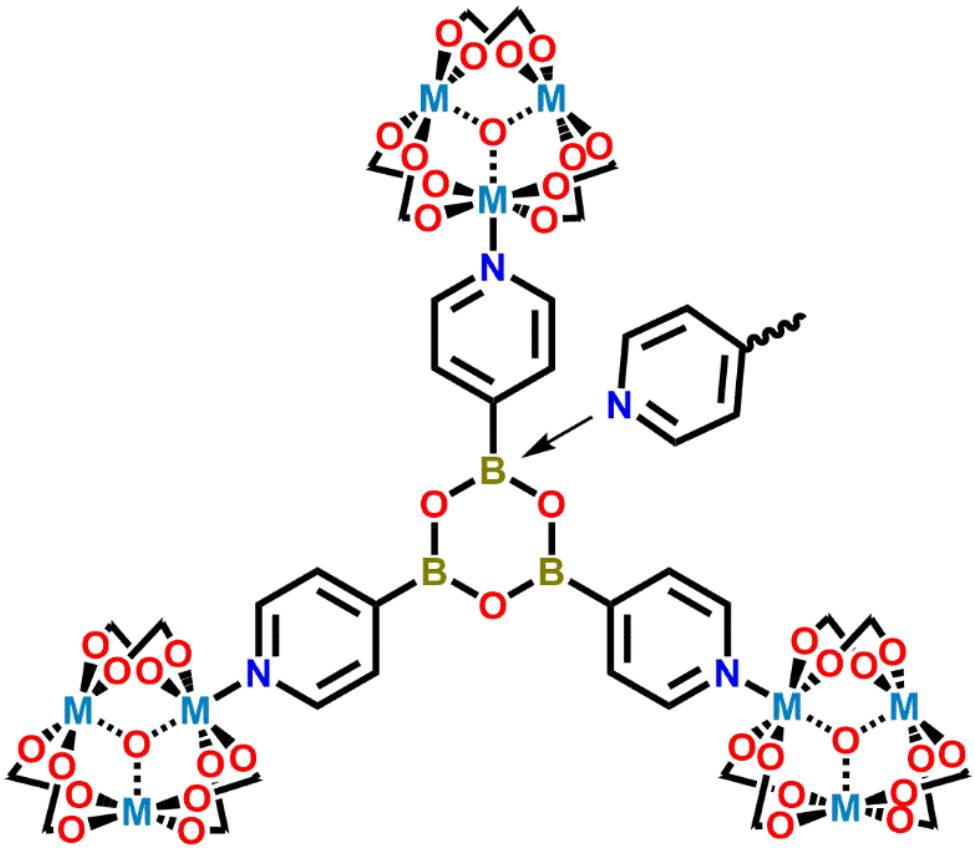

Figure 2.2 The side reaction, pyridine-boron coordination, hinders the formation of tpb in the absence of carboxylate-metal trimers.

2.2 Experimental Section

2.2.1 Chemicals and General Methods

All chemicals and solvents in this work were purchased and used without further purification. $MgCl_2 \cdot 6H_2O$, $FeCl_3 \cdot 6H_2O$, $CoCl_2 \cdot 6H_2O$, $NiCl_2 \cdot 6H_2O$, $InCl_3$, 1,4-terephthalic acid (H_2BDC), 2-aminobenzene-1,4-dicarboxylic acid (NH_2-H_2BDC), 2-nitrobenzene-1,4-dicarboxylic acid (NO_2H_2BDC), naphthalene-2,6-dicarboxylic acid (26-H_2NDC), 2,4,6-tri(4-pyridyl)-1,3,5-triazine (tpt), N, N-dimethylacetamide (DMA), N, N-dimethylformamide (DMF) and 1,3-dimethyl-3,4,5,6-tetrahydro-2(1H)-pyrimidinone (DMPU) were purchased from Aldrich American Co. without any purification. Pyridine-4-boronic acid (96%) was purchased from Oakwood Chemical Co.

Powder X-ray diffraction.

Powder X-ray diffraction (PXRD) data was collected on a Bruker D8 Advance powder diffraction meter with CuKα radiation (40 kV, 40 mA, λ = 1.5418 Å) Data was collected with a step size of 0.02° and counting time is 1s per step. The simulated powder pattern was calculated from SXRD data and processed by the Mercury 3.1 program provided by the CCDC.

Single crystal X-ray diffraction.

The single crystal samples will be performed on a Bruker Smart APEX II CCD area diffractometer with nitrogen-flow temperature controller using graphite-monochromated MoKα radiation (λ =0.71073 Å), operating in the ω and φ scan mode. The structure was

solved by direct methods followed by successive difference Fourier methods. All non-hydrogen atoms were refined anisotropically. Computations were performed using OLEX2 and final full-matrix refinements were against F^2. The M^{3+}/M^{2+} ratio was estimated from the occupancy refinement with single crystal X-ray diffraction data.

Energy dispersive spectroscopy (EDS).

The semi-quantitative elemental analyses of different heterometallic MOF samples were performed by using a FEI NNS450 field emission scanning electron microscope equipped with 50 mm^2 X-Max50 SDD energy dispersive spectroscopy (EDS) detector. Data acquisition was performed with an accelerating voltage of 15 kV and 20 s accumulation time.

Gas adsorption.

Gas sorption isotherms (C_2H_2, C_2H_4, C_2H_6, CO_2 and CH_4) of all MOFs were measured on a volumetric instrument Micromeritics ASAP 2020. The samples were activated by evacuation (10^{-3} torr) at 120 °C for 10 h and then at 150 °C for 10 h. CPM-100d was activated by evacuation (10^{-3} torr) at 100 °C for 10 h and 120 °C for 10 h. NH_3 sorption was performed on an Intelligent gravimetric analyzer (IGA 001, Hiden, UK) at 298 K. All compounds are regenerated by evacuation (10^{-3} torr) at 120 °C for 5h before recycling test.

Thermal analysis.

The simultaneous thermal analysis was performed on TA Instruments TGA-Q500 in the temperature range of 30 °C to 900 °C under the N_2 flow. The flow rate was controlled

at 60 ml/min. The temperature is increasing at 5 °C/min. All seven compounds are performed on TGA-Q500 after activation on ASAP 2020.

Isosteric heats of adsorption.

The isosteric heats of adsorption (Q_{st}) are obtained from the one certain gas component sorption isotherms at 273 K and 298 K using Clausius–Clapeyron equation (1):

$$Q_{st} = R \{[\partial \ln p]/[\partial (1/T)]\}q \qquad (1)$$

where R is the universal gas constant, q is the amount of a certain gas loaded at pressure p and temperature T. These calculations are done through the "Heat of Adsorption" calculated function embedded in the software supplied by Micromeritics ASAP 2020 surface-area and pore-size analyzer machine.

DFT calculations.

DFT calculations were performed to optimize the structures of the cleaved tpb molecule, as well as the interaction between tpb and NH_3 molecules using the DMol^3 module implemented in the Materials Studio software. The Perdew–Burke–Ernzerhof (PBE) exchange-correlation potential combined with the double numerical basis set containing polarization function (DNP) was utilized in the calculations. A self-consistent field (SCF) procedure was performed with a convergence threshold of 10^{-6} au on the energy and electron density.[18] The direct inversion of the iterative subspace technique developed by Pulay was utilized with a subspace size of 6 to increase the speed of SCF convergence on these systems. Convergence threshold parameters for optimization were 10^{-6} Ha (energy), 5×10^{-4} Ha/Å (gradient), and 5×10^{-3} Å (displacement), respectively.

The real-space global cutoff radius was set as 6.0 Å. The interaction energies were computed from Equation (2):

$$\Delta E = E_{\mathrm{tpb-NH3}} - E_{\mathrm{tpb}} - E_{\mathrm{NH3}} \qquad (2)$$

where E represents the energy of the system after full geometry relaxation, $E_{\mathrm{tpb-NH3}}$ is the total energy of the tpb and NH_3, E_{tpb} and E_{NH3} are the energies of the isolated tpb and NH_3 molecule, respectively.

2.2.2 Synthesis Methods

Synthesis of CPM-100a-InCo [$In_{1.8}Co_{1.2}(OH)_{0.2}O_{0.8}(BDC)_3tpb$]

In a 21 ml glass vial, 50 mg of $CoCl_2 \cdot 6H_2O$, 87 mg of $InCl_3$, 63 mg of H_2BDC and 36 mg of pyridine-4-boronic acid were dissolved in mixture of 6.0 g of DMF and 1.2 g of toluene. After stirring overnight, the vial was sealed and placed in a 120 °C oven for 3 days. Pink single crystals with elongated hexagonal bipyramid shape were grown under colorless flocs and pure samples were obtained after removing flocs.

Synthesis of CPM-100a-FeMg [$Fe_{1.74}Mg_{1.26}(OH)_{0.26}O_{0.74}(BDC)_3tpb$]

In a 21 ml glass vial, 109 mg of $FeCl_3 \cdot 6H_2O$, 40 mg of $MgCl_2 \cdot 6H_2O$, 64 mg of H_2BDC and 47 mg of pyridine-4-boronic acid were dissolved in mixture of 8.0 g of DMF and 0.2 g of toluene. After stirring overnight, the vial was sealed and placed in a 120 °C oven for 5 days. Green hexagonal crystals were grown on the wall and pure samples were obtained after discarding unknow solid on the bottom and washing with DMF.

Synthesis of CPM-100a-FeNi [$Fe_{1.6}Ni_{1.4}(OH)_{0.4}O_{0.6}(BDC)_3tpb$]

In a 21 ml glass vial, 109 mg of $FeCl_3 \cdot 6H_2O$, 45 mg of $NiCl_2 \cdot 6H_2O$, 66 mg of H_2BDC and 38 mg of pyridine-4-boronic acid were dissolved in mixture of 11.0 g of DMF and 2.4 g of toluene. After stirring overnight, the vial was sealed and placed in a 120 °C oven for 5 days. Yellow crystals with elongated hexagonal bipyramid shape were obtained after washing with DMF for three times and phase purity was identified by PXRD.

Synthesis of CPM-100b [$In_{1.7}Co_{1.3}(OH)_{0.3}O_{0.7}(NH_2BDC)_3tpb$]

In a 21 ml glass vial, 52 mg of $CoCl_2 \cdot 6H_2O$, 84 mg of $InCl_3$, 70 mg of NH_2-H_2BDC and 39 mg of pyridine-4-boronic acid were dissolved in mixture of 4.1 g of DMA and 0.6 g of toluene. After stirring overnight, the vial was sealed and placed in a 120 °C oven for 3 days. Pink single crystals with elongated hexagonal bipyramid shape were obtained after washing with DMF for three times.

Synthesis of CPM-100c [$In_{1.1}Co_{1.9}(OH)_{0.9}O_{0.1}(NO_2BDC)_3tpb$]

In a 21 ml glass vial, 53 mg of $CoCl_2 \cdot 6H_2O$, 88 mg of $InCl_3$, 84 mg of NO_2-H_2BDC and 45 mg of pyridine-4-boronic acid were dissolved in mixture of 6 g of DMA and 0.3 g of toluene. After stirring overnight, the vial was sealed and placed in a 120 °C oven for 3 days. Pink single crystals with hexagonal shape were obtained after washing with DMF for three times.

Synthesis of CPM-100d [$In_{1.5}Co_{1.5}(OH)_{0.5}O_{0.5}(26NDC)_3tpb$]

In a 21 ml glass vial, 49 mg of $CoCl_2 \cdot 6H_2O$, 91 mg of $InCl_3$, 84 mg of 26-H_2NDC and 46 mg of pyridine-4-boronic acid were dissolved in mixture of 8 g of DMF and 0.7 g of toluene. After stirring overnight, the vial was sealed and placed in a 120 °C oven for 3

days. Pink single crystals with elongated hexagonal bipyramid shape were obtained after washing with DMF for three times.

Synthesis of tpt-InCo-BDC [$In_{1.2}Co_{1.8}(OH)_{0.8}O_{0.2}(BDC)_3$tpt]

In a 21 ml glass vial, 49 mg of $CoCl_2 \cdot 6H_2O$, 93 mg of $InCl_3$, 63 mg of H_2BDC and 62 mg of tpt were dissolved in mixture of 5 g of DMA and 1 g of DMPU. After stirring overnight, the vial was sealed and placed in a 130 °C oven for 5 days. Orange crystals with hexagonal shape were obtained after washing with DMA for three times.

2.3 Results and Discussion

2.3.1 Structure Analysis

The tpb-**pacs** family has a general framework formula of $[(M1)_{1+x}(M2)_{2-x}(OH)_{1-x}(O)_x(L1)_3](L2)$, where $[(M1)_{1+x}(M2)_{2-x}(OH)_{1-x}(O)_x(L1)_3]$ represents the parent **acs** frameworks (M1 = In^{3+}, Fe^{3+}, M2 = Co^{2+}, Mg^{2+}, Ni^{2+}, L1 = BDC, NH_2BDC, NO_2BDC, 26NDC, in CPM-100a, -100b, -100c, -100d, respectively). CPM-100a has been made in different metal combinations, denoted as CPM-100a-InCo, CPM-100a-FeMg, CPM-100a-FeNi. L2 is the condensation product tpb. It is worth noting that tpb was previously not known to exist. It is the synergistic effect between **acs** net and pore partitioning agent that enables its formation. A tpt-**pacs** CPM $[In_{1.2}Co_{1.8}(OH)_{0.8}O_{0.2}(BDC)_3]$tpt, denoted as tpt-InCo-BDC (or CPM-83-InCo) was also prepared. [7, 14] The structures of CPM-100a, CPM-100b, CPM-100c, CPM-100d, and tpt-InCO-BDC were characterized by Single-crystal X-ray diffraction and refined by OLEX2 (Table 2.1-2.4). The metal ratios in the as-mentioned

five compunds were determined by SCXRD. The metal ratios of all seven compounds were comfirmed by EDS analysis. (Figure 2.3) Phase purity of of all seven compounds were confirmed by comparing PXRD paterns and simulated resulted calculated from cif files (Figure 2.4).

The characteristic feature of the **pacs** platform is the variety of the pore-partitioning agents and design strategies. The formation of tpt-**pacs** is an OMS-eliminating process (OMS = Open Metal Site) due to the formation of a 3,9-connected net with three open metal sites coordinated by pyridinyl groups from tpt. The trz-**pacs** represents an OMS-shifting design. While trz-**pacs** is also a 3,9-connected framework in which azolate ligands occupy all open metal sites on the parent framework, the open metal sites formed on metal-ligand complex can reach up to 18 per unit cell in the channel centers. A totally different feature is shown in this work through pore space partition. Through the MOF-COF synergistic reaction, open metal sites on the framework are occupied by pyridyl groups, and boron Lewis acid sites are exposed through boronic acid condensation. (Figure 2.5) The new partitioning agent tpb contains three B sites, providing 6 Lewis acid sites (LAS) per unit cell (~1.55 LAS/nm^3). Boron Lewis acid sites are favorable adsorbents for Lewis base gases like ammonia due to the B-N coordinative process.

Table 2.1 Crystal Data of CPM-100.

Code [a]	Formular [b]	a, b (Å)	c (Å)	R (F)
CPM-100a	$In_{1.8}Co_{1.2}(OH)_{0.2}O_{0.8}(BDC)_3tpb$	17.015 (5)	15.303 (9)	0.0560
CPM-100b	$In_{1.7}Co_{1.3}(OH)_{0.3}O_{0.7}(NH_2BDC)_3tpb$	17.055 (2)	15.333 (5)	0.0617
CPM-100c	$In_{1.1}Co_{1.9}(OH)_{0.9}O_{0.1}(NO_2BDC)_3tpb$	17.077 (3)	15.153 (3)	0.0695
CPM-100d	$In_{1.5}Co_{1.5}(OH)_{0.5}O_{0.5}(26NDC)_3tpb$	17.043 (3)	21.000 (4)	0.0807

[a] space group of all four compounds: *P6₃/mmc*, [b] BDC^{2-} = benzene-1,4-dicarboxylate, NH_2BDC^{2-} = 2-aminobenzene-1,4-dicarboxylate, NO_2BDC^{2-} = 2-nitrobenzene-1,4-dicarboxylate, $26NDC^{2-}$ = naphthalene-2,6-dicarboxylate, tpb = 2,4,6-tri(4-pyridinyl)-1,3,5-boroxine.

Table 2.2 Crystal data and refinement for CPM-100a and CPM-100b.

Sample code	CPM-100a	CPM-100b
Empirical framework formula	$C_{39}H_{24.2}B_3Co_{1.2}In_{1.8}N_3O_{16}$	$C_{39}H_{27.3}B_3Co_{1.3}In_{1.7}N_6O_{16}$
Formula weight	1100.4	1139.9
Temperature / K	174	296.15
Crystal system	hexagonal	hexagonal
Space group	$P6_3/mmc$	$P6_3/mmc$
a/Å	17.0153(5)	17.055(2)
b/Å	17.0153(5)	17.055(2)
c/Å	15.3032(9)	15.333(5)
α/°	90	90
β/°	90	90
γ/°	120	120
Volume / $Å^3$	3837.0(3)	3862.4(16)
Z	2	2
ρ_{calc} g/cm^3	0.949	0.992
μ/mm^{-1}	0.828	0.859
F (000)	1082	1129
Radiation	MoKα (λ = 0.71073)	MoKα (λ = 0.71073)
2Θ range for data collection	3.838 to 53.28	3.828 to 50.006
Completeness	98.2%	95.9%
Adsorption Correction	Multi-scan	Multi-scan
Refinement method	Full-matrix least-squares on	Full-matrix least-squares on
Independent reflections	1517 [R_{int} = 0.0712]	1264 [R_{int} = 0.1536
Data/restraints/parameters	1517/72/70	1264/66/77
Goodness-of-fit on F^2	1.115	0.967
Final R indexes [I>=2σ (I)]	R_1 = 0.0560, wR_2 = 0.1642	R_1 = 0.0617, wR_2 = 0.1485
Final R indexes [all data]	R_1 = 0.0687, wR_2 = 0.1723	R_1 = 0.1018, wR_2 = 0.1715
Largest diff. peak/hole / e $Å^{-3}$	1.75/-1.01	0.82/-0.67
CCDC deposition number	1894561	1894562

Table 2.3 Crystal data and refinement for CPM-100c and CPM-100d.

Sample code	CPM-100c	CPM-100d
Empirical framework formula	$C_{39}H_{21.9}B_3Co_{1.9}In_{1.1}N_6O_{22}$	$C_{51}H_{42.5}B_3Co_{1.5}In_{1.5}N_3O_{16}$
Formula weight	1196.9	1245.6
Temperature/K	296.15	296.15
Crystal system	hexagonal	hexagonal
Space group	$P6_3/mmc$	$P6_3/mmc$
a/Å	17.077(3)	17.043(3)
b/Å	17.077	17.043
c/Å	15.153(3)	21.000(4)
α/°	90	90
β/°	90	90
γ/°	120	120
Volume/Å^3	3826.6(16)	5282.5(19)
Z	2	2
ρ_{calc} g/cm^3	1.063	0.768
μ/mm^{-1}	0.838	0.594
F(000)	1197	1204
Radiation	MoKα (λ = 0.71073)	MoKα (λ = 0.71073)
2Θ range for data collection/°	2.754 to 49.986	3.372 to 44.948
Completeness	99.4% (to theta full =	99.5% (to theta full = 22.474)
Adsorption Correction	Multi-scan	Multi-scan
Refinement method	Full-matrix least-squares on	Full-matrix least-squares on
Independent reflections	1298 [R_{int} = 0.1154]	1328 [R_{int} = 0.1078]
Data/restraints/parameters	1298/72/99	1328/42/95
Goodness-of-fit on F^2	1.043	1.09
Final R indexes [I>=2σ (I)]	R_1 = 0.0695, wR_2 = 0.1992	R_1 = 0.0807, wR_2 = 0.2090
Final R indexes [all data]	R_1 = 0.0965, wR_2 = 0.2160	R_1 = 0.1125, wR_2 = 0.2342
Largest diff. peak/hole / e Å^{-3}	1.00/-0.84	0.84/-0.52
CCDC deposition number	1894563	1894564

Table 2.4 Crystal data and refinement for tpt-InCo-BDC.

Sample code	tpt-InCo-BDC
Sample code	tpt-InCo-BDC
Empirical framework formula	$C_{42}H_{24.8}Co_{1.8}In_{1.2}N_6O_{13}$
Formula weight	1065
Temperature/K	296.15
Crystal system	hexagonal
Space group	$P6_3/mmc$
a/Å	16.945(5)
b/Å	16.945
c/Å	15.329(5)
α/°	90
β/°	90
γ/°	120
Volume/Å^3	3812(3)
Z	2
ρ_{calc}g/cm^3	0.931
μ/mm^{-1}	0.797
F(000)	1062
Radiation	MoKα (λ = 0.71073)
2Θ range for data collection/°	3.842 to 46.514
Completeness	99.3% (to theta full = 23.257)
Adsorption Correction	Multi-scan
Refinement method	Full-matrix least-squares on F^2
Independent reflections	1062 [R_{int} = 0.0784]
Data/restraints/parameters	1062/40/68
Goodness-of-fit on F^2	1.065
Final R indexes [I>=2σ(I)]	R_1 = 0.0332, wR_2 = 0.0802
Final R indexes [all data]	R_1 = 0.0449, wR_2 = 0.0844
Largest diff. peak/hole / e Å^{-3}	0.34/-0.34

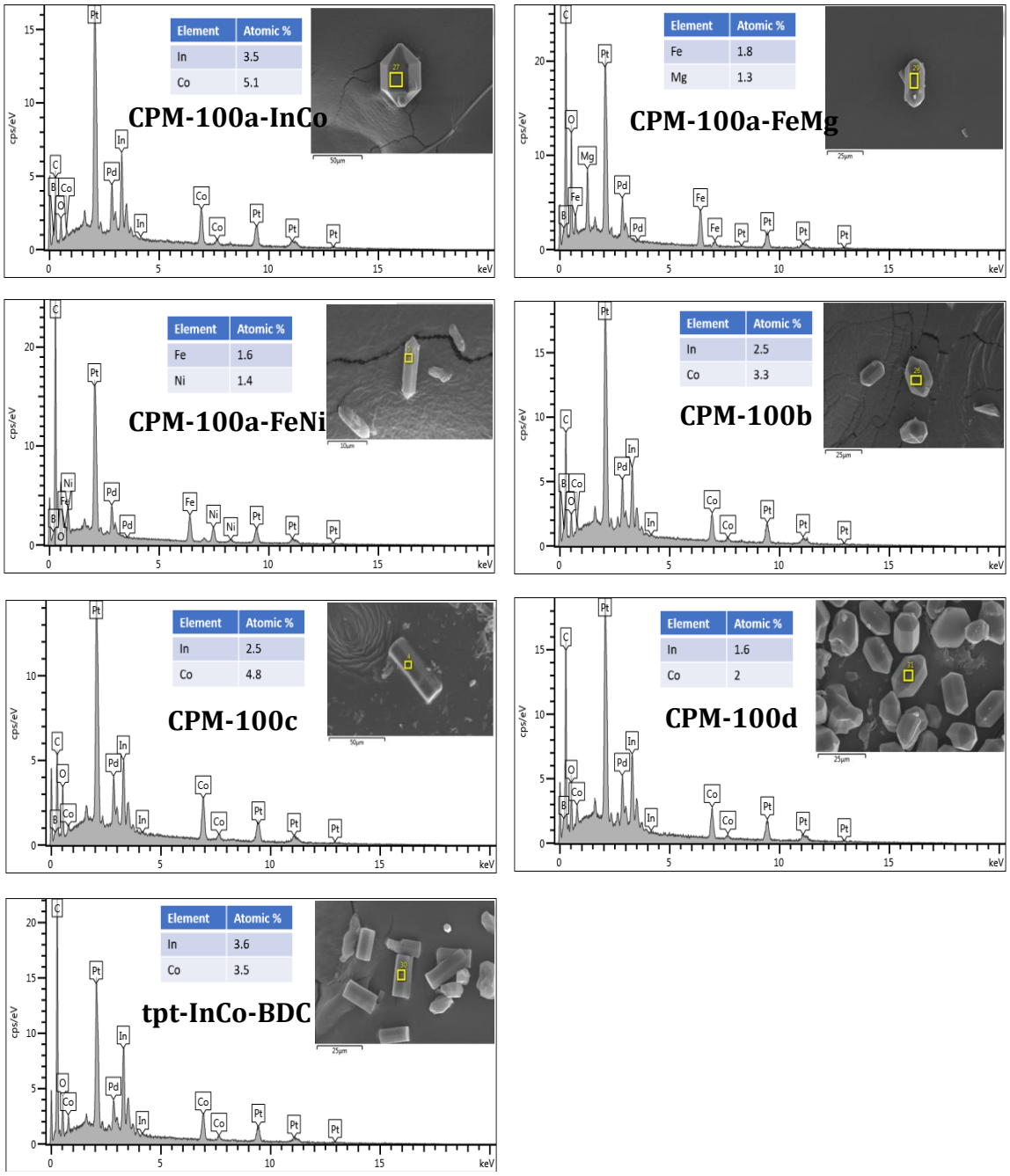

Figure 2.3 Metal ratios of tpb-**pacs** and tpt-**pacs** samples analyzed by EDS with SEM images showing corresponding crystals.

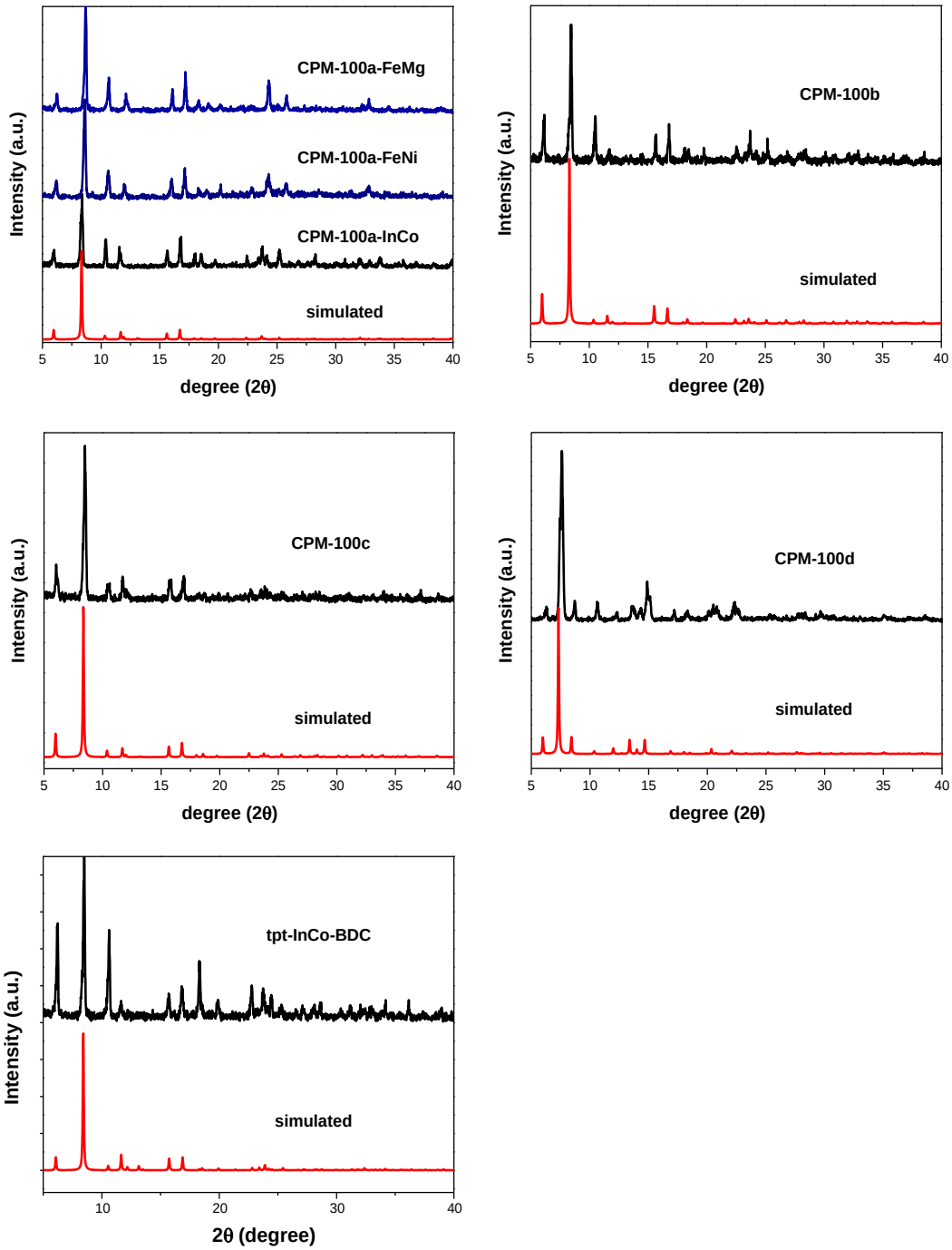

Figure 2.4 Powder XRD patterns from experiment and simulation for tpb-**pacs** and tpt-**pacs** compounds.

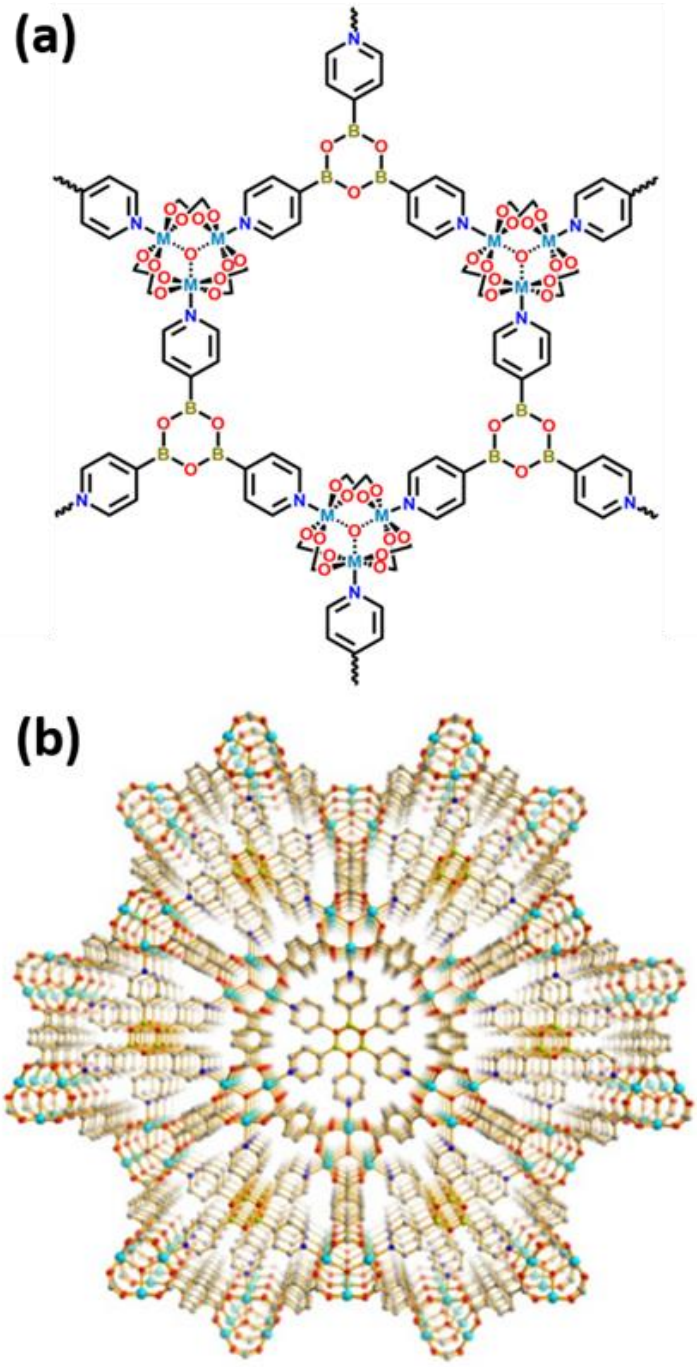

Figure 2.5 (a) Illustration of the alternative tpb and metal-cluster trimers in the ab layer of CPM-100. (b) Structure view from the c axis.

2.3.2 Isotherm Gas Sorption Studies

Newly synthesized CPMs are chosen as adsorbents for gas adsorption studies. C_2H_2, C_2H_4, C_2H_6, CH_4, CO_2 and NH_3 uptakes were performed with seven compounds. The following systematic trends among these new materials were explored: (1) changing L1 ligands with fixed M1/M2 combination (In/Co), (2) changing M1/M2 combinations (In/Co, Fe/Mg, Fe/Ni) with fixed L1 (BDC), (3) changing pore-partitioning agents (tpt or tpb) with fixed L1 (BDC) and M1/M2 (In/Co).

Isotherm gas uptakes were performed under 273 K and 298 K after the activation of each sample mentioned in 2.2.1. The solvents and unreacted chemicals were removed from the pores as shown in Figure 2.6. There is no obvious weight loss below 200 ° C under N_2 atmosphere. It is notable that the gas uptakes of five gases in tpb-**pacs** materials are dramatically enhanced compared to **acs** materials (Figure 2.8-2.9, Table 2.5). At 1 bar and 273 K, the CO_2 uptakes are increased from 3.96 to 6.32 mmol/g in tpb-**pacs**, which is far beyond the best performance gas sorbent in **acs** type Mg_2V-MIL-88 (4.25 mmol/g) (Figure 2.9c).[5] The C_2H_2 uptake can be tuned from 5.61 mmol/g to 10.45 mmol/g at 1 bar and 273 K. (Figure 2.8a) Under the same condition, the C_2H_2 uptake of CPM-100a-FeMg is nearly two times of Mg_2V-MIL-88 (5.25mmol/g at 273 K and 3.28 mmol/g at 298 K).[5] This effective gas sorption enhancement is attributed to the pore-partitioning agent tpb, which increases the robustness of the framework as well as the number of binding sites.[15] The C_2H_4 and C_2H_6 (1bar, 273 K) uptakes can be enhanced from 3.8 mmol/g to 6.89

mmol/g and 3.39 mmol/g to 7.5 mmol/g, respectively (Figure 2.8c, e). The uptake of CH_4 is tuned from 0.55 mmol/g to 1.71 mmol/g at 1 bar and 273 K (Figure 2.9a).

In the L1 ligand comparison, BDC version possesses better gas uptake performances than the other three versions. This is because there is no strong interaction after add amino groups and nitro groups in NH_2BDC and NO_2BDC versions. On the contrary, the addition of functional group occupies the pore size and lowered surface areas leading to a decrease in different gas uptakes (Figure 2.11, Table 2.5). The 26NDC version with a lengthened ligand possesses higher surface area compared to that of in BDC version, however, the host-guest interactions were weakened because of the larger pore size (Figure 2.12).

In the metal cluster comparison, FeMg cluster is the best one among all three clusters in different gas uptakes. The reasons come from the following two aspects: 1. The surface area of FeMg version is as high as 1972 m^2/g, compared to 1585 and 1579 m^2/g in InCo and FeNi versions, respectively. 2. The density of FeMg is lower than InCo and FeNi combinations. The higher surface area and lower density lead CPM-100a-FeMg a powerful gas adsorbent.

It is worth to mention that tpb version is less efficient than tpt version in all five gas uptakes in this study (Figure 2.10). The surface areas of these two compounds are very close to each other (Figure 2.11, Table 2.5). The reasons of the difference between these two versions are proposed as below:

The triazine in tpt is a π electron sufficient six-membered ring, which easily interacts with π electron contained gas molecules, such as C_2H_2, C_2H_4, and CO_2. This π- π

interaction leads tpt version higher uptakes compared to tpb version of **pacs** materials. This can be further confirmed by isosteric heat of adsorptions of C_2H_2 and C_2H_4 in Figure 2.12.

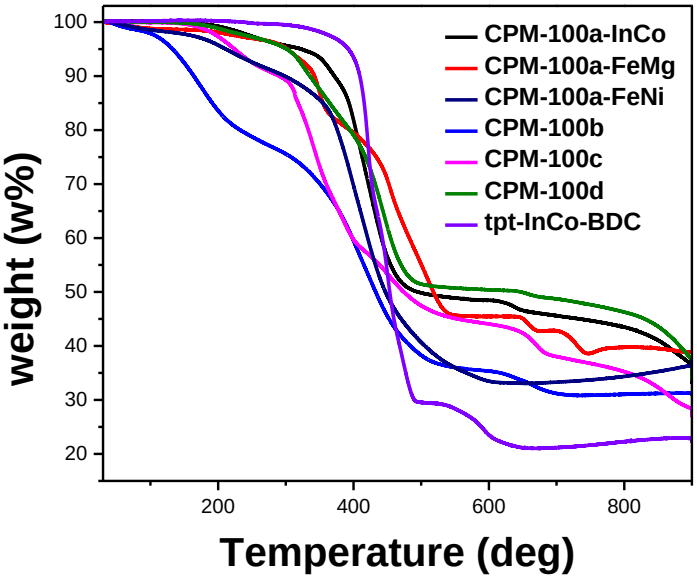

Figure 2.6 TGA figures for tpb-**pacs** and tpt-**pacs** compounds.

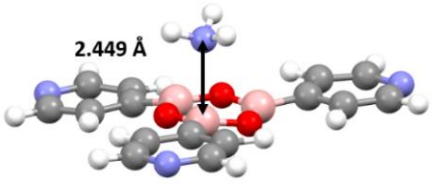

Figure 2.7 Interaction between tpb and NH_3.

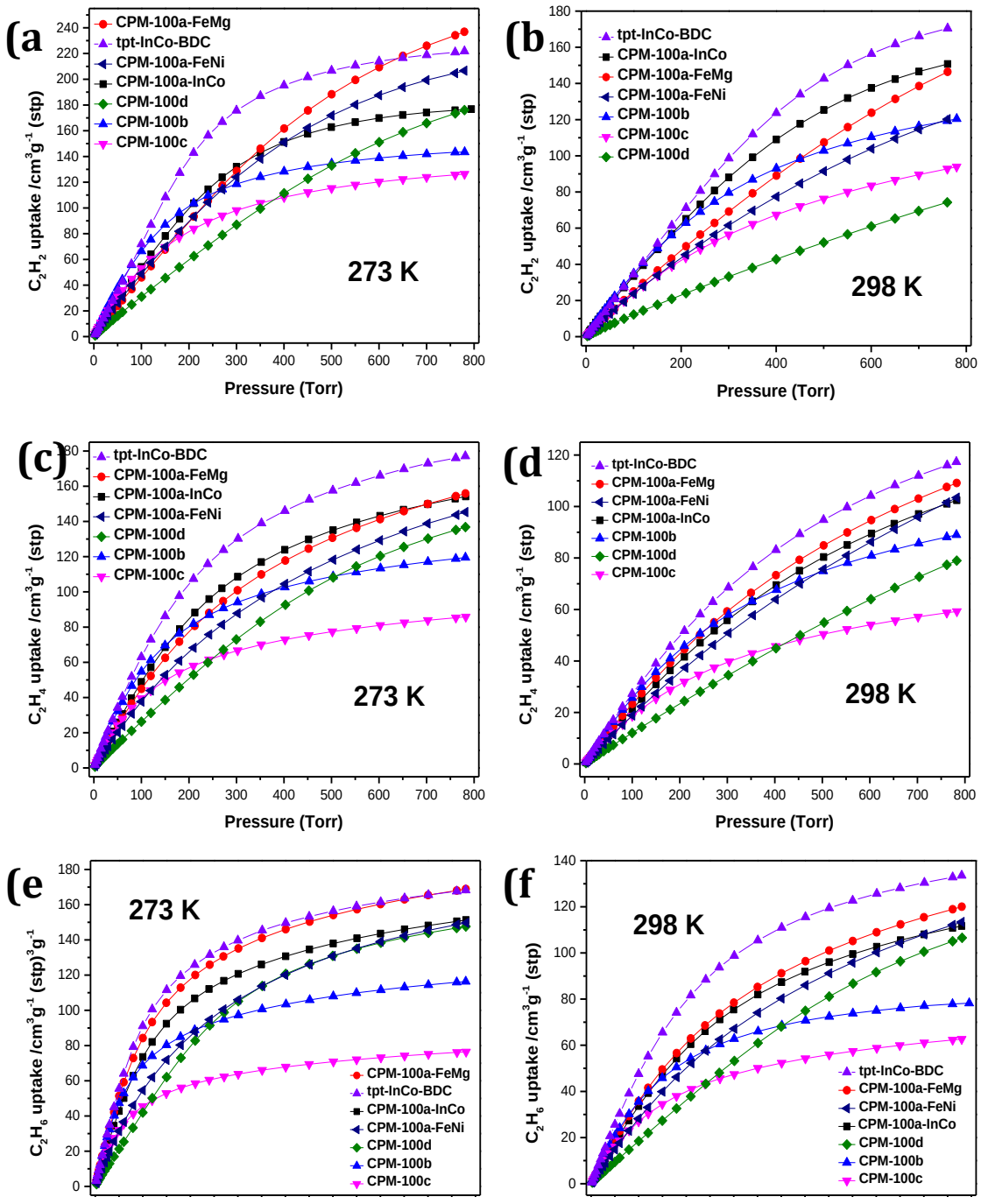

Figure 2.8 C_2H_2, C_2H_4 and C_2H_6 sorption isotherm at 273 K and 298 K for tpb-**pacs** and tpt-**pacs** compounds.

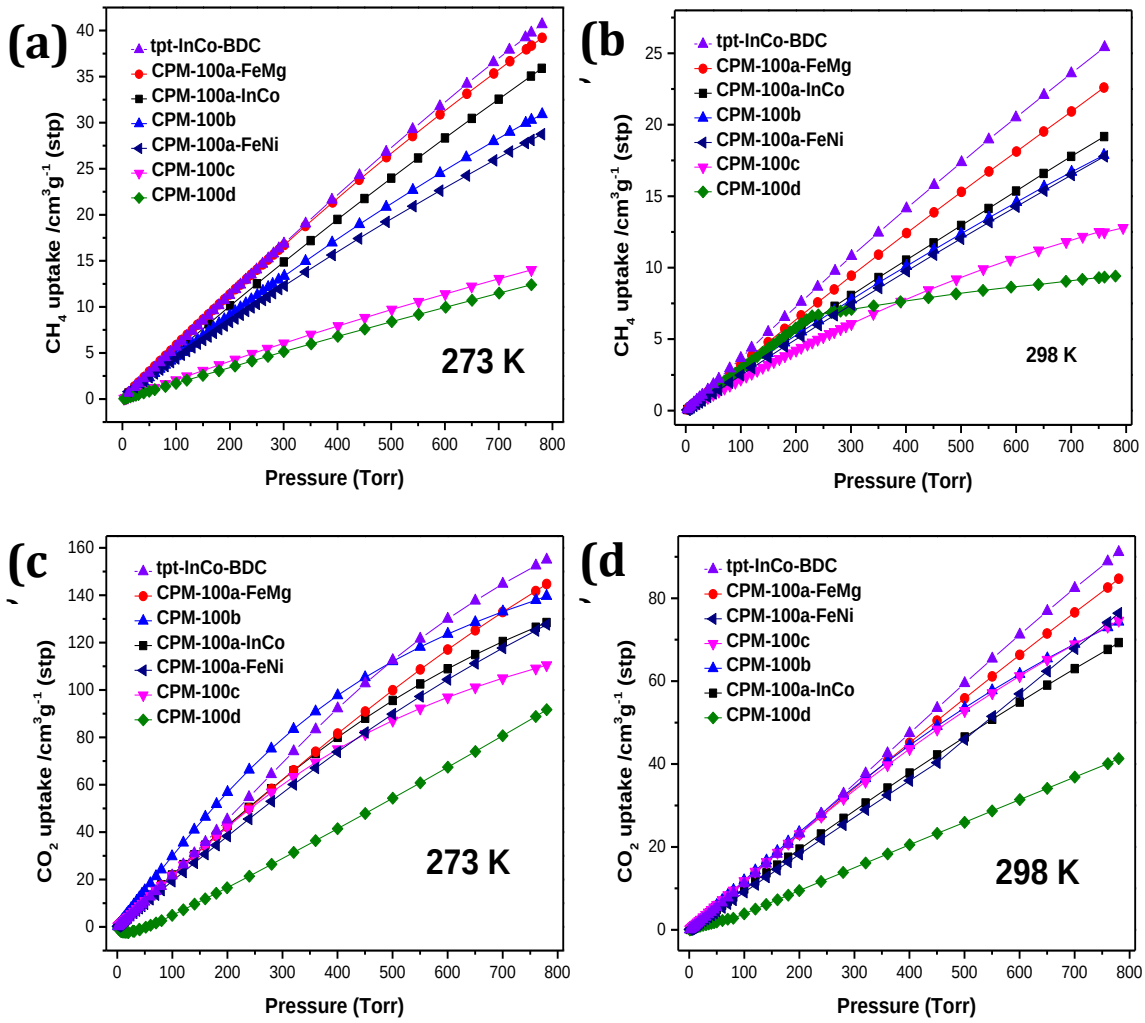

Figure 2.9 CH_4 and CO_2 sorption isotherm at 273 K and 298 K for tpb-**pacs** and tpt-**pacs** compounds.

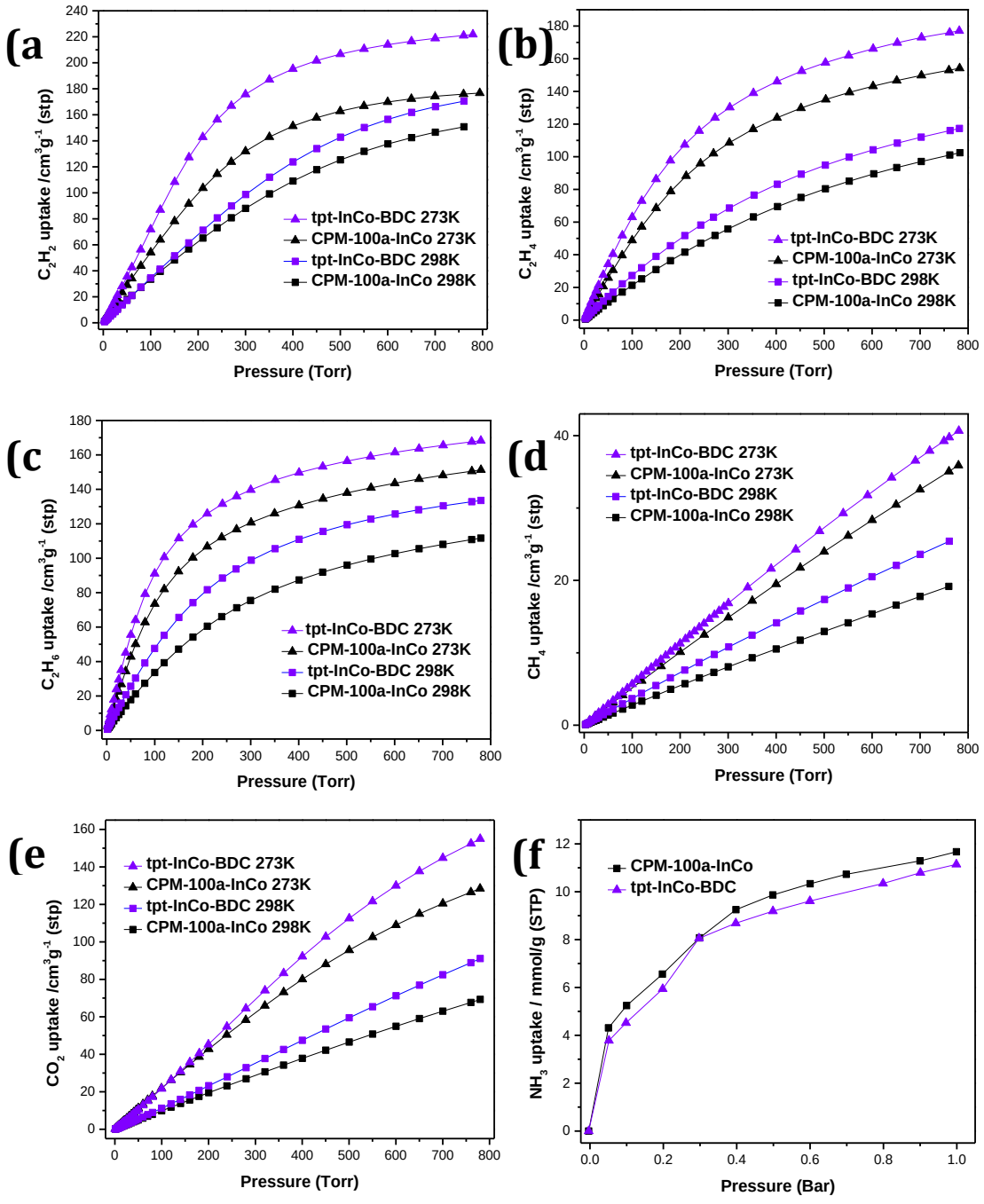

Figure 2.10 Comparison between CPM-100a-InCo and tpt-InCo-BDC for (a) C_2H_2, (b) C_2H_4, (c) C_2H_6, (d) CH_4 (e) CO_2 adsorption at 273 K and 298 K and (f) NH_3 adsorption at 298 K.

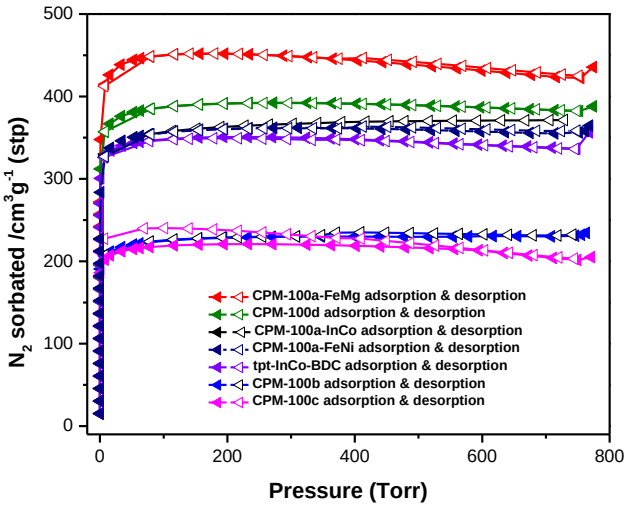

Figure 2.11 N_2 sorption isotherm at 77 K for tpb-**pacs** and tpt-**pacs** compounds.

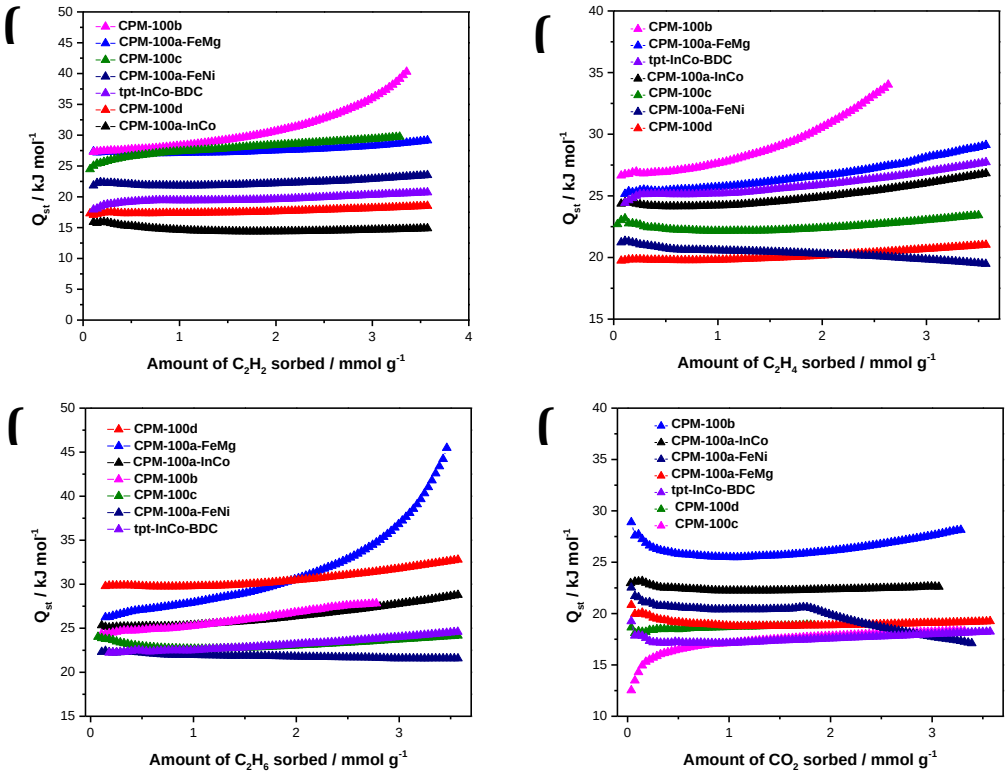

Figure 2.12 Isosteric heat of adsorption for tpb-**pacs** and tpt-**pacs** compounds.

For NH_3, at 1 bar and 298 K, the NH_3 uptake can be tuned from 7.85 mmol/g to 12.56 mmol/g following the order of 26NDC, BDC, NO_2BDC, to NH_2BDC, and from 11.66 mmol/g to 13.01 mmol/g following the order of In/Co, Fe/Mg, Fe/Ni (Figure 2.14a). There is no obvious adsorption loss after 4 cycles (Table 2.6). The NH_3 packing density in CPM-100b and CPM-100c (0.598 g/cm^3 and 0.597 g/cm^3) is comparable to the top two materials MFM-300(Al) and Co_2Cl_2BBTA (0.622 g/cm^3 and 0.610 g/cm^3) (Figure 2.14b, Table 2.7).[16] According to the DFT calculation result, the adsorption site B possesses with a large binding energy of -43 kJ/mol. The distance between N in ammonia and B in tpb is ~2.45 Å, indicating a strong interaction between B and N (Figure 2.7), which results in an adsorption enhancement compared to tpt-**pacs** materials (Figure 2.10f).

It is important to notice that the PXRD patterns lose their crystallinity after NH_3 adsorption in those compounds containing transition metals such as Co and Ni (Figure 2.13). This is because ammonia replaced carboxylate site and formed ammonia-metal complex destroyed the structure.

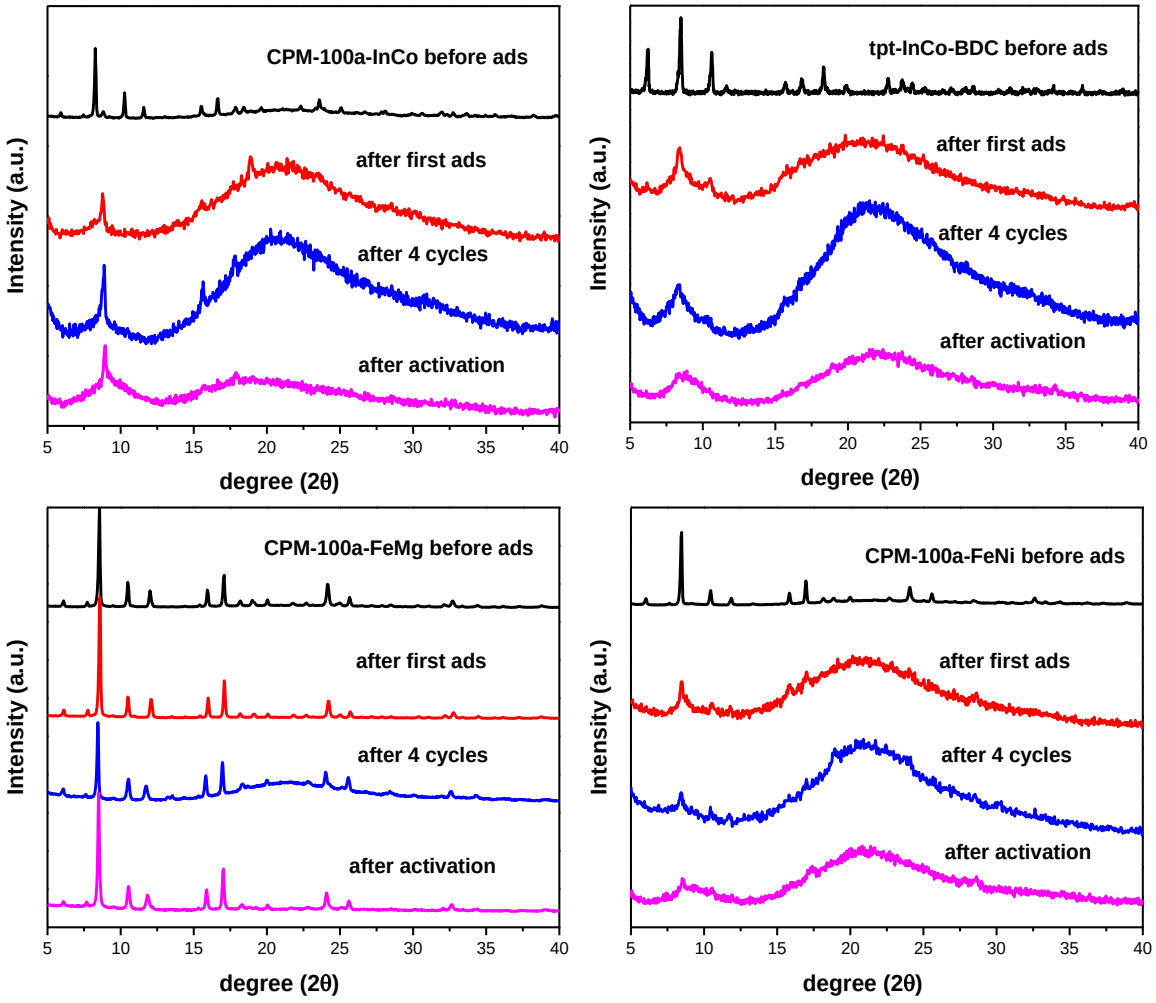

Figure 2.13 PXRD patterns for CPM-100a-InCo, FeMg, FeNi and tpt-InCo-BDC before and after NH_3 sorption and after activation.

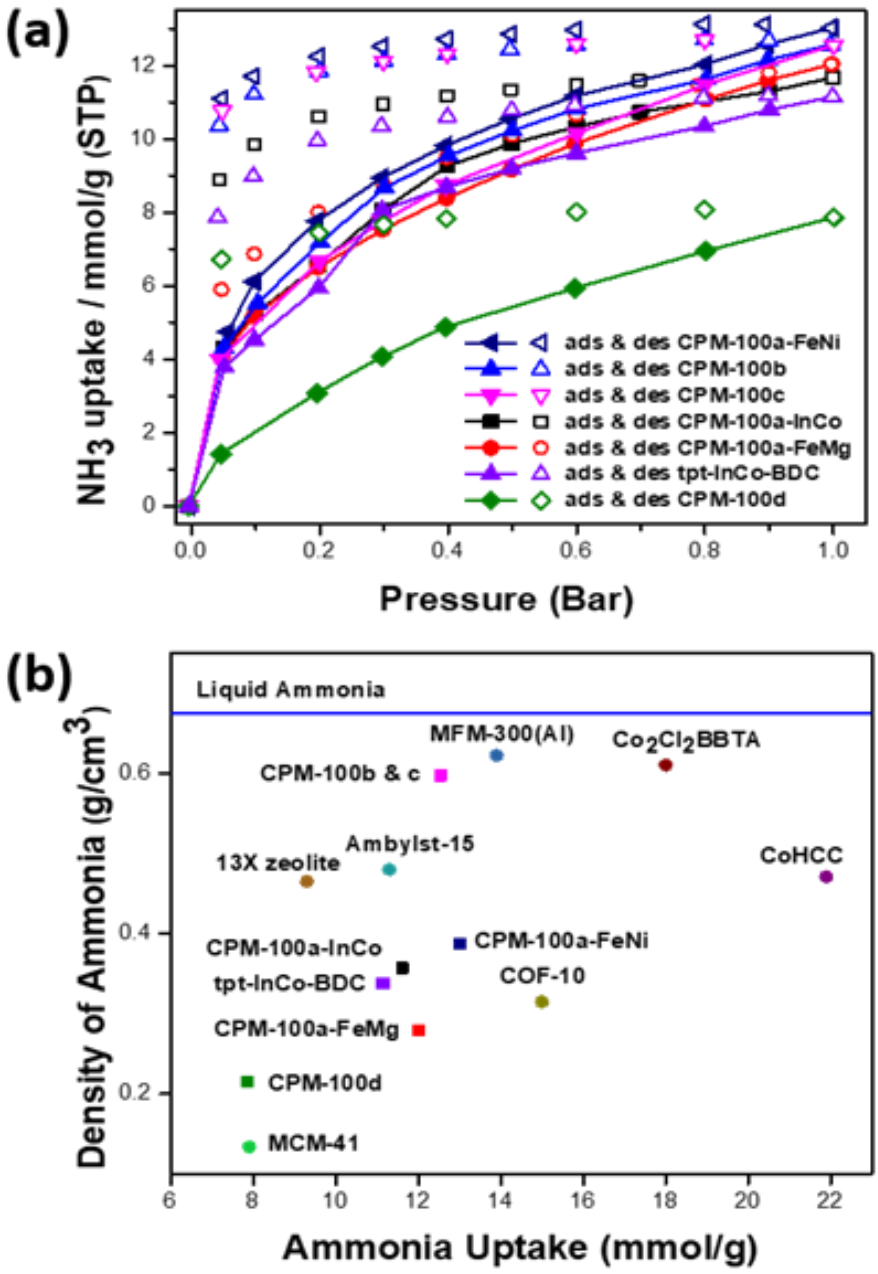

Figure 2.14 (a) NH_3 sorption isotherm at 273 K, (b) comparison of density of NH_3 between CPM-100, other materials and liquid ammonia.

Table 2.5. Summary of isotherm adsorption results for seven compounds.

Compound Code	CPM-100a-InCo	CPM-100a-FeMg	CPM-100a-FeNi	CPM-100b	CPM-100c	CPM-100d	tpt-InCo-BDC
S_A Langmuir (m^2/g)	1585	1972	1579	1001	965	1712	1532
S_A BET (m^2/g)	1388	1425	1139	721	696	1236	1106
Pore Volume (cm^3/g)	0.556	0.733	0.571	0.357	0.357	0.621	0.563
NH_3 298 K, 1 bar	11.66	12.02	13.01	12.56	12.54	7.85	11.14
NH_3 cycle 2 (mmol/g)	11.15	11.69	13.01	10.55	11.03	5.34	10.87
NH_3 cycle 3 (mmol/g)	11.44	11.33	13.48	10.67	9.58	5.22	10.33
NH_3 cycle 4 (mmol/g)	11.12	11.31	13.75	11.13	11.64	4.89	10.03
Adsorption Loss (4	4.7%	5.8%	0	11.3%	7.2%	37.7%	10.1%
C_2H_2 273 K, 1 atm	7.85	10.45	9.14	6.39	5.61	7.74	9.86
C_2H_2 298 K, 1 atm	6.73	6.53	5.36	5.32	4.14	3.31	7.61
Q_{st}^0 (kJ/mol)	15.91	17.30	21.82	27.37	27.82	24.46	17.93
C_2H_4 273 K, 1 atm	6.82	6.89	6.41	5.30	3.80	6.03	7.85
C_2H_4 298 K, 1 atm	4.51	4.80	4.53	3.93	2.62	3.45	5.18
Q_{st}^0 (kJ/mol)	24.36	19.75	21.22	25.15	26.65	22.69	24.42
C_2H_6 273 K, 1 atm	6.72	7.50	6.63	5.17	3.39	6.55	7.48
C_2H_6 298 K, 1 atm	4.82	5.31	5.00	3.44	2.78	4.69	5.93
Q_{st}^0 (kJ/mol)	25.33	29.78	22.31	26.25	24.36	24.02	22.22
CO_2 273 K, 1 atm	5.64	6.32	5.58	6.15	4.87	3.96	6.80
CO_2 298 K, 1 atm	3.02	3.68	3.31	3.25	3.26	1.78	3.96
Q_{st}^0 (kJ/mol)	22.96	20.83	22.52	28.89	12.56	18.64	19.24
CH_4 273 K, 1 bar	1.56	1.71	1.25	1.35	0.62	0.55	1.77
CH_4 298 K, 1 bar	0.87	1.01	0.79	0.79	0.55	0.41	1.13

Table 2.6. Summary of published porous materials for ammonia sorption.

Material	Material Type	BET (m^2/g)	ammonia uptake (mmol/g)	Conditions	Measure Type	Ammonia Cycling Ability	ref.
CoHCC	Porous Dye	848	21.9	298 K, 1 bar	Isotherm	no loss (4 cycles)	17
CuHCF	Porous Dye	547	20.2	298 K, 1 bar	Isotherm	Not reversible	• 17
Cu_2Cl_2(BTTA)	MOF	1205	19.79	293 K, 1 bar	Isotherm	NA	11b
Co_2Cl_2(BTTA)	MOF	1161	17.95	293 K, 1 bar	Isotherm	5.6% loss (3 cycle	11b
Fe-MIL-101-	MOF	1900	17.8	298 K, 1 bar	Isotherm	NA	18
$Zn_2(L1)_2$(bipy)	MOF	47	17.79	293 K, 1 bar	Isotherm	NA	19
BPP-5	COF	700	17.7	298 K, 1 bar	Isotherm	NA	18
$Co(NA)_2$	MOF	55	17.5	298 K, 1 bar	Isotherm	no loss (3 cycles)	20
BPP-7	COF	705	16.1	298 K, 1 bar	Isotherm	NA	18
Mn_2Cl_2(BTDD)	MOF	1917	15.47	298 K, 1 bar	Isotherm	NA	21
COF-10	COF	1148	15	298 K, 1 bar	Isotherm	4.5% loss (3	22
Ni_2Cl_2(BTTA)	MOF	1193	14.68	298 K, 1 bar	Isotherm	NA	23
$Zn_2(L1)_2$(bpe)	MOF	NA	14.31	293 K, 1 bar	Isotherm	NA	17
MFM-300(Al)	MOF	1325	13.9	293 K, 1 bar	Isotherm	no loss (50 cycles)	11a
CPM-100a-FeNi	MOF-COF	1139	13.01	298 K, 1 bar	Isotherm	no loss (4 cycles)	**this work**
CPM-100b	MOF-COF	721	12.56	298 K, 1 bar	Isotherm	11.3% loss (4 cycl	**this work**
CPM-100c	MOF-COF	696	12.54	298 K, 1 bar	Isotherm	7.2% (4 cycles)	**this work**
Prussian Blue	Porous Dye	280	12.5	298 K, 1 bar	Isotherm	NA	11b
$Cu(INA)_2$	MOF	164	12.5	298 K, 1 bar	Isotherm	no loss (3 cycles)	22
$Cu(NA)_2$	MOF	164	12.5	298 K, 1 bar	Isotherm	no loss (3 cycles)	19
MOF-5	MOF	2449	12.2	298 K, 1 bar	Isotherm	NA	23
MOF-177	MOF	3275	12.2	298 K, 1 bar	Isotherm	NA	23
PPN-6-SO_3H	COF	1200	12.1	298 K, 1 bar	Isotherm	NA	18
CPM-100a-FeMg	MOF-COF	1425	12.02	298 K, 1 bar	Isotherm	5.8% loss (4 cycle	**this work**
CPM-100a-InCo	MOF-COF	1388	11.66	298 K, 1 bar	Isotherm	4.7% loss (4 cycle	**this work**
MOS-1	MOF	1112	11.5	298 K, 1 bar	Isotherm	no loss (5 cycles)	24

Table 2.7. Summary of materials for ammonia uptake.

Material	Material Type	S_A BET (m^2/g)	Pore Volume	NH_3 Capacity	NH_3 Packing density	Cycling Ability	Ref.
CoHCC	Porous Dye	848	0.79	21.9	0.471	4 cycles, no loss	16
Co_2Cl_2BBTA	MOF	1161	0.50	18.0	0.610	3 cycles, 5.6% loss	11b
COF-10	COF	1200	0.81	15.0	0.315	3 cycles, 4.5% loss	17
MFM-300(Al)	MOF	1325	0.38	13.9	0.622	50 cycles, no loss	11a
CPM-100a-FeNi	MOF-COF	1139	0.571	13.01	0.387	4 cycles, no loss	**this work**
CPM-100b	MOF-COF	721	0.357	12.56	0.598	4 cycles, 11.3% loss	**this work**
CPM-100c	MOF-COF	696	0.357	12.54	0.597	4 cycles, 7.2% loss	**this work**
CPM-100a-FeMg	MOF-COF	1425	0.733	12.02	0.279	4 cycles, 5.8% loss	**this work**
CPM-100a-InCo	MOF-COF	1388	0.556	11.66	0.357	4 cycles, 4.7% loss	**this work**
tpt-InCo-BDC	MOF	1106	0.56	11.14	0.338	4 cycles, 10.1% loss	**this work**
CPM-100d	MOF-COF	1236	0.62	7.85	0.215	4 cycles, 37.7% loss	**this work**
Amberlyst 15	Ion-exchange Resin	225	0.40	11.3	0.480	NA	25
13X zeolite	Zeolite	615	0.34	9.3	0.465	NA	25
MCM-41	Mesoporous Silica	990	1.00	7.9	0.134	NA	21

2.4 Conclusion

In summary, an integrated MOF-COF synthesis method has been developed as a new pore-space-partition strategy, leading to a novel family of **pacs** materials, named tpb-**pacs**. It differs from previous tpt-**pacs** and trz-**pacs** by combining a simultaneous formation process of both coordination bond and covalent bond, leading to **pacs** materials with exposed boron Lewis acid sites. The gas sorption study shows that the tpb-**pacs** exhibits the high-performance gas sorption properties for common gasses, and in addition shows enhanced NH_3 uptake. It also reveals a cosolvent reaction approach which will help explore **pacs** family and other crystalline porous materials. Importantly, this method represents the first step in introducing C_3-symmetric fragments in COFs (boronate ester-linkage, imine-linkage and hydrazine-linkage) into the structure. Further materials and applications based on this strategy needed to be explored.

2.5 Reference

[1] H.-C. Zhou, J. R. Long, O. M. Yaghi, *Chem. Rev*. **2012**, *112*, 673-674.

[2] a) R. E. Morris, P. S. Wheatley, *Angew. Chem. Int. Ed.* **2008**, *47*, 4966-4981; b) M. Eddaoudi, J. Kim, N. Rosi, D. Vodak, J. Wachter, M. Keeffe, O. M. Yaghi, *Science* **2002**, *295*, 469; c) J. An, N. L. Rosi, *J. Am. Chem. Soc.* **2010**, *132*, 5578-5579; d) M. I. H. Mohideen, B. Xiao, P. S. Wheatley, A. C. McKinlay, Y. Li, A. M. Z. Slawin, D. W. Aldous, N. F. Cessford, T. Düren, X. Zhao, R. Gill, K. M. Thomas, J. M. Griffin, S. E. Ashbrook, R. E. Morris, *Nat. Chem.* **2011**, *3*, 304; e) X. Yang, Q. Xu, *Crystal Growth & Design* **2017**, *17*, 1450-1455.

[3] a) X. Cui, K. Chen, H. Xing, Q. Yang, R. Krishna, Z. Bao, H. Wu, W. Zhou, X. Dong, Y. Han, B. Li, Q. Ren, M. J. Zaworotko, B. Chen, *Science* **2016**, *353*, 141; b) L. Li, R.-B. Lin, R. Krishna, H. Li, S. Xiang, H. Wu, J. Li, W. Zhou, B. Chen, *Science* **2018**, *362*, 443; c) M. S. Denny, Jr., S. M. Cohen, *Angew. Chem. Int. Ed.* **2015**, *54*, 9029-9032; d) Y. Peng, T. Gong, K. Zhang, X. Lin, Y. Liu, J. Jiang, Y. Cui, *Nat. Commun.* **2014**, *5*, 4406; e) Z. G. Gu, W. Q. Fu, X. Wu, J. Zhang, *Chem. Commun.* **2016**, *52*, 772-775; f) Y.-P. He, L.-B. Yuan, G.-H. Chen, Q.-P. Lin, F. Wang, L. Zhang, J. Zhang, *J. Am. Chem. Soc.* **2017**, *139*, 16845-16851.

[4] a) L. Jiao, Y. Wang, H.-L. Jiang, Q. Xu, *Adv. Mater*. **2018**, *30*, 1703663; b) H. Fei, S. M. Cohen, *J. Am. Chem. Soc.* **2015**, *137*, 2191-2194; c) L. Wang, D. W. Agnew, X. Yu, J. S. Figueroa, S. M. Cohen, *Angew. Chem. Int. Ed.* **2018**, *57*, 511-515; d) X.-L. Wang, L.-Z. Dong, M. Qiao, Y.-J. Tang, J. Liu, Y. Li, S.-L. Li, J.-X. Su, Y.-Q. Lan, *Angew. Chem. Int. Ed.* **2018**, *57*, 9660-9664; e) J.-S. Qin, S. Yuan, L. Zhang, B. Li, D.-Y. Du, N. Huang, W. Guan, H. F. Drake, J. Pang, Y.-Q. Lan, A. Alsalme, H.-C. Zhou, *J. Am. Chem. Soc.* **2019**, *141*, 2054-2060; f) X. Yu, S. M. Cohen, *J. Am. Chem. Soc.* **2016**, *138*, 12320-12323; g) F.-M. Zhang, J.-L. Sheng, Z.-D. Yang, X.-J. Sun, H.-L. Tang, M. Lu, H. Dong, F.-C. Shen, J. Liu, Y.-Q. Lan, *Angew. Chem. Int. Ed.* **2018**, *57*, 12106-12110; h) E.-X. Chen, M. Qiu, Y.-F. Zhang, Y.-S. Zhu, L.-Y. Liu, Y.-Y. Sun, X. Bu, J. Zhang, Q. Lin, *Adv. Mater.* **2018**, *30*, 1704388.

[5] a) Q.-G. Zhai, X. Bu, X. Zhao, D.-S. Li, P. Feng, *Acc. Chem. Res.* **2017**, *50*, 407-417; b) Q.-G. Zhai, X. Bu, C. Mao, X. Zhao, L. Daemen, Y. Cheng, A. J. Ramirez-Cuesta, P. Feng, *Nat. Commun.* **2016**, *7*, 13645.

[6] a) C. Serre, F. Millange, S. Surblé, G. Férey, *Angew. Chem. Int. Ed*. **2004**, *43*, 6285-6289; b) A. C. Sudik, A. P. Côté, O. M. Yaghi, *Inorg. Chem.* **2005**, *44*, 2998-3000.

[7] a) S.-T. Zheng, X. Zhao, S. Lau, A. Fuhr, P. Feng, X. Bu, *J. Am. Chem. Soc.* **2013**, *135*, 10270-10273; b) X. Zhao, X. Bu, E. T. Nguyen, Q.-G. Zhai, C. Mao, P. Feng,

J. Am. Chem. Soc. **2016**, *138*, 15102-15105; c) X. Zhao, X. Bu, Q.-G. Zhai, H. Tran, P. Feng, *J. Am. Chem. Soc.* **2015**, *137*, 1396-1399.

[8] Y.-S. Wei, M. Zhang, P.-Q. Liao, R.-B. Lin, T.-Y. Li, G. Shao, J.-P. Zhang, X.-M. Chen, *Nat. Commun.* **2015**, *6*, 8348.

[9] a) P. J. Waller, F. Gandara, O. M. Yaghi, *Acc. Chem. Res.* **2015**, *48*, 3053-3063; b) S.-Y. Ding, W. Wang, *Chem. Soc. Rev.* **2013**, *42*, 548-568; c) H. Wang, Z. Zeng, P. Xu, L. Li, G. Zeng, R. Xiao, Z. Tang, D. Huang, L. Tang, C. Lai, D. Jiang, Y. Liu, H. Yi, L. Qin, S. Ye, X. Ren, W. Tang, *Chem. Soc. Rev.* **2019**, *48*, 488-516.

[10] a) A. P. Côté, A. I. Benin, N. W. Ockwig, M. O'Keeffe, A. J. Matzger, O. M. Yaghi, *Science* **2005**, *310*, 1166-1170; b) A. P. Côté, H. M. El-Kaderi, H. Furukawa, J. R. Hunt, O. M. Yaghi, *J. Am. Chem. Soc.* **2007**, *129*, 12914-12915; c) H. M. El-Kaderi, J. R. Hunt, J. L. Mendoza-Cortés, A. P. Côté, R. E. Taylor, M. O'Keeffe, O. M. Yaghi, *Science* **2007**, *316*, 268-272; d) Y. Yuan, F. Sun, F. Zhang, H. Ren, M. Guo, K. Cai, X. Jing, X. Gao, G. Zhu, *Adv. Mater.* **2013**, *25*, 6619-6624; e) R. Nishiyabu, Y. Kubo, T. D. James, J. S. Fossey, *Chem. Commun.* 2011, *47*, 1124-1150; f) A. L. Korich, P. M. Iovine, *Dalton Trans*. **2010**, *39*, 1423-1431.

[11] a) F. J. Uribe-Romo, J. R. Hunt, H. Furukawa, C. Klöck, M. O'Keeffe, O. M. Yaghi, *J. Am. Chem. Soc.* **2009**, *131*, 4570-4571; b) Q. Fang, S. Gu, J. Zheng, Z. Zhuang, S. Qiu, Y. Yan, *Angew. Chem.* **2014**, *126*, 2922-2926; c) S. Kandambeth, A. Mallick, B. Lukose, M. V. Mane, T. Heine, R. Banerjee, *J. Am. Chem. Soc.* **2012**, *134*, 19524-19527; d) L. Stegbauer, K. Schwinghammer, B. V. Lotsch, *Chem. Sci.* **2014**, *5*, 2789-2793.

[12] a) P. Kuhn, M. Antonietti, A. Thomas, *Angew. Chem. Int. Ed.* **2008**, *47*, 3450-3453; b) S. Dalapati, S. Jin, J. Gao, Y. Xu, A. Nagai, D. Jiang, *J. Am. Chem. Soc.* **2013**, *135*, 17310-17313.

[13] a) T. Ben, H. Ren, S. Ma, D. Cao, J. Lan, X. Jing, W. Wang, J. Xu, F. Deng, J. M. Simmons, S. Qiu, G. Zhu, *Angew. Chem. Int. Ed.* **2009**, *48*, 9457-9460; b) Q. Fang, Z. Zhuang, S. Gu, R. B. Kaspar, J. Zheng, J. Wang, S. Qiu, Y. Yan, *Nat. Commun.* **2014**, *5*, 4503; c) K. T. Jackson, T. E. Reich, H. M. El-Kaderi, *Chem. Commun.* **2012**, *48*, 8823-8825.

[14] Q. Lin, C. Mao, A. Kong, X. Bu, X. Zhao, P. Feng, *J. Mater. Chem. A* **2017**, *5*, 21189-21195.

[15] a) C. Mellot-Draznieks, C. Serre, S. Surblé, N. Audebrand, G. Férey, *J. Am. Chem. Soc.* **2005**, *127*, 16273-16278; b) Z. Tian, S. Dai, D.-e. Jiang, *J. Phys. Chem. Lett.* **2016**, *7*, 2568-2572.

[16] a) H. G. W. Godfrey, I. da Silva, L. Briggs, J. H. Carter, C. G. Morris, M. Savage, T. L. Easun, P. Manuel, C. A. Murray, C. C. Tang, M. D. Frogley, G. Cinque, S. Yang, M. Schröder, *Angew. Chem. Int. Ed.* **2018**, *57*, 14778-14781; b) A. J. Rieth, M. Dincă, *J. Am. Chem. Soc.* **2018**, *140*, 3461-3466.

[17] Takahashi, A.; Tanaka, H.; Parajuli, D.; Nakamura, T.; Minami, K.; Sugiyama, Y.; Hakuta, Y.; Ohkoshi, S.-i.; Kawamoto, T. *J. Am. Chem. Soc.* **2016**, *138*, 6376.

[18] Van Humbeck, J. F.; McDonald, T. M.; Jing, X.; Wiers, B. M.; Zhu, G.; Long, J. R. *J. Am. Chem. Soc.* **2014**, *136*, 2432.

[19] Glomb, S.; Woschko, D.; Makhloufi, G.; Janiak, C. *ACS Appl. Mater. Interfaces* **2017**, *9*, 37419.

[20] Chen, Y.; Shan, B.; Yang, C.; Yang, J.; Li, J.; Mu, B. *J. Mater. Chem. A* **2018**, *6*, 9922.

[21] Rieth, A. J.; Tulchinsky, Y.; Dincă, M. *J. Am. Chem. Soc.* **2016**, *138*, 9401.

[22] Doonan, C. J.; Tranchemontagne, D. J.; Glover, T. G.; Hunt, J. R.; Yaghi, O. M. *Nat. Chem.* **2010**, *2*, 235.

[23] Chen, Y.; Li, L.; Li, J.; Ouyang, K.; Yang, J. J. Haz. Mat. **2016**, 306, 340.

[24] Saha, D.; Deng, S. J. *Colloid. Interf. Sci.* **2010**, *348*, 615.

[25] Chen, Y.; Wang, Y.; Yang, C.; Wang, S.; Yang, J.; Li, J. *ACS Sustainable Chem. Eng.* **2017**, *5*, 5082.

Chapter 3 Pore-Space Partition via Monomer Trimerization for Acetylene and Carbon Dioxides Separation

3.1 Introduction

The separation of acetylene from carbon dioxides is a key but energy consuming process in chemical industry.[1] The physical similarity (boiling points: 189.3 K and 194.7 K for C_2H_2 and CO_2; sizes: 3.32 × 3.34 × 5.7 $Å^3$ and 3.18 × 3.33 × 5.36 $Å^3$ for C_2H_2 and CO_2) between these two molecules demands a less energy-intensive adsorptive separation, compared with the widely utilized cryogenic distillation.[2] This work provides an efficient platform for C_2H_2/CO_2 adsorptive separations.

The ideal porous materials for gas separation benefits from uptake capacity and separation selectivity and a trade-off between both aspects poses challenges in chemical separations.[3] Despite it is hard to maximize both performance in the same material, some works have been reported to date. The peroxo-MOF-74-Fe ($Fe_2(O_2)$dobdc) possessed 74.3 cm^3/g ethane uptake and record-high C_2H_6/C_2H_4 selectivity owing to the iron-peroxo sites.[4] SIFSIX-2-Cu-i exhibited high C_2H_2/C_2H_4 selectivity of 39.7 to 44.8 and gas capacity of 780 mmol/L in 1/99 C_2H_2/C_2H_4 gas mixture.[5] The strong host-guest interaction comes from C-H···F H-bonding between C_2H_2 and SiF_6^- anions. USTA-300a was an ultra-

efficient C_2H_2 selective adsorbent (selectivity of 743 in C_2H_2/CO_2), however, the C_2H_2 capacity was ~69 cm^3/g under ambient conditions.[6]

The functional groups as shown in peroxo-MOF-74-Fe and SIFSIXs are feasible method enhancing interactions between porous materials and gas molecules. It may result in the loss of structural robustness and stability. For gas separation trials beyond bench-scale, the stability under ambient conditions and regeneration costs are of vital concerns. In this work, we report the first application of our novel monomer-trimerization pore-space partition (PSP) strategy, organic molecules self-assembly into C_3-symmetric PSP agents during MOF formations, for the C_2H_2-selective C_2H_2/CO_2 separation. The competitive aspect of this PSP approach is that it enables the C_2H_2 uptake capacity dramatically increased more than 2-fold of the non-partitioned material MIL-88 and the benchmark material USTA-300a. [7] Besides, the binding strength is only half of that of USTA-300a. We demonstrate that the C_2H_2/CO_2 separation ability can be tuned through any one of two pore-partition and framework ligands. Importantly, these materials are highly stable and are feasible in C_2H_2/CO_2 separation due to the high C_2H_2 uptakes.

The platform of materials is constructed via insertion of a pore-partitioning agent into the 1D hexagonal channel of the MIL-88/MOF-235 (**acs**) frameworks,[8] resulting in a **pacs** net (partitioned-**acs**).[9] The general formula of **pacs** materials is $[M_3(O/OH)L1_3]L2$, where M represents the metal or metal combinations in the trimer, L1 is the ligand on the parent frameworks, and L2 is the pore-partitioning agent. There are generally three types of PSP agents, including individual C_3- symmetric ligands, [9-10] in-situ formed metal-ligand clusters,[11] and self-assembly of organic monomers into C_3-symmetric ligands.[12]

Covalent-organic frameworks (COFs) are composed by organic molecules linked through covalent bonds forming crystalline porous 2D or 3D networks.[13] The combination of COF and MOF has attracted a lot attention in these years.[14]

In our previous work, we employed COF-1 chemistry by assembling pyridine-4-boronic acid to 2,4,6-tri(4-pyridinyl)-1,3,5-boroxine (tpb), a PSP agent into **pacs** materials simultaneously with MOF formation.[15] The introduction of toluene into MOF reaction solvent DMF or DMA facilitates the concurrent and synergistic reactions between MOFs and COFs. In this work, we further explore and expand this co-solvent method by mixing 1,3,5-trimethylbenzene with DMF enabling in-situ growth of MOFs with trimerization of three different monomers, including 4-cyanopyridine, 4-vinylpyridine, and pyridine-4-boronic acid into 2,4,6-tri(pyridin-4-yl)-1,3,5-triazine (TPT), 1,3,5-tri(pyridin-4-yl)-cyclohexane (TPC), and 2,4,6-tri(4-pyridinyl)-1,3,5-boroxine (TPB), respectively, functionalized as PSP ligands.

Thanks to the structural versatility (L1, L2, and metal combinations), we have evaluated the effects from the following aspects: pore-partitioning ligands – TPT, TPC, TPB; ligands on parent frameworks – BDC, TAZBC, CPT; and metal combinations Co_2V and Co_3 (Figure 3.1). While there are 18 structural analogs by combining these components, we are able to summarize general trends in separations with five combinations over here.

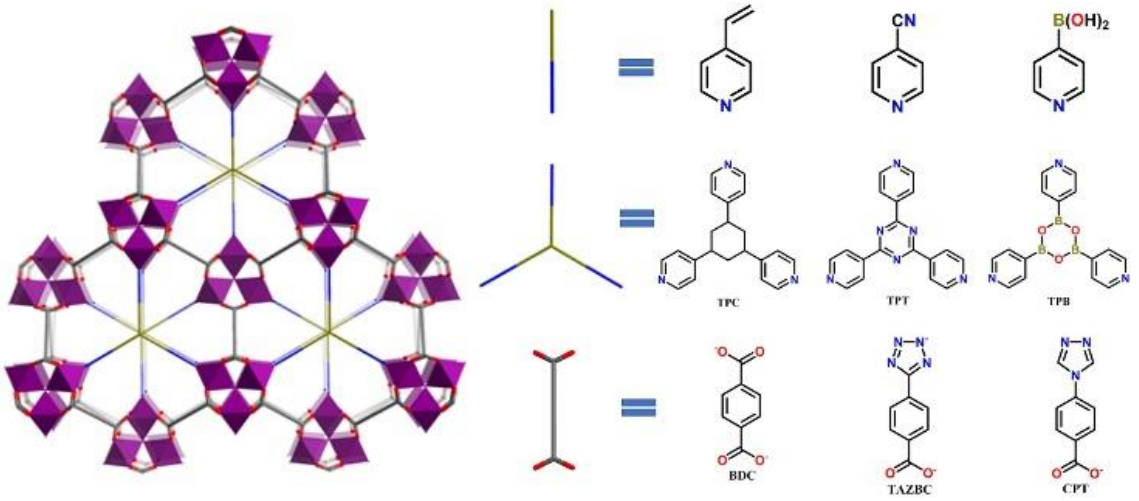

Figure 3.1 Structural illustration of **pacs** MOFs in this work. From top to bottom include three monomers (4-cyanopyridine, 4-vinylpyridine, and pyridine-4-boronic acid), three monomer-trimerized L1 ligands (TPT, TPC, and TPB), and three L2 ligands (BDC, TAZBC, and CPT).

3.2 Experimental Section

3.2.1 Chemicals and General Methods

All reagents were purchased and utilized without further purification. cobalt nitrate hexahydrate ($Co(NO_3)_2 \cdot 6H_2O$), cobalt chloride hexahydrate ($CoCl_2 \cdot 6H_2O$), vanadium (III) chloride (VCl_3), 1,4-terephthalic acid (H_2BDC), 4-(1H-tetrazol-5-yl)-benzoic acid (H_2TAZBC), 4-(4H-1,2,4-triazol-4-yl)benzoic acid (HCPT), pyridine-4-boronic acid (96%), 4-cyanopyridine (98%), 4-vinylpyridine (>95%), N, N-dimethylformamide (DMF), 1,3,5-trimethylbenzene (TMB), Ethanol (EtOH), and 1,1,1,5,5,5-hexafluoro-2,4-pentanedione (HFP).

Breakthrough Measurement.

Sample was activated using the method mentioned above. Then, the sample was pelletized (20-25 MPa) and broken in to pieces using a 45-60 standard mesh sieve. The as-prepared sample was loaded into a U-shaped glass sample holder (length: 13 cm, inner diameter: 0.45 cm) and fitted with two pieces of cotton on both sides to prevent sample from moving. The gas flow rates were controlled by 10sccm mass flow controllers purchased from MKS Co. And the outlet gas components were monitored by residual gas analysis mass spectrometer from Hiden Co. Sample was regenerated under 60 ° C with 7 ml/min He flow for 2 h.

Selectivity by IAST.

To evaluate the C2H2/CO2 separation performance, the selectivity was calculated by ideal adsorbed solution theory (IAST). Double-site Langmuir-Freundlich (DSLF) model was employed to fit the gas adsorption isotherms over the entire pressure range. DSLF model can be written as:

$$q = \mathrm{q}_{A,sat}\frac{P^{nA}b_A}{1+P^{nA}b_A} + \mathrm{q}_{B,sat}\frac{P^{nB}b_B}{1+P^{nB}b_B} \qquad (1)$$

where q is the amount adsorbed in mmol/g, q_{sat} is the amount adsorbed when saturated with gas in mmol/g, b is the Langmuir parameter in bar-1, P is the pressure in bar, n is the dimensionless Freundlich parameter. The Langmuir parameters for each site is temperature-dependent:

$$b_A = b_{A0}\,exp\left(\frac{E_A}{RT}\right) \;;\; b_B = b_{B0}\,exp\left(\frac{E_B}{RT}\right) \qquad (2)$$

The adsorption selectivity is defined as:

$$selectivity = \frac{x_{C_2H_2}/x_{CO_2}}{y_{C_2H_2}/y_{CO_2}} \quad (3)$$

where x is the mole fraction in the adsorbed phase, and y is the mole fraction in the gas phase.

Separation Potential.

The separation potential (ΔQ) is a combined metric, which considering both uptake capacity and selectivity. It is defined to quantify mixture separations in fixed bed adsorbers. For a C_2H_2/CO_2 mixture with mole fractions y_{C2H2}, and y_{CO2}=1-y_{C2H2}, the gravimetric separation potential ΔQ, is calculated from IAST using the formula:

$$\Delta Q = q_{C2H2}\frac{y_{CO2}}{1-y_{CO2}} - q_{CO2} \quad (4)$$

where q_{C2H2} and q_{CO2} are C_2H_2 and CO_2 uptake in the mixture, respectively, which are calculated based on IAST theory.

Thermal Stability.

Samples were heated on TGA with rates of 10 ° C/min to reach the set temperature under N_2 flow. Samples were kept at the set temperature for 1h and analyzed by PXRD patterns.

General characterization.

Other characterization such as PXRD, SCXRD, EDS, SEM, TGA, gas adsorptions were followed the same procedures in 2.2.2.

3.2.2 Synthesis Methods

Synthesis of [$Co_2V(OH)(BDC)_3TPT$] (Co_2V-BDC-TPT or CPM-733-TPT).

In a 11 mL glass vial, 60 mg of $Co(NO_3)_2 \cdot 6H_2O$, (~0.2 mmol), 17 mg VCl_3 (~0.1 mmol), 50 mg H_2BDC (~0.3 mmol), and 90 mg 4-cyanopyridine (~0.9 mmol) were dissolved in solvent mixture of 4.5 ml dimethylformamide (DMF), 0.25 ml 1,3,5-trimethylbenzene (TMB), and 28 µl 1,1,1,5,5,5-hexafluoro-2,4-pentanedione (HFP). After being stirred for an hour, the vial was placed in a 120 ℃ oven for 3 days, and the mixture was then cooled to room temperature. Dark-red spindle-shaped microcrystals were obtained. The phase purity was supported by powder X-ray diffraction.

Synthesis of [$Co_2V(OH)(BDC)_3TPC$] (Co_2V-BDC-TPC or CPM-733-TPC).

In a 11 mL glass vial, 60 mg of $Co(NO_3)_2 \cdot 6H_2O$, (~0.2 mmol), 17 mg VCl_3 (~0.1 mmol), 50 mg H_2BDC (~0.3 mmol), and 224 µl 4-vinylpyridine (excessive amount) were dissolved in solvent mixture of 3 ml dimethylformamide (DMF), 0.75 ml 1,3,5-trimethylbenzene (TMB). After being stirred for an hour, the vial was placed in a 120 ℃ oven for 3 days, and the mixture was then cooled to room temperature. Dark-red spindle-shaped microcrystals were obtained. The phase purity was supported by powder X-ray diffraction.

Synthesis of [$Co_2V(OH)(BDC)_3TPB$] (Co_2V-BDC-TPB or CPM-100a).

In a 11 mL glass vial, 120 mg of $Co(NO_3)_2 \cdot 6H_2O$, (~0.4 mmol), 34 mg VCl_3 (~0.2 mmol), 100 mg H_2BDC (~0.6 mmol), and 72 mg pyridine-4-boronic acid (~0.6 mmol) were dissolved in solvent mixture of 3 ml dimethylformamide (DMF), 0.5 ml 1,3,5-

trimethylbenzene (TMB). After being stirred for an hour, the vial was placed in a 120 ℃ oven for 3 days, and the mixture was then cooled to room temperature. Dark-red spindle-shaped microcrystals were obtained. The phase purity was supported by powder X-ray diffraction.

Synthesis of [$Co_2V(OH)(TAZBC)_3TPB$] (Co_2V-TAZBC-TPB or CPM-100e).

In a 11 mL glass vial, 120 mg of $Co(NO_3)_2 \cdot 6H_2O$, (~0.4 mmol), 34 mg VCl_3 (~0.2 mmol), 116 mg H_2TAZBC (~0.6 mmol), and 72 mg pyridine-4-boronic acid (~0.6 mmol) were dissolved in solvent mixture of 3 ml dimethylformamide (DMF), 0.25 ml 1,3,5-trimethylbenzene (TMB). After being stirred for an hour, the vial was placed in a 120 ℃ oven for 3 days, and the mixture was then cooled to room temperature. Orange spindle-shaped microcrystals were obtained. The phase purity was supported by powder X-ray diffraction.

Synthesis of [$Co_3(OH)(CPT)_3Cl_2TPB$] (Co_2V-CPT-TPB or CPM-100f).

In a 11 mL glass vial, 72 mg of $CoCl_2 \cdot 6H_2O$), (~0.3 mmol), 30 mg HCPT (~0.15 mmol), and 36 mg pyridine-4-boronic acid (~0.3 mmol) were dissolved in solvent mixture of 3 ml dimethylformamide (DMF), 0.3 ml 1,3,5-trimethylbenzene (TMB), and 28 μl 1,1,1,5,5,5-hexafluoro-2,4-pentanedione (HFP). After being stirred for an hour, the vial was placed in a 100 ℃ oven for 3 days, and the mixture was then cooled to room temperature. Pink spindle-shaped single crystals were obtained in the dark-red solution. The phase purity was supported by powder X-ray diffraction. The same cationic framework could also be prepared by using 90 mg of $Co(NO_3)_2 \cdot 6H_2O$ as cobalt salt.

3.3 Results and Discussion

3.3.1 Structure Analysis

Co-CPT-TPB was analyzed by single-crystal X-ray diffraction and refined by OLEX2 (Table 3.1). Phase purity was confirmed by comparing PXRD patterns with the simulated pattern from the refined structure file. The other structures in this work were confirmed by The PXRD patterns and simulated date from CCDC database. PXRD of Co2V-BDC-TPB was compared with the simulated result from CCDC 1894561 (CPM-100a-InCo, $In_{1.8}Co_{1.2}(OH)_{0.2}O_{0.8}(BDC)_3TPB$). The PXRD of Co_2V-BDC-TPT was compared with the simulated result from CCDC 1053416 (CPM-33a, $Ni_3(OH)(BDC)_3TPT$). The PXRD of Co_2V-BDC-TPC was compared with the simulated result from CCDC 1415806 [$Fe_3O(BDC)_3TPC)Cl$]. The PXRD of Co_2V-TAZBC-TPB was compared with the simulated result from CCDC 2043330 (SNNU-27-Co, $Co_3OH(TAZBC)_3TPPY$). All of PXRD patterns are shown in Figure 3.2.

The heterometallic compositions in metal trimers was confirmed by EDS analysis (Figure. 3.3). The metal ratios between Co and V in all four heterometallic compounds were 2 to 1 in atomic percentages. The materials in this work are highly stable. TGA analysis of all five compounds were conducted under N_2 flow (Figure 3.6). The thermal stability can reach up to 450 ° C and 350 ° C for Co_2V-BDC-TPT and Co_2V-BDC-TPC, respectively (Figure. 3.4). All of five materials maintained their crystallinity after cycled gas adsorption-desorption tests (Figure. 3.2). As illustrated in Figure. 3.5, Co_2V-BDC-TPT

and Co_2V-BDC-TPC are hydrothermally stable and could retain their structural integrity after immersing in water for 24 h.

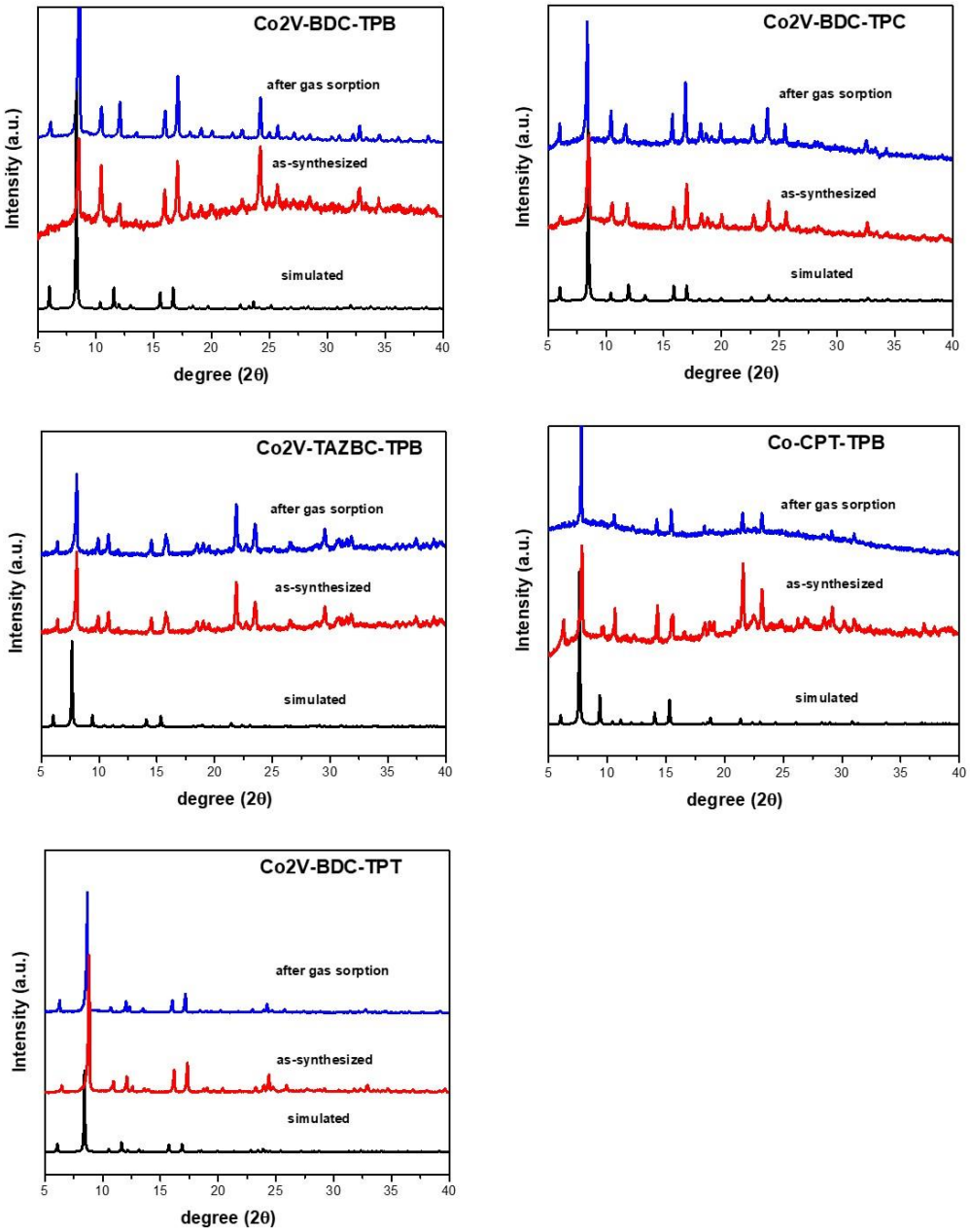

Figure 3.2 PXRD patterns of Co_2V-BDC-TPB, Co_2V-BDC-TPC, Co_2V-BDC-TPT, Co_2V-TAZBC-TPB, and Co-CPT-TPB before and after gas adsorption.

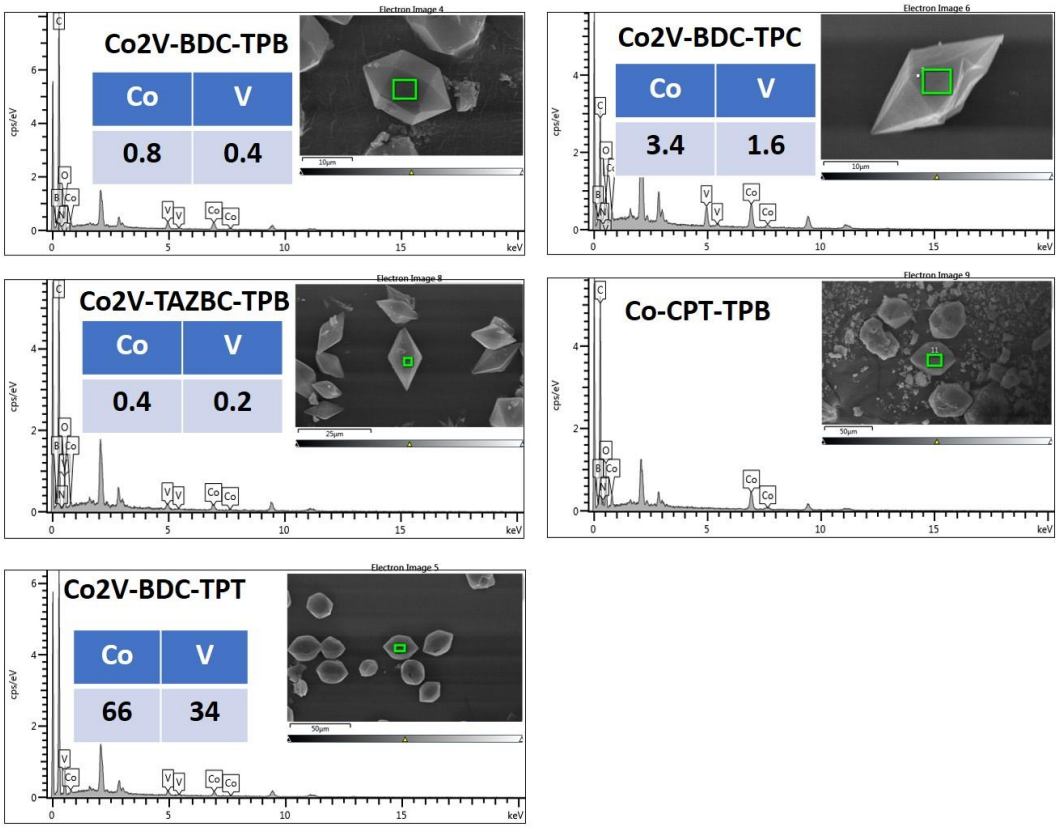

Figure 3.3 EDS and SEM results of Co_2V-BDC-TPB, Co_2V-BDC-TPC, Co_2V-BDC-TPT, Co_2V-TAZBC-TPB, and Co-CPT-TPB in this work. Atomic ratios between Co and V are listed in the form.

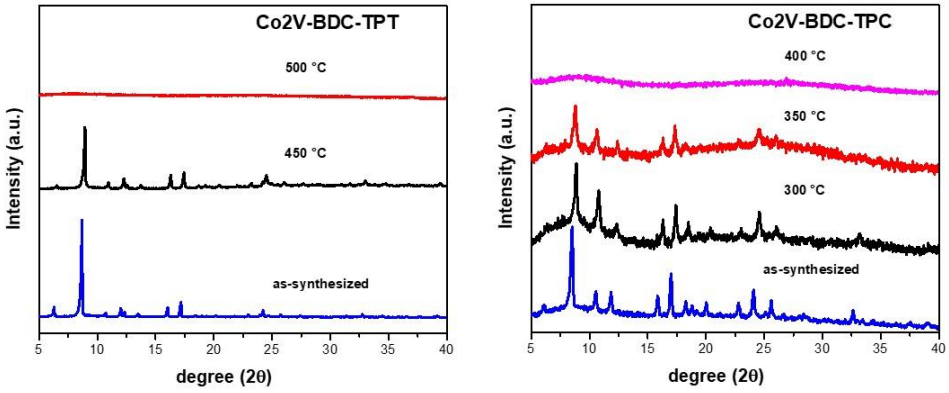

Figure 3.4 PXRD patterns of Co_2V-BDC-TPT and Co_2V-BDC-TPC after different thermal treatments.

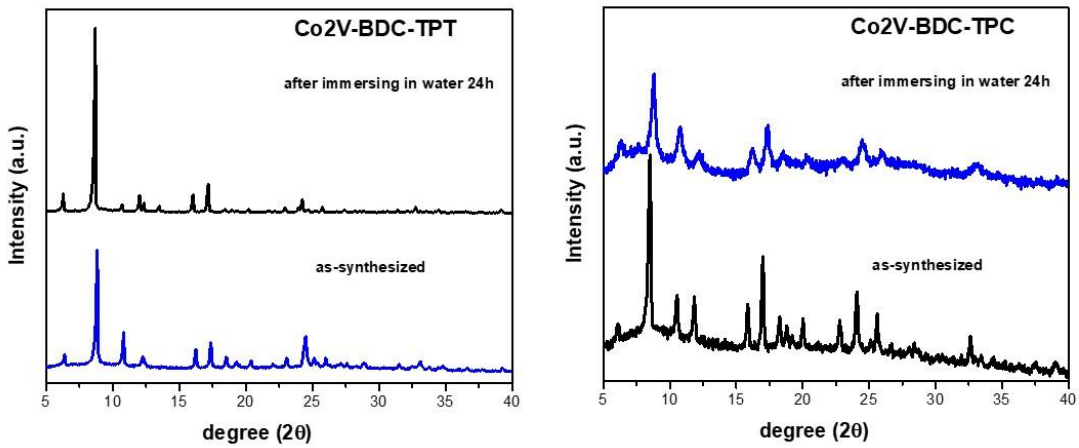

Figure 3.5 PXRD patterns of Co_2V-BDC-TPT and Co_2V-BDC-TPC after immersing in water for 24 h.

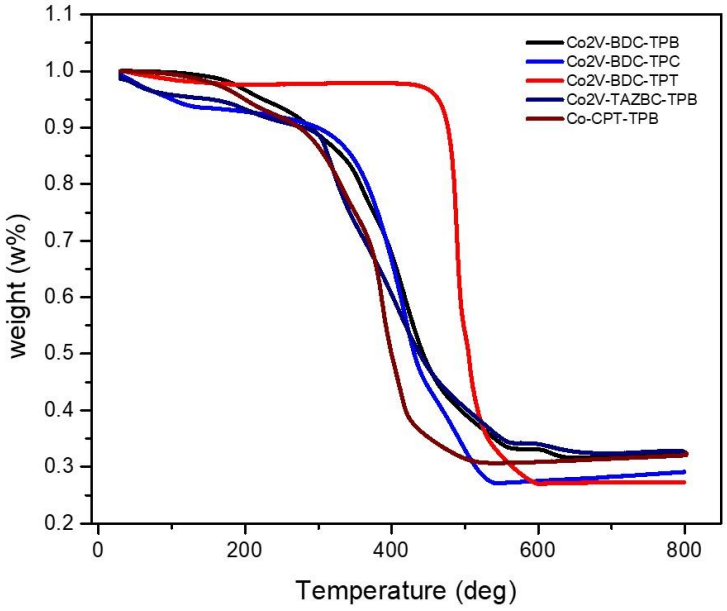

Figure 3.6 TGA of Co_2V-BDC-TPB, Co_2V-BDC-TPC, Co_2V-BDC-TPT, Co_2V-TAZBC-TPB, and Co-CPT-TPB in this work.

Table 3.1 Crystal data and structure refinement for CPM-100f (Co-CPT-TPB).

Identification code	CPM-100f	
Empirical formula	C42 H24 B3 Co3 N12 O10	
Formula weight	1065.95	
Temperature	293.15 K	
Wavelength	0.71073 Å	
Crystal system	Hexagonal	
Space group	$P6_3/m$	
Unit cell dimensions	a = 16.928(16) Å	a= 90°.
	b = 16.928 Å	b= 90°.
	c = 18.87(2) Å	g = 120°.
Volume	4683(10) $Å^3$	
Z	1	
Density (calculated)	0.378 Mg/m^3	
Absorption coefficient	0.280 mm^{-1}	
F(000)	536	
Theta range for data collection	1.389 to 14.240°.	
Index ranges	-11<=h<=11, -11<=k<=11, -13<=l<=13	
Reflections collected	10631	
Independent reflections	576 [R(int) = 0.2086]	
Completeness to theta = 14.240°	99.3 %	
Absorption correction	Semi-empirical from equivalents	
Max. and min. transmission	0.7438 and 0.5266	
Refinement method	Full-matrix least-squares on F^2	
Data / restraints / parameters	576 / 128 / 151	
Goodness-of-fit on F^2	1.856	
Final R indices [I>2sigma(I)]	R1 = 0.1466, wR2 = 0.3796	
R indices (all data)	R1 = 0.1664, wR2 = 0.3933	
Extinction coefficient	0.043(15)	
Largest diff. peak and hole	0.675 and -0.383 $e.Å^{-3}$	

3.3.2 Isotherm Gas Sorption Studies

The pore-partitioning agents quenched all open-metal sites (OMS) and generated metal-carboxylate active sites enhancing host-guest interactions in frameworks. All materials in this work present acetylene-selective C_2H_2/CO_2 separation according to the individual-gas isotherm adsorptions (Figure. 3.8-3.12). The acetylene uptakes of these materials are remarkably high. Three of five MOFs have the gas capacity from 107.9 to 184.1 cm^3/g at 298 K and 1 atm (Figure. 3.8-3.12, Table 3.2), all of which exceed 69 cm^3/g for USTA-300a,[6] a benchmark material for C_2H_2/CO_2 selectivity among acetylene-selective MOFs. Particularly, acetylene uptake by Co_2V-BDC-TPT is 184.1 cm^3/g (8.21 mmol/g), which is comparable to the capacity of benchmark materials (Table 3.3) such as SIFSIX-1-Cu (190.4 cm^3/g),[5] FJU-90a (180 cm^3/g), [10b] and SNNU-27-Fe (182.4 cm^3/g). [10a]

The adsorption enthalpies (Q_{st}) range 24.3-27.2 kJ/mol and 19.1-22.8 kJ/mol at zero coverage for C_2H_2 and CO_2 in this work (Figure. 3.7). The Q_{st} values of C_2H_2 is much lower than most MOFs, such as USTA-300a (57.6 kJ/mol) and MOF-74-Fe (74.5 kJ/mol). [6, 16] This could be advantageous for adsorbent regeneration owing to the lower energy cost.

The IAST selectivity has been employed to compare the separation potentials (Figure. 3.13). The best one is 4.5 for Co_3-BDC-TPB, which is comparable to FJU-90a (4.3), SNNU-45 (4.5),[17] CPM-107 (5.7),[18] and USTA-74a (9),[19] but significantly lower than USTA-300a (743),[6] NKMOF-1-Ni (30),[20] and FeNi-M'MOF (24) (Table 3.3).[21]

As well as uptakes and selectivity, separation potential, which is influenced by both factors, is utilized to estimate the separation performance. It illustrates the maximum amount of C_2H_2 captured from the mixture in a fixed bed adsorber, and is calculated from the equation 3 using IAST in the 3.2.2. The parameters for DSLF calculation are listed in the Table 3.5.

In addition to the as-mentioned three factors, the laboratory-scale fixed-bed gas breakthrough experiment, which is a straightforward method, is used to evaluate the gas separation performance. Breakthrough experiment, together with separation potentials, uptake capacity, and selectivity are discussed in the following when we tune the structural module to boost the C_2H_2/CO_2 separation performance.

As shown in Figure 3.13 and Table 3.2, the TPT pore space partitioning ligand was determined to have the best separation potential and uptake capacity. However, the selectivity of 2.93 for Co_2V-BDC-TPT is lower than that of 3.20 for Co_2V-BDC-TPB. This is because the π-π interaction between the triazine ring on TPT with π-electron-contained gas molecules, both acetylene and carbon dioxides. The O sites on boroxine ring provides potential interaction sites with acetylene due to H···O interaction. This can be proved via the increase of adsorption enthalpies from 25 kJ/mol for Co_2V-BDC-TPT to 26.33 kJ/mol for Co_2V-BDC-TPB, 27.0 kJ/mol for Co_2V-TAZBC-TPB, and 27.2 kJ/mol for Co-CPT-TPB in C_2H_2 adsorption, and the decrease from 20 kJ/mol for Co_2V-BDC-TPT to 19.4 kJ/mol for Co_2V-TAZBC-TPB and to 19.1 kJ/mol for Co-CPT-TPB in CO_2 adsorption (Table 3.2, Figure 3.7). The change of PSP ligand didn't lead to a significant change of BET surface areas among three versions of materials (Figure 3.14, Table 3.2). Following

the same trend, the C_2H_2 uptakes decreased from 184.1 for Co_2V-BDC-TPT to 107.7 for Co_2V-BDC-TPC and to 132.1 cm^3/g for Co_2V-BDC-TPB.

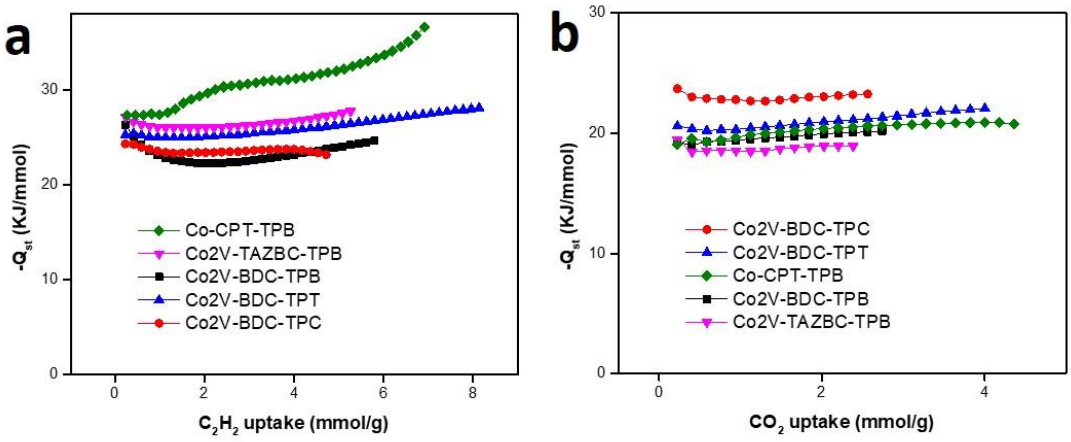

Figure 3.7 Isosteric heat of adsorption for Co_2V-BDC-TPB, Co_2V-BDC-TPC, Co_2V-BDC-TPT, Co_2V-TAZBC-TPB, and Co-CPT-TPB of a: C_2H_2 and b: CO_2.

In addition to the PSP ligand (L2 ligand) that exhibits a significant impact on C_2H_2/CO_2 selectivity, the ligands on the frameworks (L1 ligand) possesses a high impact on C_2H_2/CO_2 selectivity and C_2H_2 uptake capacity. According to the previous work, the host-guest interaction was between metal-carboxylate sites and carbon dioxides. The replacement of carboxylate groups on BDC to triazole group on CPT or tetrazole group on TAZBC was employed to reduce the framework-carbon dioxides interaction and to enhance the selectivity, which was increased from 3.20 for Co_2V-BDC-TPB to 3.99 for Co_2V-TAZBC-TPB and to 4.53 for Co_3-CPT-TPB. This is further confirmed by the decrease of the isosteric heat of adsorption in CO_2 at zero coverage that Co_2V-BDC-TPB (22.2 kJ/mol) > Co_2V-TAZBC-TPB (19.4 kJ/mol) > Co-CPT-TPB (19.1 kJ/mol) in Figure

3.7b and Table 3.2. And the increase of the isosteric heat of adsorption at zero coverage in C_2H_2 that Co-CPT-TPB (27.2 kJ/mol) > Co_2V-TAZBC-TPB (27.0 kJ/mol) > Co_2V-BDC-TPB (26.33 kJ/mol) in Figure 3.7a and Table 3.2.

The acetylene uptake capacities were following the same order of Co_2V-TAZBC-TPB (172.3) > Co-CPT-TPB (169.4) > Co_2V-BDC-TPB (107.7). It is worth to mention that CPT is -1 charged ligand different from BDC and TAZBC, which are -2 charged ligands. The Co_2V combination was employed in other versions due to the high stability as-mentioned before. In Co-CPT-TPB, Co was utilized because of the high uptake capacity, selectivity, and the reduce of counter ions Cl^-, balancing the cationic frameworks $[Co_3(OH)CPT_3]^{2+}$, in the channel.

Separation potentials were calculated via IAST as shown in Figure 3.13b. The separation potentials illustrate the predicted C_2H_2 recovered amount from C_2H_2/ CO_2 mixtures. The results follow the order of for Co-CPT-TPB (4.43) > for Co_2V-BDC-TPT (3.27) > Co_2V-TAZBC-TPB (3.26) > Co_2V-BDC-TPB (2.44) > Co_2V-BDC-TPC (1.88). It is worth to notice the separation potential of Co-CPT-TPB (4.43) is comparable to the best material FJU-90a (4.53) in C_2H_2/ CO_2 separation (Figure 3.13c). [10b]

Table 3.2. Summary of gas adsorption properties for MOFs in this work.

MOFs	S_{BET} (m^2/g)	C_2H_2 298 K, 1bar (cm^3/g)	CO_2 298 K, 1bar (cm^3/g)	C_2H_2/CO_2 selectivity	Qst (C_2H_2) (kJ/mol)	Qst (CO_2) (kJ/mol)	C_2H_2 273 K, 1bar (cm^3/g)	CO_2 273 K, 1bar (cm^3/g)
CPM-100a Co_2V-BDC-TPB	909.8	132	63.5	3.2	26.3	22.2	175.7	104.2
CPM-733-TPT Co_2V-BDC-TPT	1050.0	184.1	89.2	2.93	25.2	20.5	239.5	163.9
CPM-733-TPC Co_2V-BDC-TPC	767.7	107.9	57.2	2.87	24.3	22.8	135.4	99.0
CPM-100e Co_2V-TAZBC-	1284.6	172.3	53.0	3.99	27.0	19.4	279.3	106.8
CPM-100f Co-CPT-TPB	1251.6	169.4	101.0	4.53	27.2	19.1	248.9	177.5

Table 3.3. Summary of BET surface areas, gas adsorption uptakes at 298 K and 1 bar, adsorption enthalpies at zero-loading for MOFs with C_2H_2/CO_2 separation properties, and IAST selectivity (C_2H_2/CO_2 50/50) at 298 K and 1 bar.

MOFs	S_{BET} (m^2/g)	C_2H_2 uptake (cm3/g)	CO_2 uptake (cm3/g)	Q_{st} (C_2H_2) (kJ/mol)	Q_{st} (CO_2) (kJ/mol)	Selectivity	Ref.
FJU-90a	1572	180	103	25.1	20.7	4.3	1
CPM-733-TPT Co_2V-BDC-TPT	1050.0	184.1	89.2	25.2	20.5	2.93	this work
CPM-100e Co_2V-TAZBC-TPB	1284.6	172.3	53.0	27.0	19.4	3.99	this work
CPM-100f Co-CPT-TPB	1251.6	169.4	101.0	27.2	19.1	4.53	this work
UPC-200(Al)-F-BIM	2212	144.5	55.5	20.5	14.2	3.15	2
SNNU-45	1007	134	97.4	40	27.1	4.5	3
FJU-6-TATB	1306	110	58	29	26	3.1	4
UTSA-74a	830	107	71	31	25	9	5
CPM-107	319	97	35	37	24	5.7	6
FeNi-M'MOF	383	96	60.9	27	24.5	24	7
ZJU-74	694	85.7	69	44.5	30	36.5	8
BSF-3-Co	458	80.4	47	42.7	22.4	16.3	9
UTSA-300a	311	68.9	3.25	57.6	N.A.	743	10
NKMOF-1-Ni	382	61	51.1	60.3	40.9	30	11

Table 3.4. Summary of the refine parameters with Dual-Site Langmuir-Freundlich fitting for the single component adsorption isotherm s of C_2H_2 and CO_2 at 298 K.

MOFs	Gases	$q_{A,sat}$ (mmol/g)	b_A (kPa-1)	n_A	$q_{B,sat}$ (mmol/g)	b_B (kPa-1)	n_B	R_2
CPM-100a	C_2H_2	1.970309	0.060964	0.970346	7.018573	0.001301	1.529066	0.99999
Co_2V-BDC-TPB	CO_2	7.387753	0.000947	1.364529	0.361702	0.058257	1.064733	0.99999
CPM-733-TPT	C_2H_2	6.185408	0.020282	0.990224	5.781806	0.000422	1.878547	0.99999
Co_2V-BDC-TPT	CO_2	2.166886	0.016481	0.937842	10.67362	3.73E-04	1.4828	0.99999
CPM-733-TPC	C_2H_2	7.412904	0.00429	1.238406	0.696278	0.136725	0.867784	0.99999
Co_2V-BDC-TPC	CO_2	5.694705	0.000734	1.396357	1.162415	0.025922	0.921554	0.99999
CPM-100e	C_2H_2	9.231042	0.011016	0.994099	5.186348	7.85E-05	2.09637	0.99999
Co_2V-TAZBC-	CO_2	31.43948	0.000525	1.088897	0.030527	0.000465	3.666316	0.99998
CPM-100f	C_2H_2	2.734523	0.331199	0.925606	6.648361	4.39E-03	1.40692	0.99999
Co-CPT-TPB	CO_2	55.07501	0.001154	0.927165	0.289518	8.51E-02	1.021966	0.99999

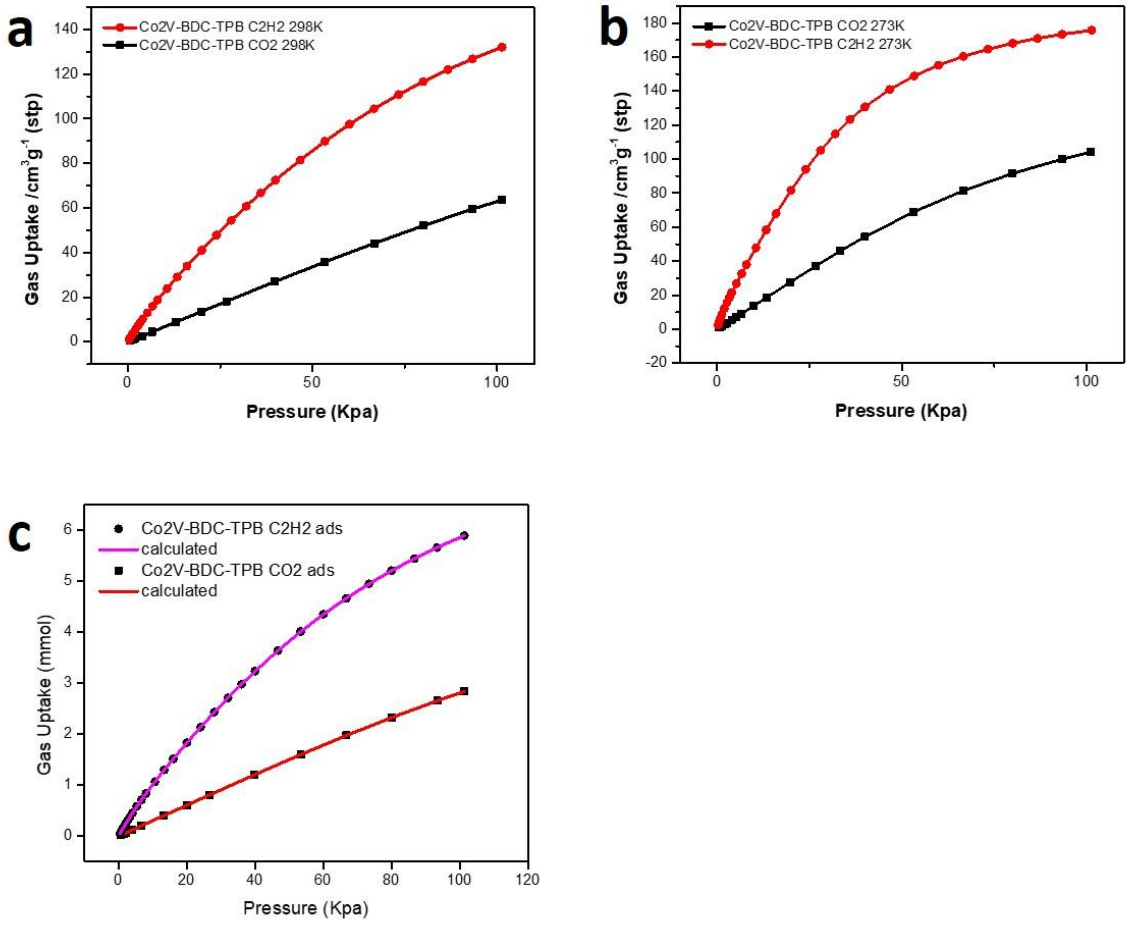

Figure 3.8 Gas adsorption properties for Co_2V-BDC-TPB. a: C_2H_2 adsorption and CO_2 adsorption at 298 K; b: C_2H_2 adsorption and CO_2 adsorption at 273 K; c: DSLF fitting for C_2H_2 adsorption and CO_2 adsorption at 298 K.

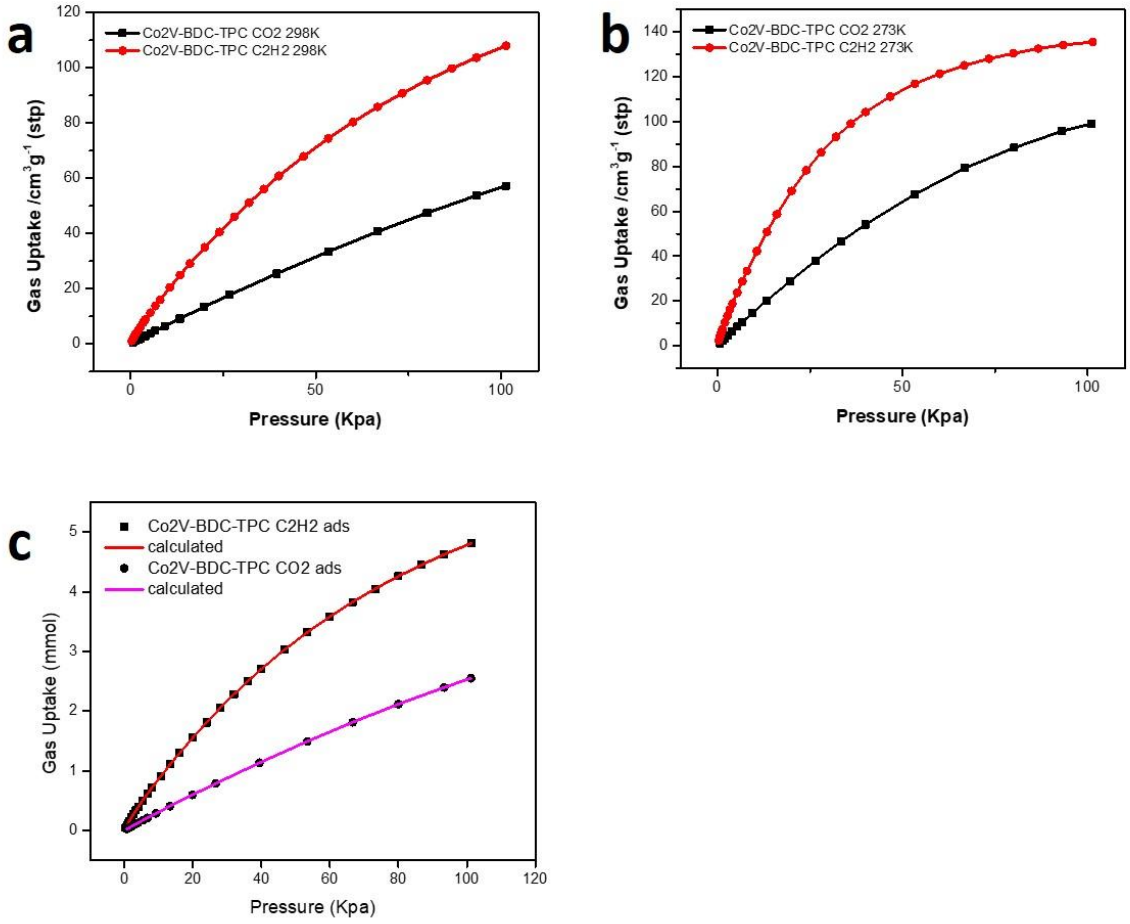

Figure 3.9 Gas adsorption properties for Co_2V-BDC-TPC. a: C_2H_2 adsorption and CO_2 adsorption at 298 K; b: C_2H_2 adsorption and CO_2 adsorption at 273 K; c: DSLF fitting for C_2H_2 adsorption and CO_2 adsorption at 298 K.

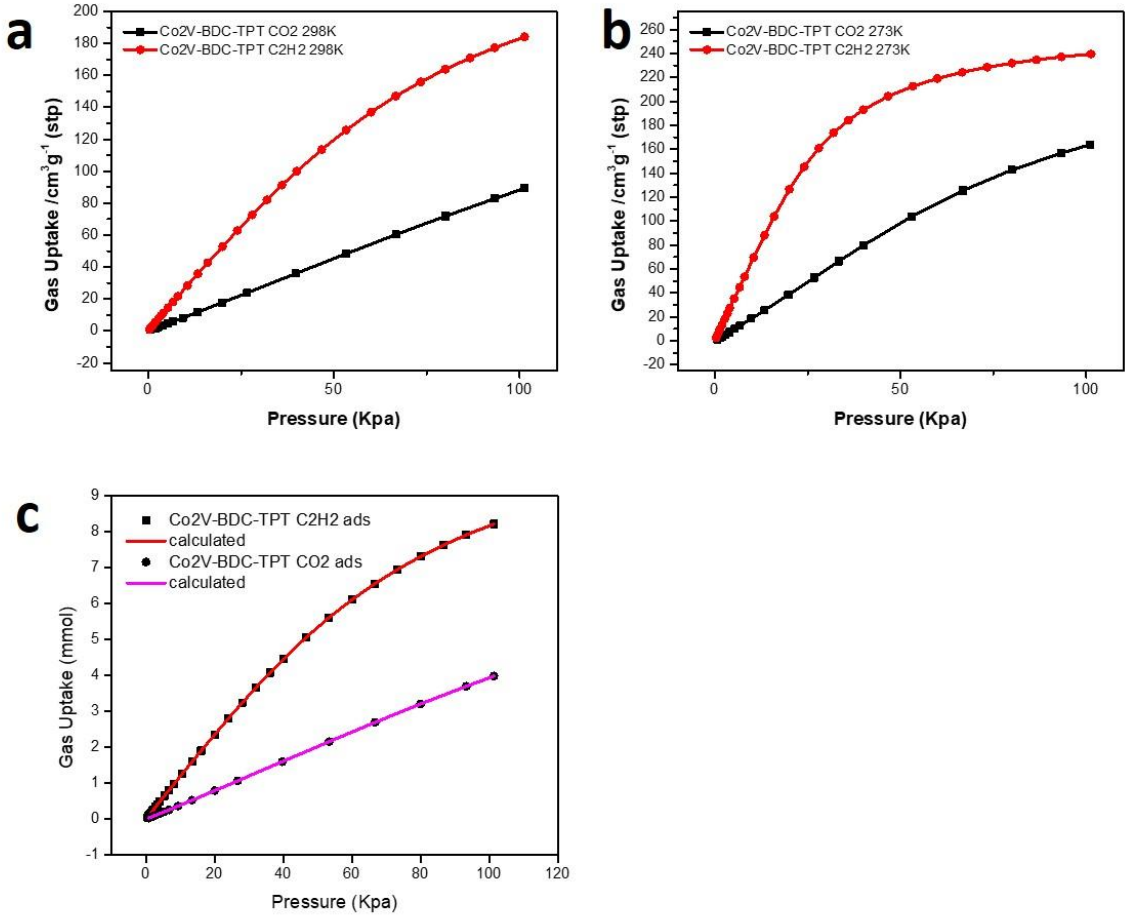

Figure 3.10 Gas adsorption properties for Co_2V-BDC-TPT. a: C_2H_2 adsorption and CO_2 adsorption at 298 K; b: C_2H_2 adsorption and CO_2 adsorption at 273 K; c: DSLF fitting for C_2H_2 adsorption and CO_2 adsorption at 298 K.

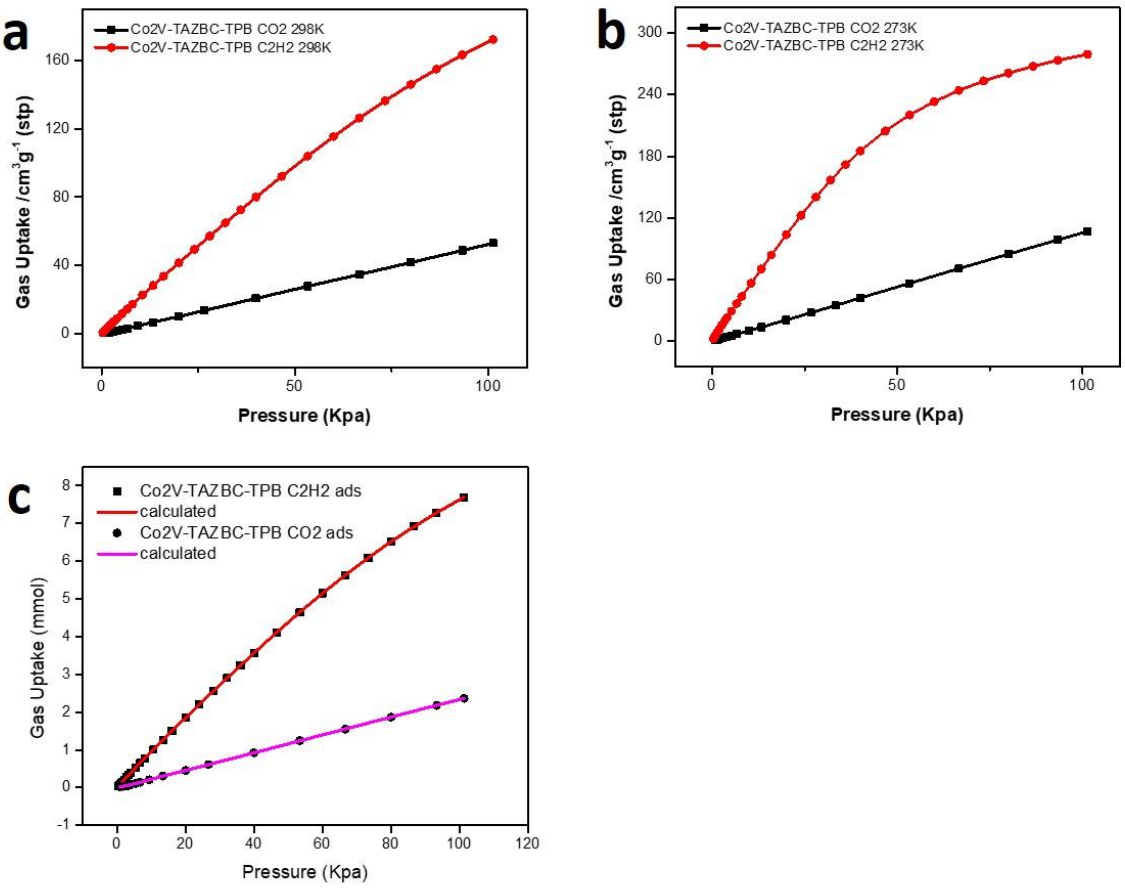

Figure 3.11 Gas adsorption properties for Co_2V-TAZBC-TPB. a: C_2H_2 adsorption and CO_2 adsorption at 298 K; b: C_2H_2 adsorption and CO_2 adsorption at 273 K; c: DSLF fitting for C_2H_2 adsorption and CO_2 adsorption at 298 K.

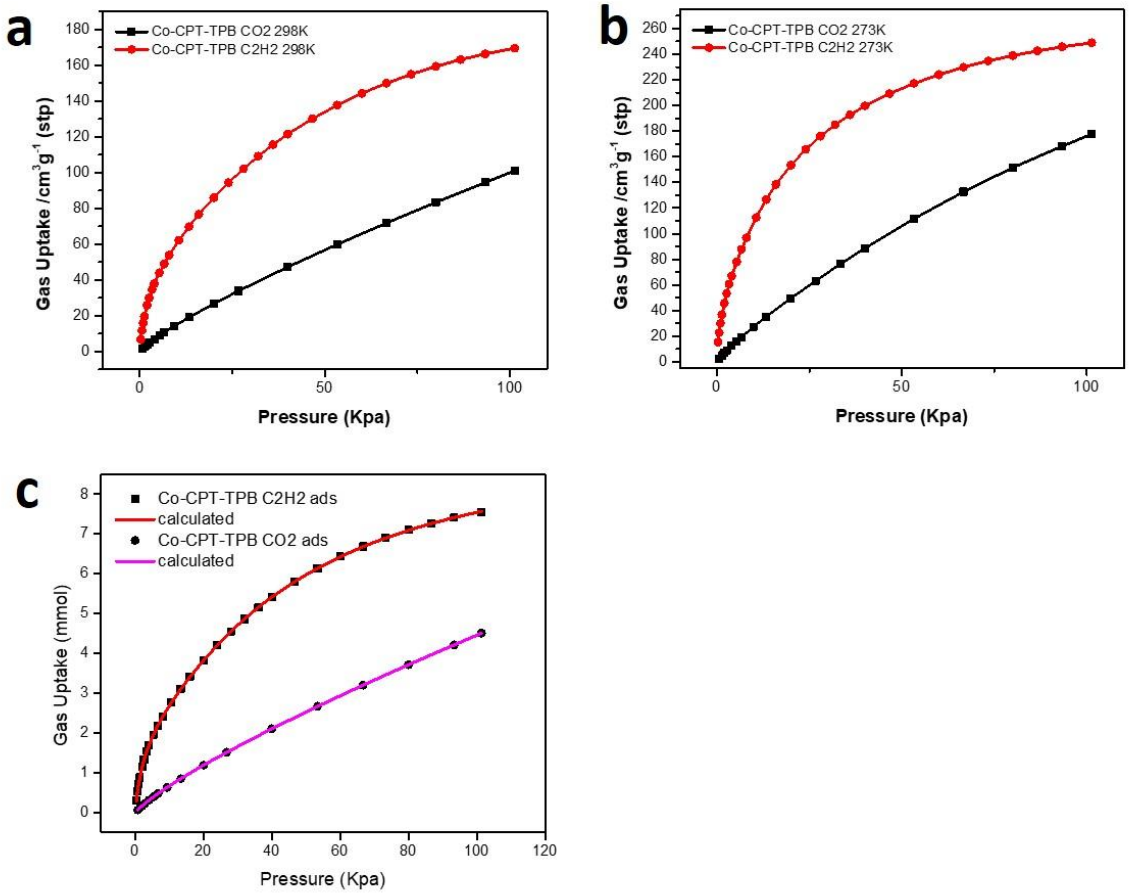

Figure 3.12 Gas adsorption properties for Co-CPT-TPB. a: C_2H_2 adsorption and CO_2 adsorption at 298 K; b: C_2H_2 adsorption and CO_2 adsorption at 273 K; c: DSLF fitting for C_2H_2 adsorption and CO_2 adsorption at 298 K.

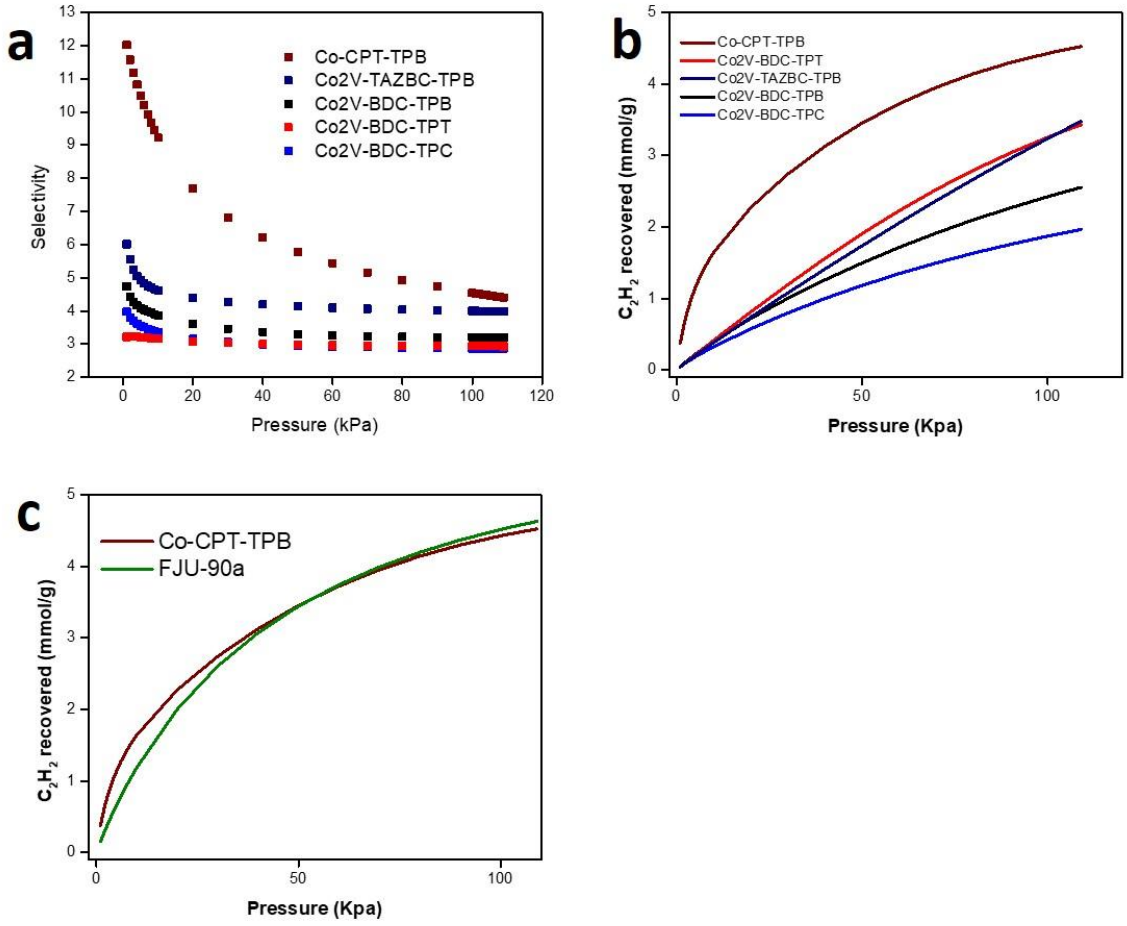

Figure 3.13 a: Comparison of IAST selectivity for C_2H_2/CO_2 (50/50) at 298 K. b: Separation potentials calculated from IAST for Co_2V-BDC-TPB, Co_2V-BDC-TPC, Co_2V-BDC-TPT, Co_2V-TAZBC-TPB, and Co-CPT-TPB in this work. c: comparison between Co-CPT-TPB and FJU-90a.

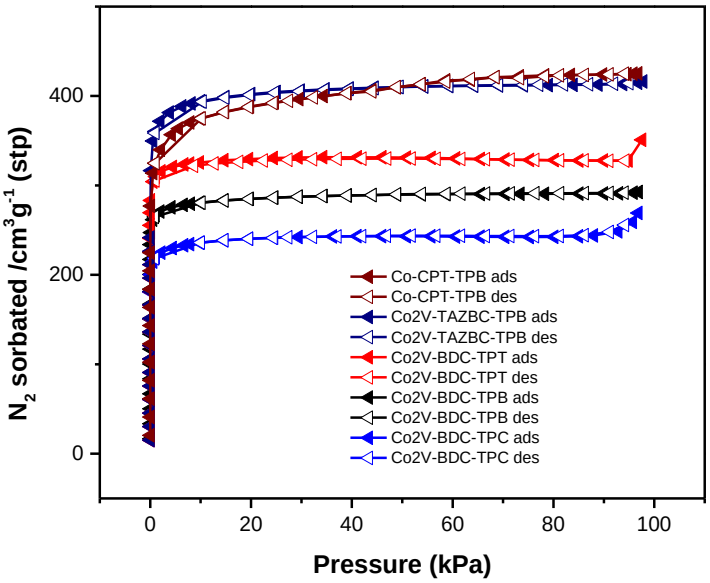

Figure 3.14 N_2 sorption isotherm at 77 K for Co_2V-BDC-TPB, Co_2V-BDC-TPC, Co_2V-BDC-TPT, Co_2V-TAZBC-TPB, and Co-CPT-TPB.

3.3.3 Transient Breakthrough Experiment

To further prove the excellent separation performance, laboratory-scaled fixed-bed transient breakthrough experiments were conducted utilizing five different materials in this work. C_2H_2/CO_2 (50/50) mixture, which flowed through packed columns at 1/1 sccm (standard cubic centimeter per minute) flow rate was selected to simulate the industrial separation process under ambient conditions (Figure 3.15, 3.16). The results explicitly present that all five materials are capable of separating gas mixtures. Among all materials, Co-CPT-TPB achieved the most efficient separation of C_2H_2/CO_2 mixture. In Figure 3.16a, CO_2 was first eluted and quickly reached a pure grade without C_2H_2 detected. C_2H_2 was trapped in the packed column for a while and then breakthrough occurred after 120 min.

To further validate the practical industrial separation ability, the recyclability test on Co-CPT-TPB was carried out. As shown in Figure 3.16b, there is no change in the retention time and C_2H_2 uptake capacity after five cycles under same operation conditions.

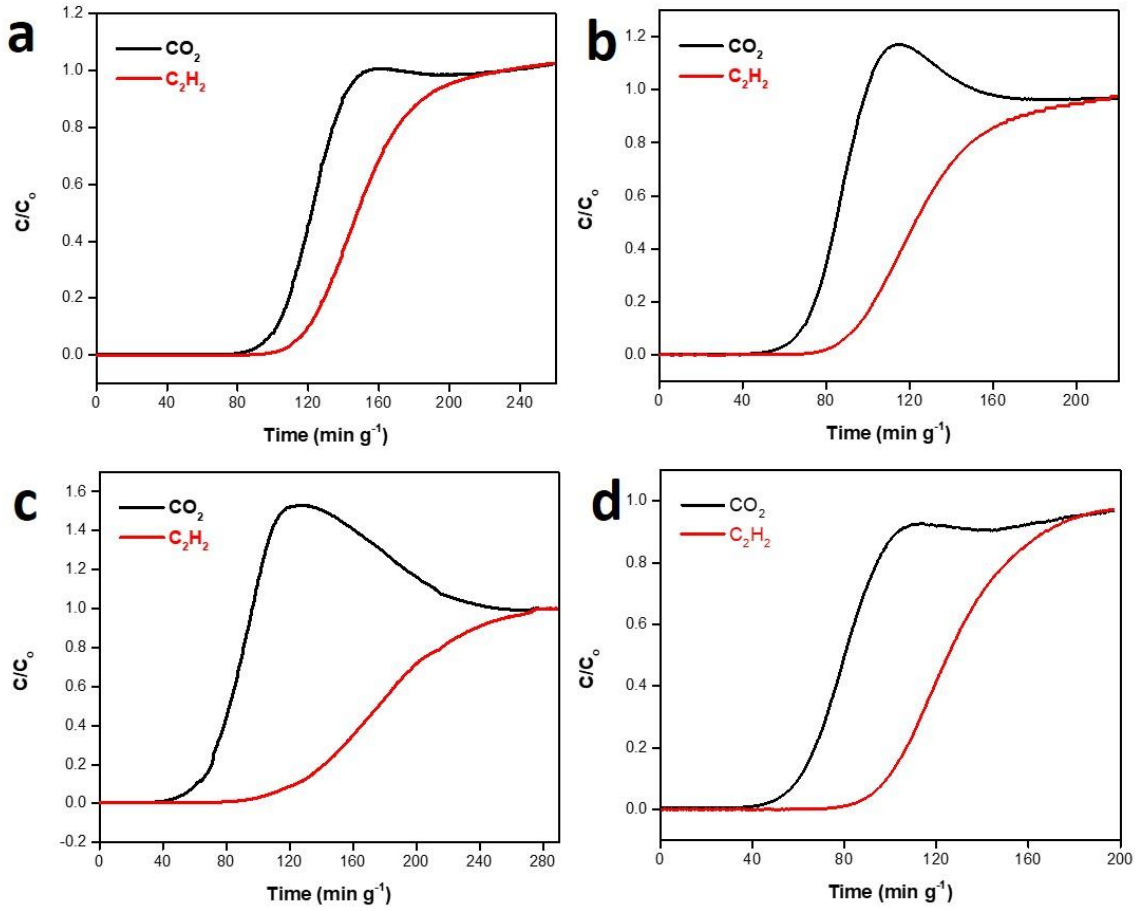

Figure 3.15 Breakthrough curves of a: Co_2V-BDC-TPC, B: Co_2V-BDC-TPB, c: Co_2V-BDC-TPT, d: Co_2V-TAZBC-TPB.

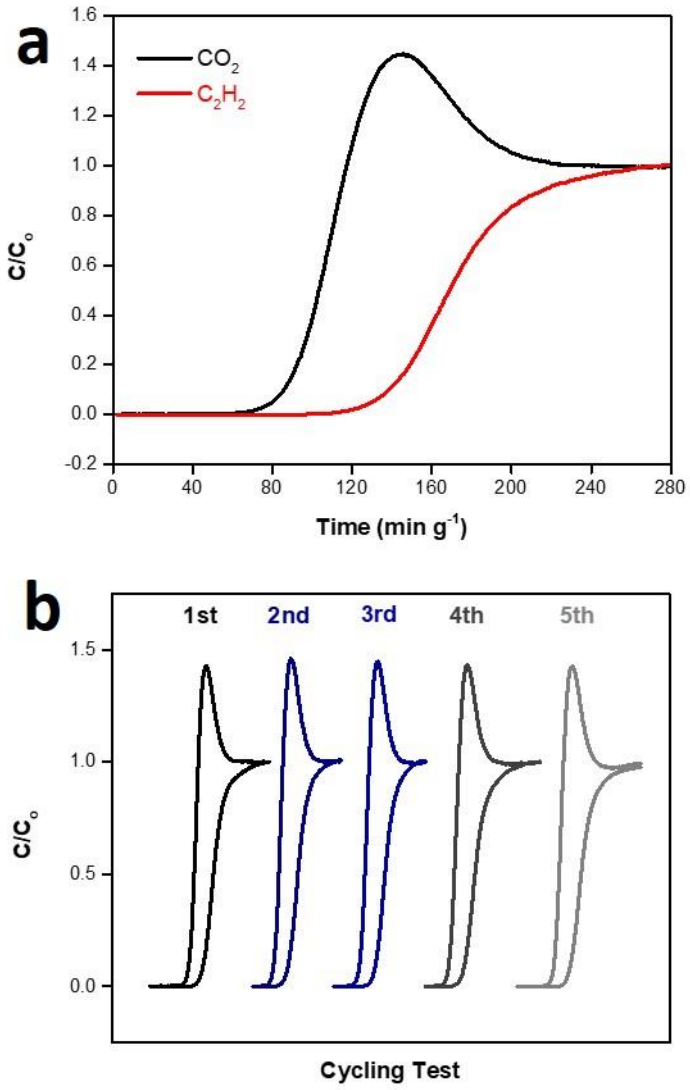

Figure 3.16 Breakthrough curves of a: Co-CPT-TPB, b: cycling test for Co-CPT-TPB.

3.4 Conclusion

In summary, we have prepared five different MOFs base on a novel in-situ monomer trimerization pore space partitioning method and systematically investigate the effects of three components on the C_2H_2/CO_2 separations. Compared with USTA-300a with ultra-high selectivity, this platform of materials possesses exceptional high uptake and provides another method to perform efficient separations. The structural versatility, high stability, and low-cost regeneration further push those materials for further investigations. Besides, the host-guest interactions reported here could be helpful to design novel MOFs for C_2H_2/CO_2 separations. Finally, the co-solvent method in this work emphasizes possibilities for the construction of various novel MOFs.

3.5 Reference

[1] D. S. Sholl, R. P. Lively, *Nature* **2016**, *532*, 435-437.

[2] a) X.-P. Fu, Y.-L. Wang, Q.-Y. Liu, *Dalton Trans.* **2020**, *49*, 16598-16607; b) Z. R. Herm, E. D. Bloch, J. R. Long, *Chem. Mater.* **2014**, *26*, 323-338.

[3] a) Z. Niu, X. Cui, T. Pham, G. Verma, P. C. Lan, C. Shan, H. Xing, K. A. Forrest, S. Suepaul, B. Space, A. Nafady, A. M. Al-Enizi, S. Ma, *Angew. Chem. Int. Ed.* **2021**, *60*, 5283-5288; b) Y.-P. Li, Y. Wang, Y.-Y. Xue, H.-P. Li, Q.-G. Zhai, S.-N. Li, Y.-C. Jiang, M.-C. Hu, X. Bu, *Angew. Chem. Int. Ed.* **2019**, *58*, 13590-13595; c) K.-J. Chen, Hayley S. Scott, David G. Madden, T. Pham, A. Kumar, A. Bajpai, M. Lusi, Katherine A. Forrest, B. Space, John J. Perry, Michael J. Zaworotko, *Chem* **2016**, *1*, 753-765.

[4] L. Li, R.-B. Lin, R. Krishna, H. Li, S. Xiang, H. Wu, J. Li, W. Zhou, B. Chen, *Science* **2018**, *362*, 443.

[5] X. Cui, K. Chen, H. Xing, Q. Yang, R. Krishna, Z. Bao, H. Wu, W. Zhou, X. Dong, Y. Han, B. Li, Q. Ren, M. J. Zaworotko, B. Chen, *Science* **2016**, *353*, 141.

[6] R.-B. Lin, L. Li, H. Wu, H. Arman, B. Li, R.-G. Lin, W. Zhou, B. Chen, *J. Am. Chem. Soc.* **2017**, *139*, 8022-8028.

[7] Q. G. Zhai, X. Bu, C. Mao, X. Zhao, L. Daemen, Y. Cheng, A. J. Ramirez-Cuesta, P. Feng, *Nat. Commun.* **2016**, *7*, 13645.

[8] a) A. C. Sudik, A. P. Côté, O. M. Yaghi, *Inorg. Chem.* **2005**, *44*, 2998-3000; b) C. Serre, F. Millange, S. Surblé, G. Férey, *Angew. Chem. Int. Ed.* **2004**, *43*, 6285-6289.

[9] X. Zhao, X. Bu, Q. G. Zhai, H. Tran, P. Feng, *J. Am. Chem. Soc.* **2015**, *137*, 1396-1399.

[10] a) Q.-G. Zhai, Y.-Y. Xue, X.-Y. Bai, J. Zhang, Y. Wang, S.-N. Li, Y.-C. Jiang, M.-C. Hu, *Angew. Chem. Int. Ed.* **2021**, *n/a*; b) Y. Ye, Z. Ma, R.-B. Lin, R. Krishna, W. Zhou, Q. Lin, Z. Zhang, S. Xiang, B. Chen, *J. Am. Chem. Soc.* **2019**, *141*, 4130-4136.

[11] a) X. Zhao, X. Bu, E. T. Nguyen, Q. G. Zhai, C. Mao, P. Feng, *J. Am. Chem. Soc.* **2016**, *138*, 15102-15105; b) S.-T. Zheng, X. Zhao, S. Lau, A. Fuhr, P. Feng, X. Bu, *J. Am. Chem. Soc.* **2013**, *135*, 10270-10273.

[12] Y. S. Wei, M. Zhang, P. Q. Liao, R. B. Lin, T. Y. Li, G. Shao, J. P. Zhang, X. M. Chen, *Nat. Commun.* **2015**, *6*, 8348.

[13] a) P. J. Waller, F. Gandara, O. M. Yaghi, *Acc. Chem. Res.* **2015**, *48*, 3053-3063; b) A. P. Côté, A. I. Benin, N. W. Ockwig, M. Keeffe, A. J. Matzger, O. M. Yaghi, *Science* **2005**, *310*, 1166; c) J. R. Hunt, C. J. Doonan, J. D. LeVangie, A. P. Côté, O. M. Yaghi, *J. Am. Chem. Soc.* **2008**, *130*, 11872-11873; d) F. J. Uribe-Romo, J. R. Hunt, H. Furukawa, C. Klöck, M. O'Keeffe, O. M. Yaghi, *J. Am. Chem. Soc.* **2009**, *131*, 4570-4571; e) T. Ben, H. Ren, S. Ma, D. Cao, J. Lan, X. Jing, W. Wang, J. Xu, F. Deng, J. M. Simmons, S. Qiu, G. Zhu, *Angew. Chem. Int. Ed.* **2009**, *121*, 9621-9624; f) X. Feng, X. Ding, D. Jiang, *Chem. Soc. Rev.* **2012**, *41*, 6010-6022; g) Q. Fang, Z. Zhuang, S. Gu, R. B. Kaspar, J. Zheng, J. Wang, S. Qiu, Y. Yan, *Nat. Commun.* **2014**, *5*, 4503; h) X. Guan, H. Li, Y. Ma, M. Xue, Q. Fang, Y. Yan, V. Valtchev, S. Qiu, *Nat. Chem.* **2019**.

[14] a) Z. Chen, X. Li, C. Yang, K. Cheng, T. Tan, Y. Lv, Y. Liu, *Advanced Science* **2021**, *8*, 2101883; b) Y. Li, M. Karimi, Y.-N. Gong, N. Dai, V. Safarifard, H.-L. Jiang, *Matter* **2021**, *4*, 2230-2265; c) Y. Hu, S. J. Teat, W. Gong, Z. Zhou, Y. Jin, H. Chen, J. Wu, Y. Cui, T. Jiang, X. Cheng, W. Zhang, *Nat. Chem.* **2021**; d) L. Feng, K.-Y. Wang, X.-L. Lv, T.-H. Yan, J.-R. Li, H.-C. Zhou, *J. Am. Chem. Soc.* **2020**; e) L. Feng, K.-Y. Wang, X.-L. Lv, J. A. Powell, T.-H. Yan, J. Willman, H.-C. Zhou, *J. Am. Chem. Soc.* **2019**, *141*, 14524-14529; f) H. L. Nguyen, F. Gándara, H. Furukawa, T. L. H. Doan, K. E. Cordova, O. M. Yaghi, *J. Am. Chem. Soc.* **2016**, *138*, 4330-4333; g) F.-M. Zhang, J.-L. Sheng, Z.-D. Yang, X.-J. Sun, H.-L. Tang, M. Lu, H. Dong, F.-C. Shen, J. Liu, Y.-Q. Lan, *Angew. Chem. Int. Ed.* **2018**, *57*, 12106-12110; h) A. Dutta, K. Koh, A. G. Wong-Foy, A. J. Matzger, *Angew. Chem. Int. Ed.* **2015**, *54*, 3983-3987.

[15] Y. Wang, X. Zhao, H. Yang, X. Bu, Y. Wang, X. Jia, J. Li, P. Feng, *Angew. Chem. Int. Ed.* **2019**, *58*, 6316-6320.

[16] E. D. Bloch, W. L. Queen, R. Krishna, J. M. Zadrozny, C. M. Brown, J. R. Long, *Science* **2012**, *335*, 1606-1610.

[17] J.-W. Zhang, M.-C. Hu, S.-N. Li, Y.-C. Jiang, P. Qu, Q.-G. Zhai, *Chem. Commun.* **2018**, *54*, 2012-2015.

[18] H. Yang, T. X. Trieu, X. Zhao, Y. Wang, Y. Wang, P. Feng, X. Bu, *Angew. Chem. Int. Ed.* **2019**, *0*.

[19] F. Luo, C. Yan, L. Dang, R. Krishna, W. Zhou, H. Wu, X. Dong, Y. Han, T.-L. Hu, M. O'Keeffe, L. Wang, M. Luo, R.-B. Lin, B. Chen, *J. Am. Chem. Soc.* **2016**, *138*, 5678-5684.

[20] Y.-L. Peng, T. Pham, P. Li, T. Wang, Y. Chen, K.-J. Chen, K. A. Forrest, B. Space, P. Cheng, M. J. Zaworotko, Z. Zhang, *Angew. Chem. Int. Ed.* **2018**, *57*, 10971-10975.

[21] J. Gao, X. Qian, R.-B. Lin, R. Krishna, H. Wu, W. Zhou, B. Chen, *Angew. Chem. Int. Ed.* **2020**, *59*, 4396-4400.

[22] W. Fan, S. Yuan, W. Wang, L. Feng, X. Liu, X. Zhang, X. Wang, Z. Kang, F. Dai, D. Yuan, D. Sun, H.-C. Zhou, *J. Am. Chem. Soc.* **2020**, *142*, 8728-8737.

[23] L. Liu, Z. Yao, Y. Ye, Y. Yang, Q. Lin, Z. Zhang, M. O'Keeffe, S. Xiang, *J. Am. Chem. Soc.* **2020**, *142*, 9258-9266.

[24] J. Pei, K. Shao, J.-X. Wang, H.-M. Wen, Y. Yang, Y. Cui, R. Krishna, B. Li, G. Qian, *Adv. Mater.* **2020**, *32*, 1908275.

[25] Y. Zhang, J. Hu, R. Krishna, L. Wang, L. Yang, X. Cui, S. Duttwyler, H. Xing, *Angew. Chem. Int. Ed.* **2020**, *59*, 17664-17669

.

Chapter 4 Gas Adsorption Sites Study in pacs Materials via Size-tuning on Pore-Space Partition Ligand

4.1 Introduction

Pore-space partition has been known as an efficient method to boost gas uptakes in the crystalline porous materials.[1] Numerous gases including CO_2, C_2H_2, C_2H_4, C_2H_6, C_3H_6, and C_3H_8, have been studied in this platform.[2] Among all gases, the uptakes of CO_2, C_2H_2, and C_2H_6 are extraordinarily high in pore-space partitioned materials (also known as **pacs** materials) compared to other materials. For instance, C_2H_6 uptake in $Mg_2V(OH)BDC_3TPT$ is as high as 166.8 cm^3/g at around 1 bar and 298 K. This is the highest C_2H_6 uptake among all materials. And CO_2 uptake in $Mg_2V(OH)DHBDC_3TPT$ is as high as 232.3 cm^3/g at 1 atm and 273 K. This is one of the best CO_2 adsorbents among all materials reported to date. Besides, the isosteric heat of adsorption (Q_{st}) in C_2H_2 belongs to CPM-733 [$Co_2V(OH)BDC_3TPT$] is only 21.9 kJ/mol at zero coverage, which is much lower than 66.8 kJ/mol for $Fe_2(O_2)$(dobdc) and 25 kJ/mol for Fe_2(dobdc).[3] The Q_{st} in CO_2 for CPM-233 [$Mg_2V(OH)(DHBDC)_3TPT$] is 20.38 kJ/mol at zero coverage, which is much

lower than 42 kJ/mol for Mg-MOF-74 [Mg_2(dobdc)] and 42.2 kJ/mol for Cu-TDPAT [Cu_3(TDPAT)(H_2O)$_3$].[4]

The high uptake capacity combining with the lowest isosteric heat of adsorption enable pore-space partition strategy to be an effective and energy-saving gas adsorbent. What is more, it attracts a lot of attention for the host-guest interaction mechanism.

In 2016, Jiang et al. utilized DFT method to simulate and determine two active sites in CPM-33b [Ni_3(OH)DHBDC$_3$TPT].[5] Different from the strong interaction between oxygen site in carbon dioxides and open metal sites in non-partitioned material, the open metal site quenched or pore-partitioned material exposed two carboxylate sites both above and below the partitioning reagent-pyridine ring. The carboxylate sites from both sides of the pyridine interaction with the carbon site on carbon dioxide molecule independently and the binding energies are around 30 kJ/mol on both sides. In addition to the active sites mentioned above, carboxylate groups on the parent framework ligand, DHBDC, enable the formation of intramolecular hydrogen bond and polarization on the hydroxyl group. And exposed oxygen site on hydroxyl group interacts with carbon site on carbon dioxide molecule resulting in a 34.5 kJ/mol binding energy. This calculation study helps us better understand the host-guest interaction in CPM-33 series of materials and the adsorption mechanism in pore-space partitioned materials.

In 2020, our group reported a pore-space partition-enabled C_2H_6-selective in C_2H_6/ C_2H_4 separation by utilizing CPM733 [Co_2V(OH)BDC$_3$TPT] as adsorbent. In this work, we found out there was no strong site on the framework through GCMC simulations. However, we figured out the preferential sites for the adsorption of C_2H_6 over C_2H_4 via

DFT calculations. [2b] The phenyl rings on three BDC ligands below or above the metal-trimer interacted with the light hydrocarbons through C–H···π interaction resulting binding energies of 35.85 kJ/mol for C_2H_6 over 33.76 kJ/mol for C_2H_4. Even if the interactions between guest gas molecules and host framework studied in this work are not strong, this work provides us an alternative view into the host-guest interactions in the pore-space partitioned materials.

Although some simulations have been reported to explain the interaction sites in pore-space partitioned materials, there is no report on host-guest interaction study via structural tuning as far as we know.

In this work, a size-tuning strategy on pore-space partitioning reagents was employed to design and synthesize two structures, $Co_2V(OH)(BPDC)_3TPB$ and $Co_2V(OH)(BPDC)_3TPPB$ [where BPDC is bipenyl-4,4'-dicarboxylate, TPB is 2,4,6-tri(4-pyridinyl)-1,3,5-boroxine, and TPPB is 2,4,6-tris(4-(pyridin-4-yl) phenyl)-1,3,5-boroxine] (Figure 4.1). The fixed size on the parent framework, which is determined by BPDC, and the size-tuning on pore-space partitioning ligands enable us to change the angles between BPDC and pore-partitioning plane. The angle tuning facilitates us to study host-guest interactions under the same chemical environment but in different size of the pore space.

4.2 Experimental Section

4.2.1 Chemicals and General Methods

All reagents were purchased and utilized without further purification. cobalt nitrate hexahydrate ($Co(NO_3)_2 \cdot 6H_2O$), cobalt chloride hexahydrate ($CoCl_2 \cdot 6H_2O$), vanadium (III) chloride (VCl_3), indium (III) chlorides tetrahydrate ($InCl_3 \cdot 4H_2O$), bipenyl-4,4'-dicarboxylic acid (H_2BPDC), pyridine-4-boronic acid (96%), 4-(pyridine-4-yl)phenylboronic acid, N, N-dimethylformamide (DMF), 1,3,5-trimethylbenzene (TMB), extra dry acetone.

Sample Activation and Gas Sorption Measurement.

Gas sorption measurements were carried out on a Micromeritics ASAP 2020 PLUS Physisorption Analyzers. Prior to the measurement, around 50 mg of the as-synthesized samples were immersed in 20 ml extra dry Acetone under inert gas protection for three days. After solvent exchange, samples were degassed under room temperature for 5 h and then under 100 ° C for 24h to yield guest-free samples.

General characterization.

Other characterization such as PXRD, SCXRD, EDS, SEM, TGA were followed the same procedures in 2.2.2.

4.2.2 Synthesis Methods

Synthesis of [$Co_2V(OH)(BPDC)_3TPB$] (CPM-100g).

In a 11 mL glass vial, 120 mg of $Co(NO_3)_2 \cdot 6H_2O$ (~0.4 mmol), 34 mg VCl_3 (~0.2 mmol), 144 mg H_2BPDC (~0.6 mmol), and 72 mg pyridine-4-boronic acid (~0.6 mmol) were dissolved in solvent mixture of 9 ml dimethylformamide (DMF), 0.25 ml 1,3,5-trimethylbenzene (TMB). After being stirred for an hour, the vial was placed in a 120 ℃ oven for 6 days, and the mixture was then cooled to room temperature. Dark-red spindle-shaped microcrystals were obtained. The phase purity was supported by powder X-ray diffraction.

Synthesis of [$Co_2V(OH)(BPDC)_3TPPB$] (Co_2V-BPDC-TPPB or CPM-1000).

In a 11 mL glass vial, 60 mg of $Co(NO_3)_2 \cdot 6H_2O$ (~0.2 mmol), 17 mg VCl_3 (~0.1 mmol), 72 mg H_2BPDC (~0.3 mmol), and 60 mg 4-(pyridine-4-yl)phenylboronic acid (~0.3 mmol) were dissolved in solvent mixture of 6 ml dimethylformamide (DMF), 0.25 ml 1,3,5-trimethylbenzene (TMB). After being stirred for an hour, the vial was placed in a 120 ℃ oven for 6 days, and the mixture was then cooled to room temperature. Dark-red spindle-shaped microcrystals were obtained. The phase purity was supported by powder X-ray diffraction.

Synthesis of [$Co_{1.63}In_{1.37}(OH)_{0.63}(O)_{0.37}(BPDC)_3TPPB$] ($Co_2In$-BPDC-TPPB or CPM-1000-CoIn).

In a 11 mL glass vial, 80 mg of $InCl_3 \cdot 4H_2O$, 50 mg $CoCl_2 \cdot 6H_2O$, 90 mg H_2BPDC , and 60 mg 4-(pyridine-4-yl)phenylboronic acid were dissolved in solvent mixture of 6 ml

dimethylformamide (DMF), 1.25 ml 1,3,5-trimethylbenzene (TMB). After being stirred for an hour, the vial was placed in a 120 ℃ oven for 6 days, and the mixture was then cooled to room temperature. Pink single crystals were obtained. The crystal data was collected on Bruker SCXRD mentioned in 2.2.2 and refined by OLEX2. The metal ratio in this material was determined through crystal data refinement in Table 4.1.

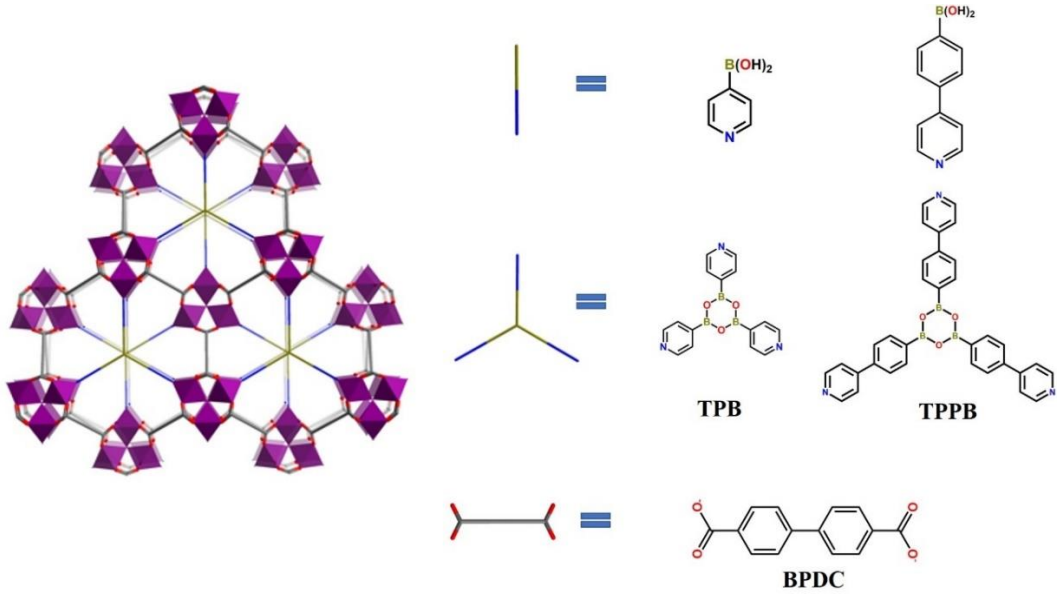

Figure 4.1 Structural illustration of **pacs** MOFs in this work. From top to bottom include two monomers (pyridine-4-boronic acid and 4-(pyridine-4-yl) phenylboronic acid), two monomer-trimerized L1 ligands (TPB and TPPB), and one L2 ligand (BPDC).

4.3 Results and Discussion

4.3.1 Structure Analysis

Both structures of $Co_2V(OH)(BPDC)_3TPB$ (also named as Co_2V-BPDC-TPB or CPM-100g) and $Co_2V(OH)(BPDC)_3TPPB$ (also named as Co_2V-BPDC-TPPB or CPM-1000-CoV) were confirmed through the comparison between PXRD patterns and simulated

results from crystal structures (Figure 4.2). $Co_2V(OH)(BPDC)_3TPB$ was matched with the PXRD data of CPM-85-In, for which the formular is $[In_3O(BPDC)_3(TPT)](NO_3)$. $Co_2V(OH)(BPDC)_3TPPB$ was matched with the PXRD data of CPM-1000-CoIn, for which the formular is $Co_{1.63}In_{1.37}(OH)_{0.63}(O)_{0.37}(BPDC)3TPPB$.[6] The structure refinement of CPM-1000-CoIn was performed on OLEX2. The Co/In ratio was estimated from the occupancy refinement with single crystal X-ray diffraction data. The Co/V ratios in Co_2V-BPDC-TPB and Co_2V-BPDC-TPPB were analyzed by EDS (Figure 4.3). TGA results of both Co_2V-BPDC-TPB and Co_2V-BPDC-TPPB are similar as shown in Figure 4.4.

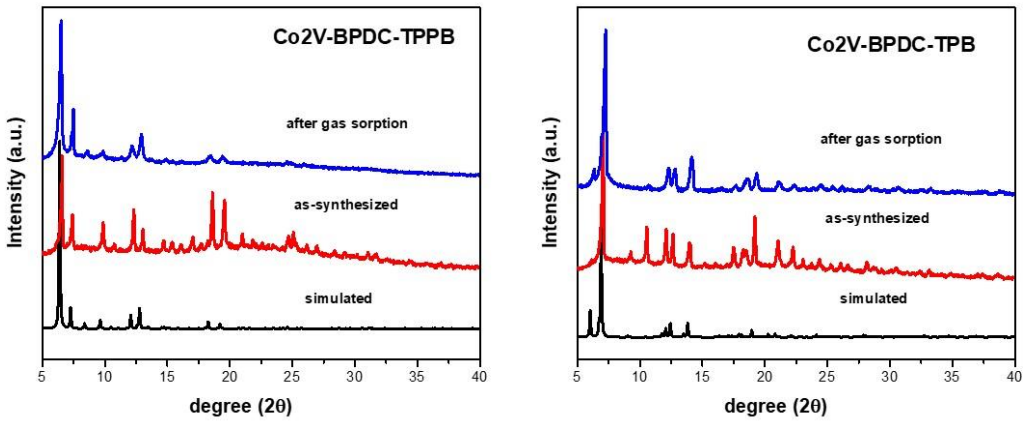

Figure 4.2 PXRD patterns for Co_2V-BPDC-TPB and Co_2V-BPDC-TPPB.

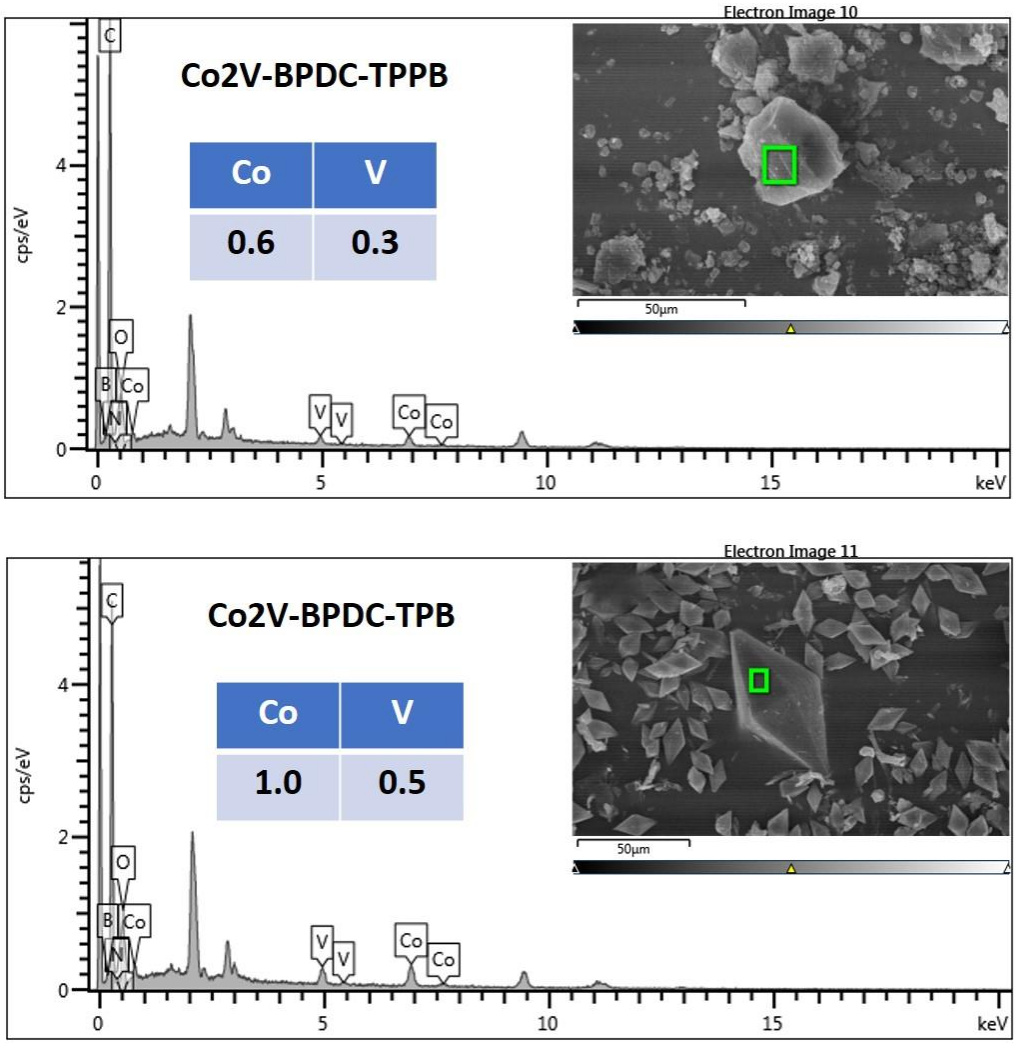

Figure 4.3 SEM and EDS results for Co_2V-BPDC-TPB and Co_2V-BPDC-TPPB.

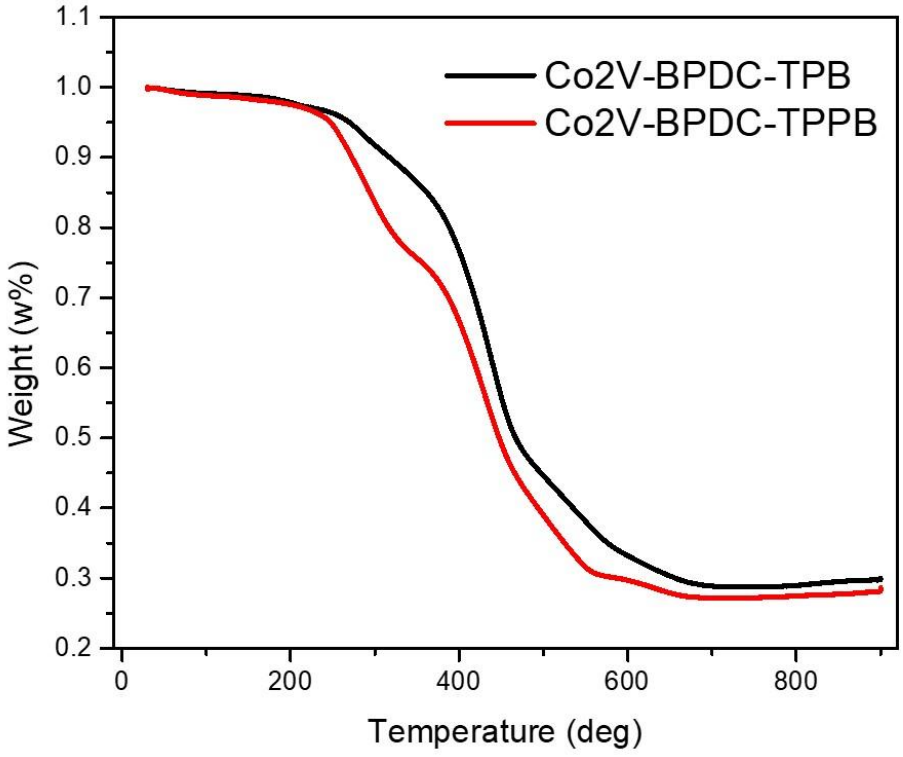

Figure 4.4 TGA results for Co_2V-BPDC-TPB and Co_2V-BPDC-TPPB.

4.3.2 Gas Adsorption and Gas Interaction Site Study

Isothermal N_2 adsorption and desorption at 77 K was conducted to reveal the surface areas in these two materials. As shown in Figure 4.5, the N_2 isotherms of two materials are both type I indicating the existence of micropores. And the BET surface areas are 1945 cm^3/g for Co_2V-BPDC-TPB and 2003 cm^3/g for Co_2V-BPDC-TPPB. As shown in Figure 4.6, the distance between Co_2V trimers is determined by the parent framework ligand, which is fixed by BPDC. Through size tuning on pore-space partitioning ligand from TPB to TPPB, the space in the channel is changed from a slim and tall cylinder to a

flat and short cylinder as illustrated in Figure 4.6b, 4.6c. The close surface areas and same chemistry environment in these two materials enable us to study the host-guest interaction through structural analysis.

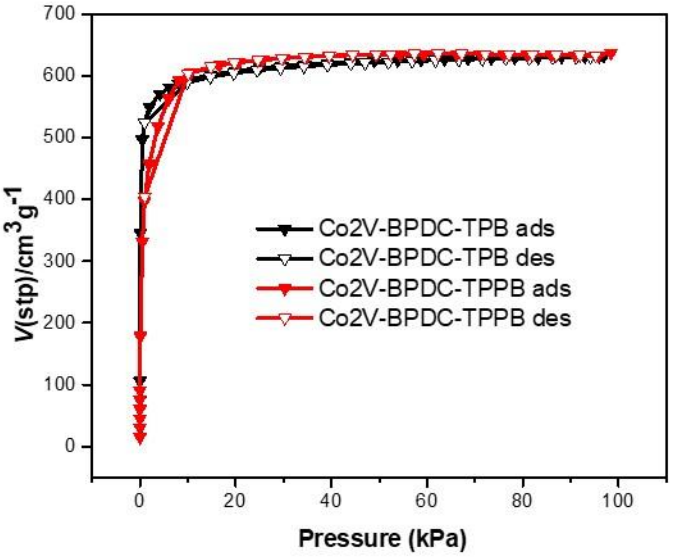

Figure 4.5 N_2 isotherms at 77 K for Co_2V-BPDC-TPB and Co_2V-BPDC-TPPB.

Isothermal C_3H_6 and C_3H_8 sorption at 273 K and 298 K was conducted in these two materials (Figure 4.7, 4.8). C_3H_6 sorption at 273 K is 238.3 cm^3/g for Co_2V-BPDC-TPB and 244.9 cm^3/g for Co_2V-BPDC-TPPB. C_3H_6 sorption at 298 K is 212.0 cm^3/g for Co_2V-BPDC-TPB and 203.7 cm^3/g for Co_2V-BPDC-TPPB. C_3H_8 sorption at 273 K is 234.7 cm^3/g for Co_2V-BPDC-TPB and 249.4 cm^3/g for Co_2V-BPDC-TPPB. C_3H_8 sorption at 298 K is 182.3 cm^3/g for Co_2V-BPDC-TPB and 181.4 cm^3/g for Co_2V-BPDC-TPPB (Table 4.2). There are no significant differences for adsorptions between C_3H_6 and C_3H_8 in these two materials. This indicates the selectivity between C_3H_6 and C_3H_8 are small. Isosteric heat of sorption was calculated through C_3H_6 and C_3H_8 isotherms at 273 K and 298 K. As

shown in Figure 4.9, the Q_{st} are 25.4 kJ/mol (C_3H_6) and 25.5 kJ/mol (C_3H_8) for Co_2V-BPDC-TPB, and 32.0 kJ/mol (C_3H_6) and 32.7 kJ/mol (C_3H_8) for Co_2V-BPDC-TPPB. The Q_{st} values reveal the host-guest interaction intensity, which is low in these two materials, between different gases. This follows the same trend in isotherm sorption. The selectivity was calculated through IAST and shown in Figure 4.10. The selectivity between C_3H_6 and C_3H_8 was 1.1 for Co_2V-BPDC-TPB and 1.07 for Co_2V-BPDC-TPPB. There is nearly no selectivity in these two materials. The IAST simulation parameters are listed in Table 4.3.

Although there is no selectivity between C_3H_6 and C_3H_8 in Co_2V-BPDC-TPB and Co_2V-BPDC-TPPB, the Q_{st} of C_3H_6 and C_3H_8 shows similar trend for both materials. The Q_{st} of C_3H_6 and C_3H_8 in Co_2V-BPDC-TPPB are higher than that of Co_2V-BPDC-TPB at low uptakes, and are surpassed by Co_2V-BPDC-TPB at high uptakes. The interesting Q_{st} results lead us to propose the interaction sites in these two materials through structure analysis. In Figure 4.11 and Table 4.4, the dihedral angles between pore-space partitioning ligand plane and dual-BPDC plane are ~75° for Co_2V-BPDC-TPB and~ 52° for Co_2V-BPDC-TPPB. The narrower dihedral angle in Co_2V-BPDC-TPPB leads to a stronger host-guest interaction and a proposed interaction site A at low uptake amount. The dihedral angles between pore-space partitioning ligand plane and single-BPDC plane are ~66° for Co_2V-BPDC-TPB and ~35° for Co_2V-BPDC-TPPB. The wider dihedral angle in Co_2V-BPDC-TPB narrows the distance between three BPDC ligands leading to a strong host-guest interaction after site A is saturated and a proposed interaction site B at high uptake amount. These two sites are according with the simulation results in two previous works.

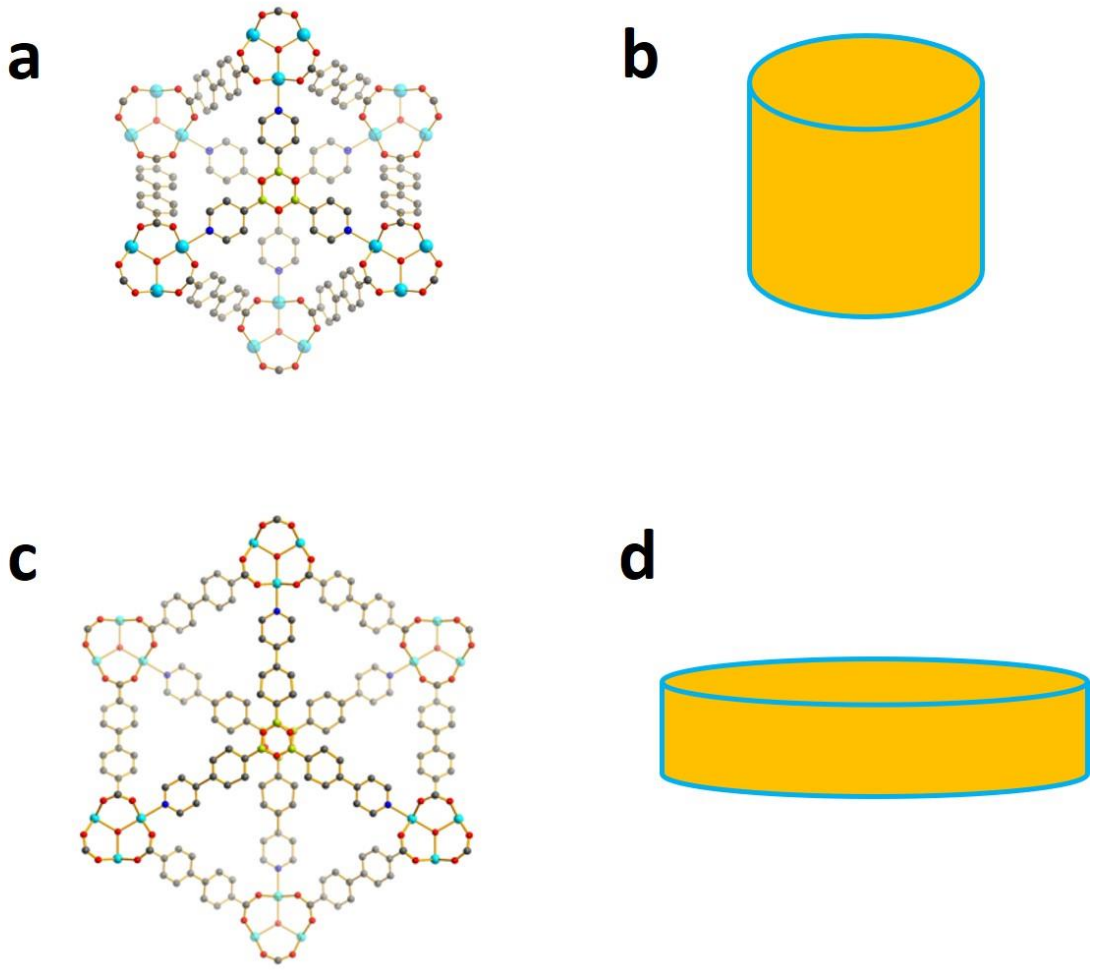

Figure 4.6 Structure and pore space illustrations for Co_2V-BPDC-TPB and Co_2V-BPDC-TPPB.

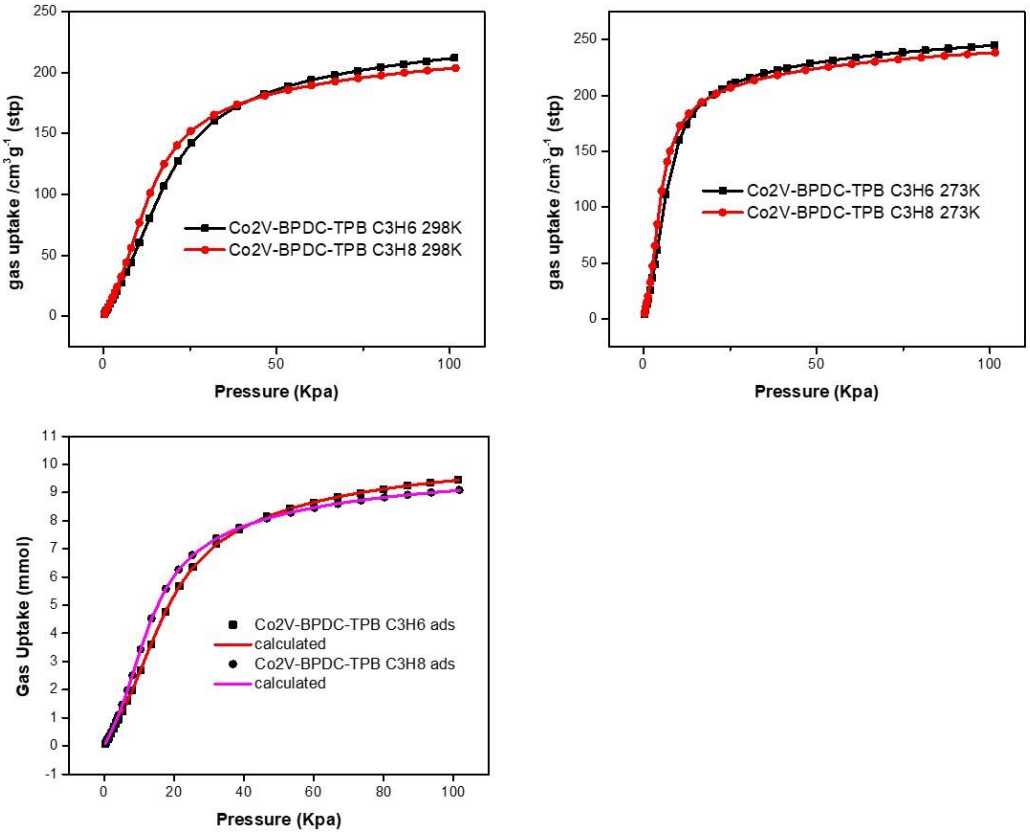

Figure 4.7 C_3H_6 and C_3H_8 adsorptions and simulated results at 298 K and 273 K for Co_2V-BPDC-TPB.

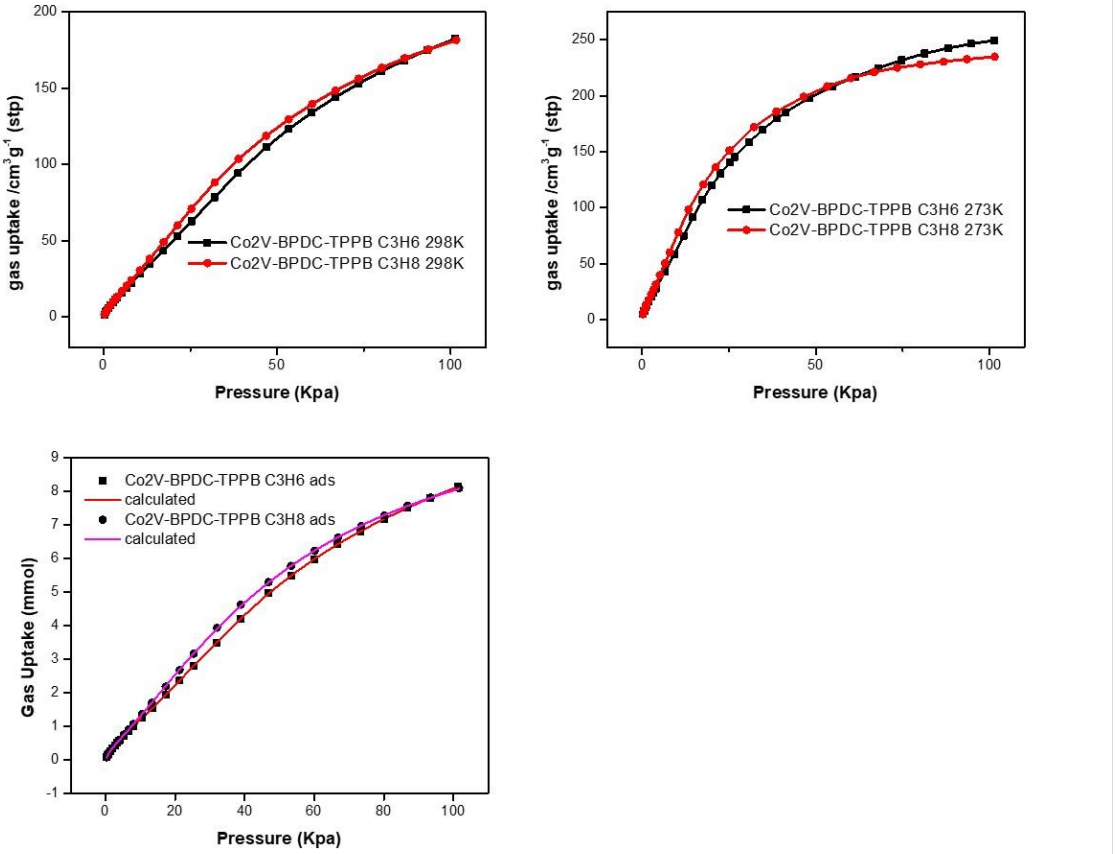

Figure 4.8 C_3H_6 and C_3H_8 adsorptions and simulated results at 298 K and 273 K for Co_2V-BPDC-TPPB.

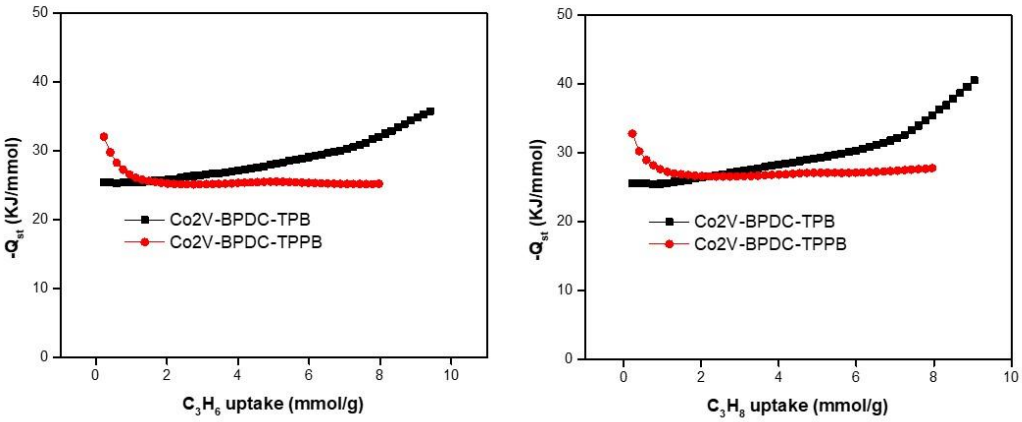

Figure 4.9 Isosteric heat of sorption of C_3H_6 and C_3H_8 for Co_2V-BPDC-TPB and Co_2V-BPDC-TPPB.

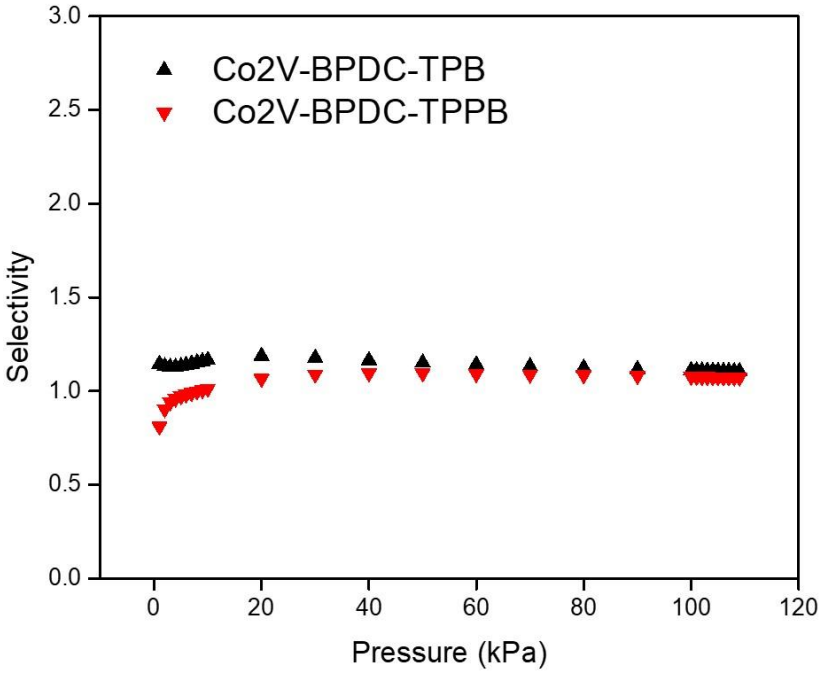

Figure 4.10 Selectivity between C_3H_6 and C_3H_8 for Co_2V-BPDC-TPB and Co_2V-BPDC-TPPB.

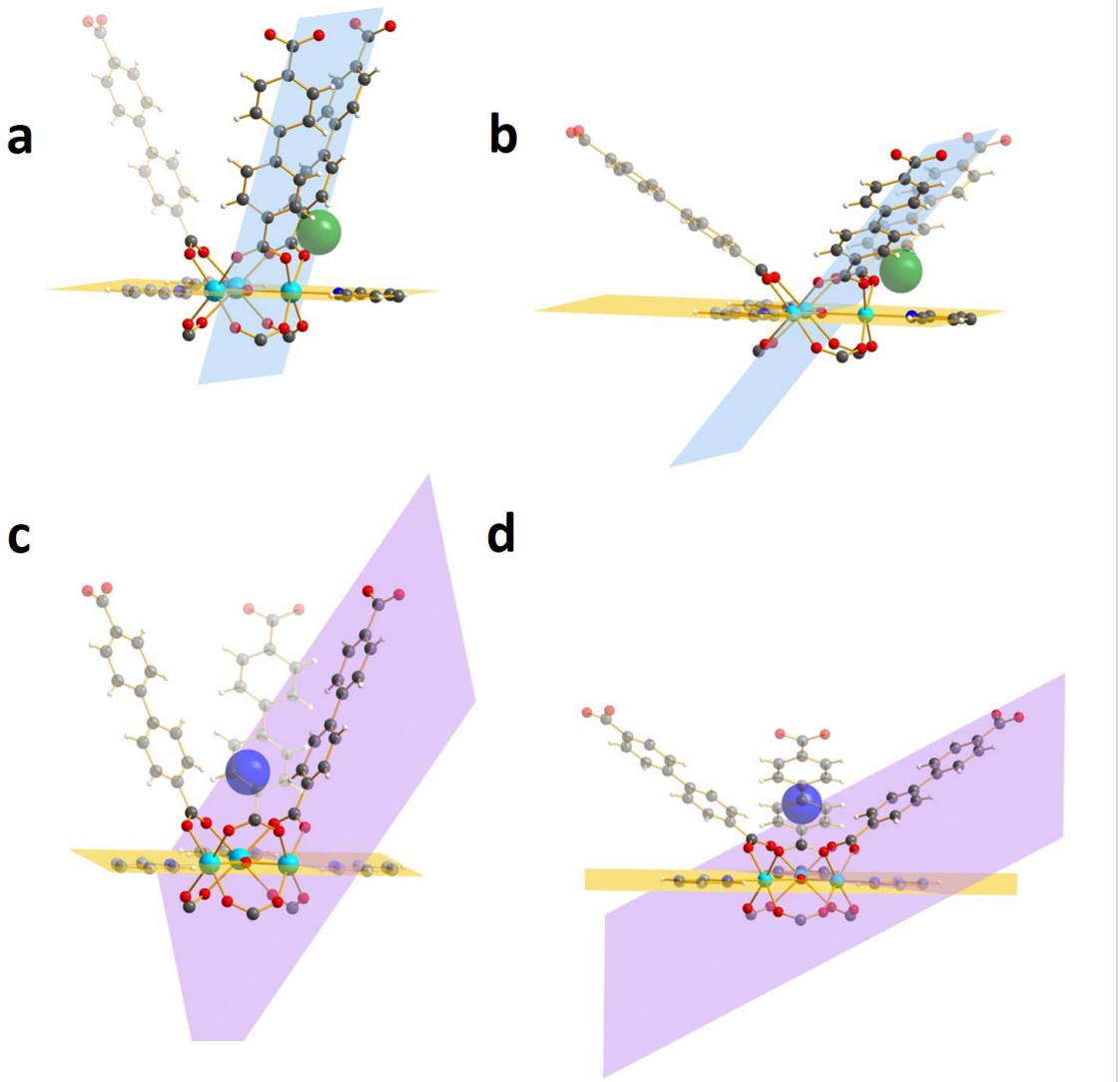

Figure 4.11 Dihedral planes and interaction sites (green: site A; blue: site B) in Co_2V-BPDC-TPB and Co_2V-BPDC-TPPB.

Table 4.1 Crystal data and structure refinement for CoIn-CPM-1000.

Identification code	CoIn-CPM-1000	
Empirical formula	C75H54 B3 Co1.63 In1.37 N3 O16	
Formula weight	1539.17	
Temperature	296.15 K	
Wavelength	0.71073 Å	
Crystal system	Hexagonal	
Space group	$P6_3/mmc$	
Unit cell dimensions	a = 24.35(2) Å	a= 90°.
	b = 24.354 Å	b= 90°.
	c = 18.365(16) Å	g = 120°.
Volume	9434(18) $Å^3$	
Z	2.00016	
Density (calculated)	0.542 Mg/m^3	
Absorption coefficient	0.334 mm^{-1}	
F(000)	1559	
Theta range for data collection	1.470 to 23.252°.	
Index ranges	-26<=h<=25, -27<=k<=26, -20<=l<=20	
Reflections collected	49558	
Independent reflections	2531 [R(int) = 0.0961]	
Completeness to theta = 23.252°	99.7 %	
Absorption correction	Semi-empirical from equivalents	
Max. and min. transmission	0.7449 and 0.6061	
Refinement method	Full-matrix least-squares on F^2	
Data / restraints / parameters	2531 / 115 / 117	
Goodness-of-fit on F^2	1.052	
Final R indices [I>2sigma(I)]	R1 = 0.0955, wR2 = 0.2638	
R indices (all data)	R1 = 0.1251, wR2 = 0.2849	
Extinction coefficient	0.0002(2)	
Largest diff. peak and hole	1.083 and -0.645 $e.Å^{-3}$	

Table 4.2. Summary of gas adsorption properties for MOFs in this work.

MOFs	S_{BET} (m^2/g)	C_3H_8 298 K, 1bar	C_3H_6 298 K, 1bar	C_3H_8/ C_3H_6 selectivity	Qst (C_3H_8)	Qst (C_3H_6)	C_3H_8 273 K, 1bar	C_3H_6 273 K, 1bar
Co_2V-BPDC-TPB	1945.5	203.7	212.0	1.1	25.5	25.4	238.3	244.9
Co_2V-BPDC-TPPB	2003.3	181.4	182.3	1.07	32.7	32.0	234.7	249.4

Table 4.3. Summary of the refine parameters with Dual-Site Langmuir-Freundlich fitting for the single-component adsorption isotherm s of C_3H_6 and C_3H_8 at 298 K.

MOFs	Gases	$q_{A,sat}$ (mmol/g)	b_A (kPa^{-1})	n_A	$q_{B,sat}$ (mmol/g)	b_B (kPa^{-1})	n_B	R^2
Co_2V-BPDC-TPB	C_3H_8	3.845596	0.000719	2.859261	6.327898	0.0422	1.024654	0.99999
	C_3H_6	3.804514	0.000294	2.870747	7.067773	0.0335	1.036851	0.99999
Co_2V-BPDC-TPPB	C_3H_8	10.53621	0.003199	1.446137	0.511924	0.509	1.080044	0.99999
	C_3H_6	2.857919	6.86E-05	2.536526	26.6627	7.58E-03	0.769694	0.99999

Table 4.4. Dihedral angles and two interaction sites in Co_2V-BPDC-TPB and Co_2V-BPDC-TPPB.

	Co_2V-BPDC-TPB	Co_2V-BPDC-TPPB
Site A	75	52
Site B	66	35

4.4 Conclusion

In this work, $Co_2V(OH)(BPDC)_3TPB$ and $Co_2V(OH)(BPDC)_3TPPB$ were designed and prepared to study the host-guest interactions between frameworks with C_3H_6 and C_3H_8.Two interaction sites were analyzed and confirmed through gas adsorption and size-tuning on pore-space partitioning ligands. It is worth to mention that this is the first time utilizing experimental data to confirm the functional sites for gas molecules in pore-space partitioned materials. This strategy could be extended to other systems for host-guest interaction study.

4.5 Reference

[1] Q.-G. Zhai, X. Bu, X. Zhao, D.-S. Li, P. Feng, *Acc. Chem. Res.* **2017**, *50*, 407-417.

[2] a) Q. G. Zhai, X. Bu, C. Mao, X. Zhao, L. Daemen, Y. Cheng, A. J. Ramirez-Cuesta, P. Feng, *Nat. Commun.* **2016**, *7*, 13645; b) H. Yang, Y. Wang, R. Krishna, X. Jia, Y. Wang, A. N. Hong, C. Dang, H. E. Castillo, X. Bu, P. Feng, *J. Am. Chem. Soc.* **2020**, *142*, 2222-2227; c) A. N. Hong, H. Yang, T. Li, Y. Wang, Y. Wang, X. Jia, A. Zhou, E. Kusumoputro, J. Li, X. Bu, P. Feng, *ACS Applied Materials & Interfaces* **2021**.

[3] a) L. Li, R.-B. Lin, R. Krishna, H. Li, S. Xiang, H. Wu, J. Li, W. Zhou, B. Chen, *Science* **2018**, *362*, 443; b) E. D. Bloch, W. L. Queen, R. Krishna, J. M. Zadrozny, C. M. Brown, J. R. Long, *Science* **2012**, *335*, 1606-1610.

[4] a) D.-A. Yang, H.-Y. Cho, J. Kim, S.-T. Yang, W.-S. Ahn, *Energy & Environmental Science* **2012**, *5*, 6465-6473; b) B. Li, Z. Zhang, Y. Li, K. Yao, Y. Zhu, Z. Deng, F. Yang, X. Zhou, G. Li, H. Wu, N. Nijem, Y. J. Chabal, Z. Lai, Y. Han, Z. Shi, S. Feng, J. Li, *Angew. Chem. Int. Ed.* **2012**, *51*, 1412-1415.

[5] Z. Tian, S. Dai, D.-e. Jiang, *J. Phys. Chem. Lett.* **2016**, *7*, 2568-2572.

[6] X. Zhao, C. Mao, K. T. Luong, Q. Lin, Q.-G. Zhai, P. Feng, X. Bu, *Angew. Chem. Int. Ed.* **2016**, *55*, 2768-2772.